Louisiana State University
LSU Digital Commons

2010

Particle analysis in infrared laser desorption and ablation

Xing Fan
Louisiana State University and Agricultural and Mechanical College, fanxing.lsu@gmail.com

PARTICLE ANALYSIS IN INFRARED LASER DESORPTION AND ABLATION

A Dissertation

Submitted to the Graduate Faculty of the
Louisiana State University and
Agricultural and Mechanical College
in partial fulfillment of the
requirement for the degree of
Doctor of Philosophy

in

The Department of Chemistry

by
Xing Fan
B.S., University of Science and Technology of China, 2000
M.E., University of Science and Technology of China, 2004
December 2010

ACKNOWLEDGEMENTS

First of all, I would like to express my sincere gratitude to my advisor Professor Kermit Murray, for welcoming me into his group and continuous support in my Ph.D. program. I could not have finished the program without his priceless guidance and encouragement. His scientific passion will always inspire me to overcome difficulty and accomplish my goal.

Besides my advisor, I would like to thank the rest of my dissertation committee, Professor Jayne Garno, Professor Barry Dellinger, Professor David Spivak, and Professor Michael Murphy. I appreciate your encouragement and suggestions given to me in fulfilling my goal.

I would like to thank the former and current Murray group members, Nichole Bell, Jon Beusse, Lancia Darville, Jianan Dong, John Dugas, Juaneka Hayes, Fan Huang, Jae-Kuk Kim, Jeonghoon Lee, Mark Little, Thabiso Musapelo, Damien Narcisse, Sung-gun Park, Yohannes Rezenom, Feng Xu, and Yichuang Xu, who have helped me in completing my research and dissertation. Special gratitude goes to Mark Little who gave me a lot of help during my first year in Murray group and Fan Huang for his collaborative efforts with the infrared laser projects.

I dedicate this work to my parents, Wensheng Fan and Hua Li. They always give me their love and encouragement, which support me pursuing a Ph.D. degree abroad.

TABLE OF CONTENTS

LIST OF TABLES

LIST OF FIGURES

LIST OF ABBREVIATIONS

AFM	atomic force microscopy
APCI	atmospheric pressure chemical ionization
API	atmospheric pressure ionization
AP-MALDI	atmospheric pressure matrix-assisted laser desorption/ionization
CI	chemical ionization
CMOS	complementary metal-oxide-semiconductor
Da	dalton
DART	direct analysis in real time
DC	direct current
DEM	delayed extraction method
DESI	desorption electrospray ionization
Da	dalton
EI	electron ionization
Er:YAG	erbium-doped yttrium aluminium garnet
ESI	electrospray ionization
FAB	fast atom bombardment
FD	field desorption
FFDM	field-free drift method
FT-ICR	Fourier transform ion cyclotron resonance
FTIR-ATR	Fourier transform infrared - Attenuated total reflectance
GD	glow discharge
ICP	inductively coupled plasma
IR	infrared
KTP	potassium titanyl phosphate
LAMMA	laser microprobe mass analysis
LDESI	desorption electrospray ionization
LDI	laser desorption ionization

MALDESI	matrix assisted laser desorption electrospray ionization
MALDI	matrix-assisted laser desorption ionization mass spectrometry
MS	mass spectrometry
MS/MS	tandem mass spectrometry
m/z	mass-to-charge ratio
NBA	3-nitrobenzyl alcohol
Nd:YAG	neodymium-doped yttrium aluminium garnet
OPO	optical parametric oscillators
PD	plasma desorption
ppt	part per trillion
SIMS	secondary ion mass spectrometry
TEM	transmission electron microscopy
UV	ultraviolet

ABSTRACT

The fundamental physical processes of mid infrared laser ablation in the context of laser desorption mass spectrometry were investigated. Understanding the mechanisms of infrared laser desorption and ablation can lead to improvements in these techniques and expand their applications. Particles were generated from glycerol irradiated at atmospheric pressure using a tunable infrared laser at wavelengths between 2.6 and 3.8 µm. The wavelength dependence of size distributions of ablated particles was measured. The particle concentration roughly tracked the infrared absorption spectrum of glycerol and the mean particle size tracked the inverse of the IR absorption. A novel approach, post ablation particle irradiation, was developed to manipulate the size of ejected particles. Particles generated by a 2.94 µm laser ablation of 3-nitrobenzyl alcohol were irradiated with a 351 nm ultraviolet laser at different time delays. A reduction in the average particle size and an increase in the total particle concentration were recorded. In addition to particle sizing, fast photography was used to study the dynamics of mid infrared laser desorption and ablation. Images of scattered light from glycerol ablation at atmospheric pressure were recorded using a CMOS camera from 25 ns to 1000 µs delay. The velocity of the expanding plume ranged from greater than 300 m/s near the 3.0 µm OH stretch absorption of glycerol to less than 100 m/s near the 3.4 µm CH stretch. Modeling calculations of these experiments suggest that the vigorous ablation is driven by phase explosion in the stress confinement regime near the wavelength of OH stretch absorption followed by a plume

evolution for milliseconds. The wavelength and energy of the infrared laser can be used to effectively "tune" the composition of the desorption plume. This ability to control the composition of the plume will be used in the development of IR laser ambient ionization mass spectrometry techniques such as atmospheric pressure matrix-assisted laser desorption ionization (AP-MALDI) and matrix-assisted laser desorption electrospray ionization (MALDESI) where the ability to control material removal is critical to efficient ionization.

CHAPTER 1. INTRODUCTION

Laser desorption refers to laser-induced material ejection and has significant applications in mass spectrometry (MS), a widely used analytical technique.[1-8] Matrix-assisted laser desorption ionization mass spectrometry (MALDI-MS) [3, 9] is one of the two modern mass spectrometry techniques besides electrospray ionization mass spectrometry (ESI-MS) [10] that have become sensitive detection tools for large, non-volatile and labile molecules. The breakthrough by Koichi Tanaka demonstrated the application of MALDI to biomolecules as large as the 34,472 Da protein.[3] This led him to receive a portion of the 2002 Noble prize for chemistry shared with John Fenn for ESI.

Although there are several advantages to the use of MALDI, the mechanism of MALDI and is still under investigation.[11-12] The absorption of laser radiation is determined by the laser parameters such as. wavelength, pulse width, and fluence, as well as the nature of the matrix.[13-14] Due to the extreme heating rates induced by the laser pulse, phase change takes place and leads to material ejection.[15] The ion yields are controlled by the physical processes of this phase change and by the chemical processes that ultimately lead to ionization.[15] However, the ionization mechanism is a subject of considerable debate and the roles of the various components, including free molecules, clusters and particulate, in desorption ionization remain unclear.[11-13] The full exploitation and optimization of laser desorption ionization techniques cannot be

accomplished until the fundamental physical and chemical processes underlying the process are better understood.

In recent years, the development of new ionization source technology grows tremendously to realize functions of both MALDI and ESI for reducing sample preparation and multiply-charged ions generation.[16] Matrix assisted laser desorption electrospray ionization (MALDESI) is such a combination applied under ambient condition.[7-8] In MALDESI, a pulsed laser is used to desorb and ablate a condensed phase sample inducing the ejection of particles and gas molecules from the sample. The ejected neutral molecules are entrained in the charged electrospray droplets and the ablated particles merge with the electrospray, where the particles and molecules interact with the charged droplets, and highly charged ions are formed through the subsequent droplet evaporation.[16-19] Although the corresponding mechanism of ionization is still under investigation, recent studies of particle generation in laser desorption and ablation showed that ejected particles might play a role.[19-22] It is critical to learn how laser parameters such as energy, wavelength, and pulse width work on the material ejection and how the quantity of material removal, and size distribution and composition of ejected particles effect on ion formation by interaction with charged droplets from an electrospray source.

It is difficult to gain detailed information about the desorption and ionization processes in MALDI and MALDESI using only the mass spectrum obtained under different laser and sample preparation conditions. To gain additional understanding of the underlying phenomena, the

2

amount of material removed and both chemical and physical processes of the removal can be studied by other means. Molecular dynamics methods have been used in simulating the interaction of laser pulses with material.[23] Experimental studies have been undertaken with the goal of understanding the role of material desorption and particle formation.[20, 22, 24-26] Plume imaging has been used to examine directly the material desorption processes and investigate their temporal behavior.[27-28] Fluorescence spectroscopy was carried out to investigate the mechanism of photon absorption by matrices used in laser desorption and ionization. A large fraction of molecules in the excited singlet state was found undergoing singlet-singlet annihilation, a pathway to matrix ion generation.[29] An optical multi-channel analyser was utilized for the analysis of luminescence spectra of several matrices.[30] It was found that most of the energy absorbed by the molecules relaxed via non-radiative pathways and was available for desorption/ionization process. Karas and co-workers focused on the pH of analyte in matrix crystals and found that analyte molecules retained their solution charge state upon incorporation into the matrix.[31] The result supported ionization mechanism that desorption and ionization occurred together during the ejection of clusters and particles. Knochenmuss et al. argued that the physical processes of desorption of material separately from the chemical process of ionization of the analyte.[32] Charge transfer from matrix ions to the analyte molecules in the expanding plume of ejected material led to the ionization of analyte molecules. Photoelectrons were presumed emitting upon laser irradiation of a metal target covered by a thin sample layer.[33]

3

These electrons decreased the yield of positive ions, reduced ions with higher oxidation states, and improved the mass resolution.

In this chapter, an overview of mass spectrometry is presented. Various ionization methods used in MS and their corresponding ionization mechanisms are introduced and compared. Compared to other ionization methods, ionization involving a pulsed laser can realize ionization of biological compounds and synthetic polymers.[3-4] Details on the physical process in laser desorption/ablation are also presented. The investigation of physical process can help elucidate understand the mechanism, optimize, and extend the applications of laser desorption ionization. Several experimental methods used for the investigation of laser desorption are also introduced.

1.1. Mass Spectrometry

Mass spectrometry is an analytical technique in which atoms or molecules in the gas phase are transformed into ions and are separated by their mass-to-charge ratio. A mass spectrometer consists of three essential components: an ion source, a mass analyzer, and a detector.

Getting neutral molecules into the gas phase as ions is the first and quite important procedure of mass spectrometry. The challenge of ionization is to select a method for converting the sample compounds into ions that can be mass analyzed while at the same time preserving the properties of the sample that are of interest.[34] Different ionization methods, such as electron ionization, chemical ionization, spray ionization, and desorption ionization, are used in MS analysis for converting the sample compounds into ions[34] Electron ionization (EI) is a highly

4

energetic process and induces breaking of chemical bonds and fragmentation, which is called

"hard" ionization. Although fragmentation is useful for the identification of small molecules,[35] it

is not useful for larger molecules. To overcome the limits of hard ionization, soft ionization such

as matrix-assisted laser desorption/ionization (MALDI) [36] and electrospray ionization [10] have

been developed to minimize the fragmentation in the ionization process. These ionization

methods are discussed further below.

The ions generated in the ion source are then transferred to the mass analyzer that is under

high vacuum where static or dynamic electric or magnetic fields separate the ions based on their

mass-to-charge ratio (m/z), where m is given as the mass number of the ions and z as the charge

number of the ions. A great variety of mass analyzers have been used, just as there are many

different ion sources.[37] For continuous ion sources, scanning analyzers, such as magnetic sectors

[38] or quadrupole mass filters [39] are good separation choices. For pulsed ion sources, a

time-of-flight mass spectrometer is a good choice.[3] However, pulsed ion sources can be used in

quasi-continuous mode with a scanning mass spectrometer.[40] Sometimes several analyzers can

be combined in sequence for tandem mass spectrometry (MS/MS), to obtain a mass spectrum

resulting from the fragmentation in between two analyzers (tandem mass spectrometry in space)

or in a single analyzer (tandem mass spectrometry in time).[41]

After m/z selection, the ions are detected using a particle multiplier detector [42] or, with high

intensity beams, a Faraday cup detector. With some types of trapping instruments, such as the

Fourier transform ion cyclotron resonance (FT-ICR)[43] and orbitrap [44] mass spectrometers, the ion

image current is measured. The signal of ion current is amplified and recorded. The abundance

of each ion present is calculated and displayed in the form of a mass spectrum: ion relative

abundance as a function of *m/z*.

1.2. Ionization in Mass Spectrometry

For inorganic molecules, volatile organic molecules, non-volatile molecules, and

biomolecules, various ionization sources are developed to realize ionization.[34] Volatile and

thermally stable samples are suitable for gas-phase ionization by electron ionization and

chemical ionization. However, a large number of compounds are nonvolatile and thermally labile.

Ions from these compounds are extracted directly from the condensed phase sample to the gas

phase by spray or desorption ionization.

1.2.1. Ionization of Atoms and Small Molecules

1.2.1.1. Electron Ionization
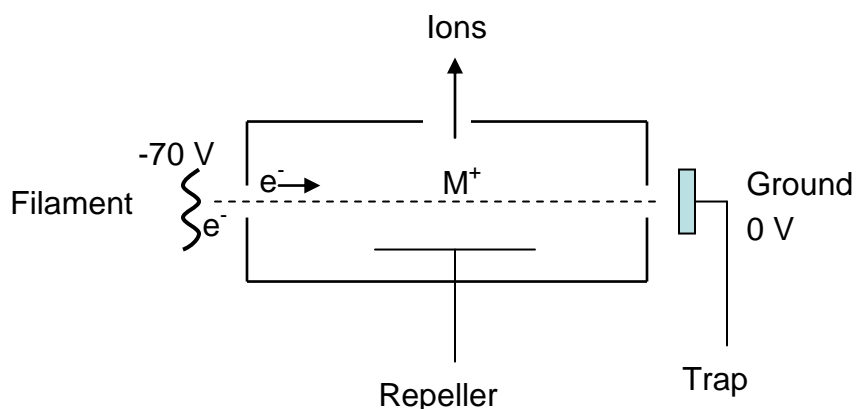
Figure 1-1 Schematic diagram of an EI source.

Electron ionization, as well as other hard ionization techniques such as spark ionization, low

discharge, and inductively coupled plasma ionization, have been widely applied to produce

molecular ions from volatile samples since the early part of the 20th century.[45] EI is suitable for

gas phase molecules but induces extensive fragmentation.[37] This ionization technique is limited

to volatile molecules smaller than hundreds of Da.[46]

A diagram of an EI source is shown in Figure 1-1. Electrons are produced by heating a metal

filament and accelerated by the potential difference between the filament and an ion source

chamber. The current passing the filament controls the number of emitted electrons. The beam of

accelerated electrons is directed into a gas phase sample at reduced pressure (< 0.1 milliTorr) in

the ion source chamber. When an energetic electron, typically 70 eV, collides with a neutral

analyte molecule (M), an electron of the neutral molecule is expelled and a positively charged

ion with one unpaired electron (a radical cation), denoted $M^{+\bullet}$, is formed according to

$$M + e^- \rightarrow M^{+\bullet} + 2e^- \qquad\qquad\qquad \text{(Eq. 1-1)}$$

A voltage is applied to a repeller electrode within the chamber that accelerates the radical cation

toward an exit aperture to a mass analyzer.

EI is typically used to determine the molecular weight and structure of molecules that are

sufficiently stable in the vaporization process with decomposition.[34] The ionization process can

produce either a molecular ion with the same molecular weight and elemental composition as the

starting analyte, or a fragment ion that corresponds to a smaller piece of the analyte molecule.

Both the $M^{+\bullet}$ and fragment ions are produced for most compounds. The relative ratio of the

radical cation and fragment depends on the energy required to break the molecule's internal

covalent bonds.[46]

1.2.1.2. Spark Ionization
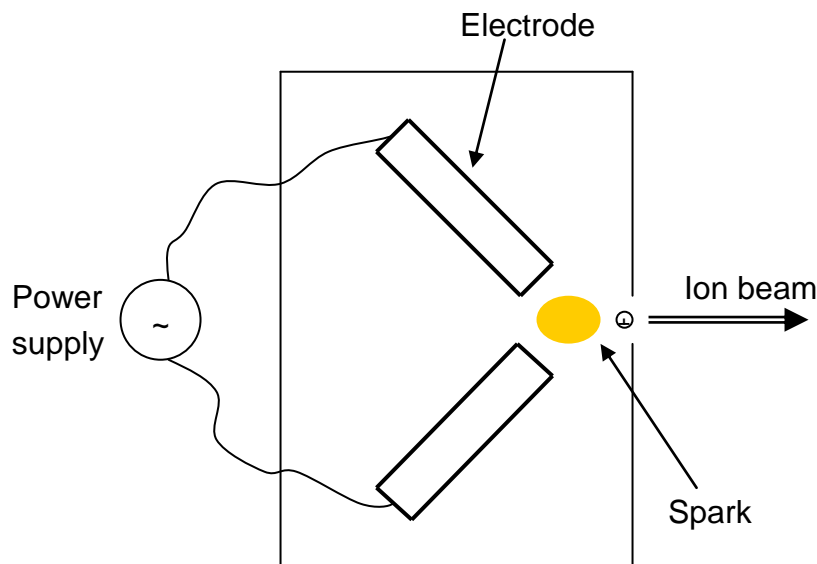
Figure 1-2 Schematic diagram of a spark source.

A spark source is particularly effective at generating gas ions from a solid sample. Shown

in Figure 1-2 is the schematic diagram of spark source. Two electrodes are mounted in a vacuum

chamber. A pulsed several kilovolt typically AC potential is applied across a small gap between

two electrodes and produces an electrical discharge. Such electrical discharges produce hot spots

on the electrodes from which atoms and molecules are evaporated and sputtered into the space

between the two electrodes.[47] The electrons in this space produce ions through electron

bombardment, generating mainly singly charged, atomic ions.[37] Solid samples can be

incorporated into graphite electrodes and ionized by the intermittent spark generated between two electrodes. If the sample is a metal, it may serve as one of the two electrodes. Typically spark source mass spectrometry is used to determine the abundance of the various elements in the sample.[34]

1.2.1.3. Glow Discharge Ionization
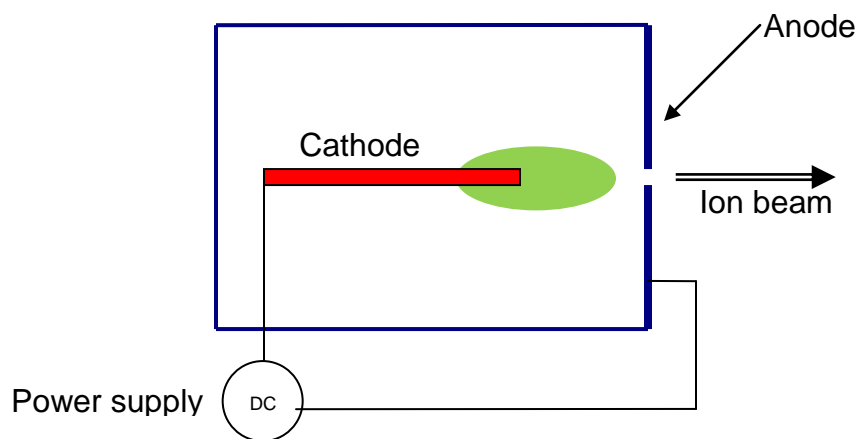
Figure 1-3 Schematic diagram of a glow discharge source.

Glow discharge (GD) ionization is a method used to sputter and ionize compounds from solid surfaces. GD has been widely applied to the analysis of metals, alloys, and high purity inorganic materials.[48] A glow discharge source is indicated schematically in Figure 1-3. This source consists of a cathode and an anode in a low-pressure (0.1-10 Torr) noble gas such as argon. The cathode is formed as a metal pin and the stainless steel anode contains the ion exit aperture. Samples are introduced into the glow discharge source as the cathode material itself or a layer of material deposited on the surface of the cathode. A simple DC power supply provides a voltage of about -1000 V to the cathode with a discharge current to 1-5 mA.[34, 37] For a given

discharge voltage and gas pressure, argon is ionized, and electrons and positive ions are accelerated towards the oppositely charged electrodes. Both ionic and neutral argon interact with the surface of the cathode by bombardment, creating a collision cascade with sufficient energy to remove atoms from the surface. Neutral atoms are then sputtered into the glow region of the discharge from the surface of the cathode where they are ionized or excited by collisions with metastable argon atoms or electrons.[49]

1.2.1.4. Inductively Coupled Plasma Ionization

Inductively coupled plasma (ICP) ionization is widely used to produce atomic ions. ICP mass spectrometry (ICP-MS) is used for elemental analysis of both solid and liquid samples.[34] A high temperature plasma in argon gas is used to atomize and ionize samples. Solid samples are ablated by a pulsed laser and introduced into the plasma torch by the argon carrier gas. A nebulizer is used to introduce aqueous samples into the torch as a fine mist.[37] The plasma torch consists of concentric quartz tubes. The inner tube contains the sample aerosol and argon, and an argon gas flow is in the outer tube to cool the tubes. A coupling coil that wraps around the tubes is used to transmit radio frequency energy applied to the coil to argon through an oscillating electromagnetic field. Argon inside the inner tube is heated by energy transferred from the outer induction region and becomes argon plasma with a temperature around 10,000 K, that atomizes and ionizes the sample. Analysis of major, minor, trace, and ultra-trace element concentrations at levels below part per trillion (ppt) can be realized by ICP-MS.[50]

1.2.1.5. Chemical Ionization

Although electron ionization is simple and sensitive for small molecules analysis, it suffers from the drawback that only volatile molecules can be analyzed. A further limitation of EI is the requirement that stable neutral molecules must be in the gas phase before ionization. At the same time, EI induces fragmentation of the molecular ion, which can prevent the detection of the molecular ion for larger molecules. For some volatile compounds that do not give molecular ions in the EI mass spectrum, chemical ionization (CI), which was developed in the 1960s,[51] is an especially useful technique to ionize such molecules. A spectrum with less fragmentation is obtained with the CI technique.[37]

The ion source for chemical ionization is similar to that of EI but the working pressure is around 1 Torr due to the reagent gas, such as methane, isobutene, or ammonia, in the ion source chamber. The bombardment of the reagent gas with a beam of 200-500 eV electrons produces reagent ions that react with the analyte to form ions. The reagent gas is present in large excess compared to the analyte in the ion source.[34, 52]

If methane is introduced into a CI ion source as the reagent gas, the principle of chemical ionization can be illustrated with the following reactions. The electron beam ionizes methane by electron ionization:

$$CH_4 + e^- \rightarrow CH_4^{\bullet+} + 2e^- \qquad\qquad (Eq.\ 1\text{-}2)$$

This molecular ion will fragment, mainly through the following reaction:

11

$$CH_4^{\bullet+} \rightarrow CH_3^+ + H^{\bullet} \qquad\qquad\qquad\qquad\qquad \text{(Eq. 1-3)}$$

$$CH_4^{\bullet+} \rightarrow CH_2^+ + H_2 \qquad\qquad\qquad\qquad\qquad \text{(Eq. 1-4)}$$

One or more secondary reagent ions are formed by ion-molecule reactions. Sometimes the initially formed reagent ions are not stable. Thermally stable reagent ions are produced by the collisions between the initially formed reagent ions and neutral reagent gas molecules:[52]

$$CH_4 + CH_4^{\bullet+} \rightarrow CH_5^+ + CH_3^{\bullet} \qquad\qquad\qquad \text{(Eq. 1-5)}$$

$$CH_4 + CH_3^+ \rightarrow C_2H_5^+ + H_2 \qquad\qquad\qquad\quad \text{(Eq. 1-6)}$$

The reagent gas produces a set of ions that can undergo exoergic ion-molecule reactions with the sample of interest under a high reagent gas pressure. Ions are produced through the reaction of the analyte with ions of the reagent gas.[34] There are four general pathways to form product ions from a neutral analyte molecule M in CI with methane gas:[53]

$$M + CH_5^+ \rightarrow CH_4 + [M+H]^+ \qquad \textit{proton transfer} \qquad \text{(Eq. 1-7)}$$

$$M + CH_5^+ \rightarrow [M+ CH_5]^+ \qquad \textit{electrophilic addition} \qquad \text{(Eq. 1-8)}$$

$$M + CH_3^+ \rightarrow CH_4 + [M-H]^+ \qquad \textit{hydride abstraction} \qquad \text{(Eq. 1-9)}$$

$$M + CH_4^+ \rightarrow M^+ + CH_4 \qquad \textit{charge exchange} \qquad \text{(Eq. 1-10)}$$

The analyte molecule will react mostly through proton transfer reaction, a gas-phase acid-base process if the proton affinity of analyte molecule is greater than that of methane. Moreover, attachment of complete reagent ions to the analyte molecule is sometimes observed, which is a type of gas-phase solvation.[54] Studies have shown that the main ionizing reactions of molecules

containing heteroatoms occurr through acid-base reactions with $C_2H_5^+$ and CH_3^+.[37, 55] The

hydride abstraction to form $[M-H]^+$ is also observed for saturated hydrocarbon compounds.[52]

Charge exchange yields radical ions of low internal energy which behave similarly to molecular

ions in low-energy electron ionization.[56]

1.2.2. Ionization of Large Molecules

Although the ionization methods mentioned above have been widely used, they are only

suitable for gas-phase ionization of volatile compounds with small molecular masses of a few

hundred dalton (Da), or for elemental analysis.[46] For large molecules such as biological

compounds and synthetic polymers, soft ionization techniques have been developed for those

nonvolatile and thermally labile samples.[3, 10, 57] Spray ionization and desorption ionization are

major soft ionization techniques applied to the analysis of nonvolatile large molecules as well as

other polar and involatile compounds.[58]

<u>1.2.2.1. Spray Ionization</u>

Spray ionization is a method for direct introduction of samples in solution. Ions from a

sample solution are generated in a spray process that is typically at ambient pressure. The solvent

can be selectively vaporized before the sample ions enter the mass spectrometry vacuum system.

1.2.2.1.1. Atmospheric Pressure Chemical Ionization

Unlike chemical ionization working at around 1 Torr, atmospheric pressure chemical

ionization (APCI) is an ionization technique adapted to a spray ion source using gas phase

13

ion-molecule reactions at atmospheric pressure with the vaporized solvent acting at the reagent gas.[37] The schematic diagram of an APCI source is shown is Figure 1-4. A high flow rate of analyte (0.2-2 mL/min) in solution is introduced directly into a pneumatic nebulizer where it is sprayed into aerosol cloud by high flow rates of an inert gas such as nitrogen. The spray droplets then are displaced by the gas flow through a heated chamber (about 120 oC) and the solvent evaporates. The gas is subjected to a corona discharge where ionization occurs.
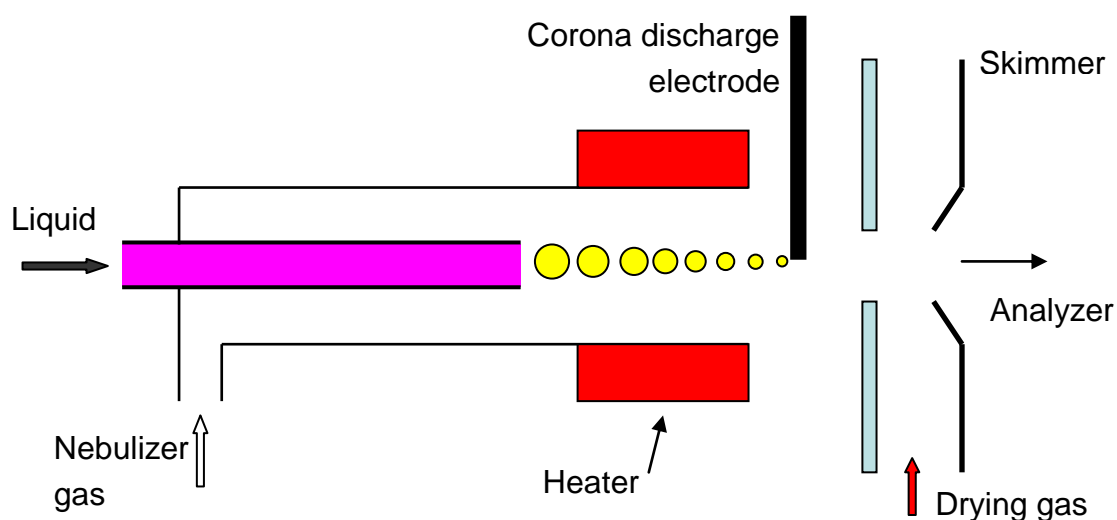
Figure 1-4 Schematic diagram of an atmospheric pressure chemical ionization source.

The ionization processes in APCI is similar to the processes of ionization for CI noted above except that they occur at atmospheric pressure. Primary ions such as $N_2^{\bullet+}$ or $O_2^{\bullet+}$ are formed by corona discharge.[37] Then, primary ions collide with gaseous solvent molecules to form secondary reactant gas ions. Ions of molecular species are produced through the reaction of the analyte molecules with reagent gas ions.

1.2.2.1.2. Electrospray Ionization
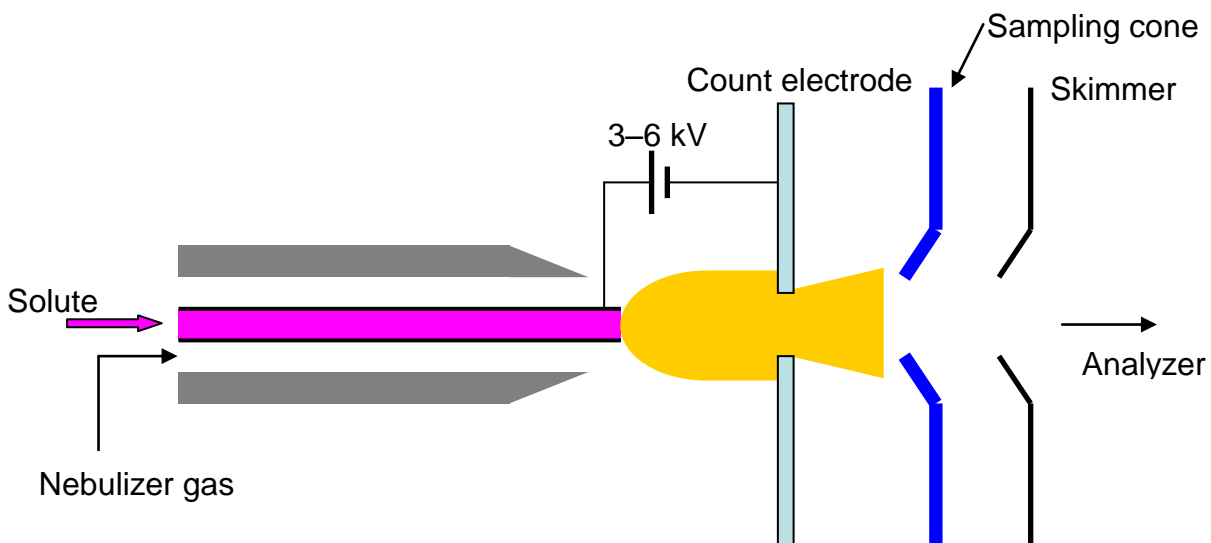
Figure 1-5 Illustration of electrospray ionization.

Like APCI, electrospray ionization (ESI) is an atmospheric pressure ionization (API) source.

However, ESI is better for polar and high molecular weight molecules compared to APCI.[59]

Shown in Figure 1-5 is the schematic diagram of an ESI source. High molecular mass samples (>

1000 Da) such as peptides and proteins are ideally suited to electrospray ionization.[60-61] A

sample liquid containing the analyte passes through a stainless steel capillary (75-100 μm

internal diameter) and is sprayed under an electric field, which is obtained by applying a

potential difference of 3-6 kV between the capillary and the counter-electrode.[46] Charge

accumulation is induced by the electric field at the liquid surface located at the end of the

capillary. A mist of fine charged droplets is formed in the spray process under the electric field.

In the presence of a flow of heated nitrogen to assist desolvation, solvent is evaporated from the

charged droplets leading to the decrease of droplet size. Due to the size decrease, the charge density at the surface of the droplets increases until the repulsive Coulombic forces exceed the droplet surface tension, which causes the droplets to break into smaller and highly charged offspring droplets.[52] The solvent evaporation and droplet fission is repeated several times until the surface charge density is high enough to overcome the droplet cohesive forces inducing direct ion desorption.[10, 52] Multiply charged ions are formed during the process of electrospray ionization. The reduced mass-to-charge ratio induced by multiple charging allows mass spectra to be obtained for large molecules.[62]

1.2.2.2. Desorption Ionization

In desorption ionization, energy is rapidly added to a condensed-phase sample by bombardment with ions, atoms, or photons.[58] A plume with high concentration of the gas-phase neutral and ionic species, clusters, and particles is formed above the point of impact. Typically, even-electron ions such as protonated molecules $[M+H]^+$, deprotonated molecules $[M{-}H]^-$, or cationized molecules $[M+Na]^+$ are produced by desorption ionization.[58]

1.2.2.2.1. Field Desorption

Unlike other desorption ionization methods, there is no a high-energy particle beam used to bombard a sample in field desorption (FD). The schematic diagram of a FD source is shown in Figure 1-6. A small filament with crystalline "whiskers" (approximately 1 μm diameter) grown on the surface is held about 1 mm away from a grounded cathode in a vacuum chamber. The

16

sample is deposited onto the filament before it is inserted into the vacuum. A high positive

potential (~5 kV) relative to the cathode is applied on the filament, which lead to a strong electric

field gradient (up to 10^{10} V/cm) existing near the tips of the "whiskers".[34] A current passes

through the filament and the sample is heated to induce desorption. The high electric field at the

whisker tip distorts the electron cloud of the sample molecules, and decreases the barrier for

single electron removal from the molecule by quantum-mechanical tunneling.[34] After removal of

the electron from the molecule, the $M^{+\bullet}$ ion is left behind. The ion-molecule reactions of sample

molecules with $M^{+\bullet}$ produce $[M+H]^+$ ions. Due to the presence of cationic impurities, ions such

as $[M+Na]^+$ can also be generated.[37, 52]
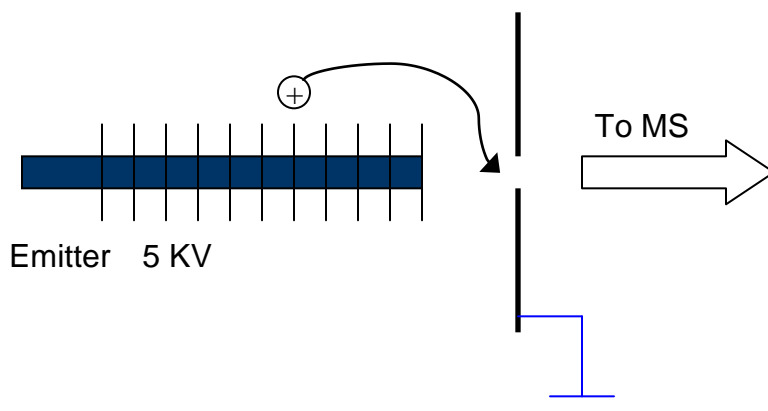
Figure 1-6 Schematic diagram of field desorption source.

1.2.2.2.2. Plasma Desorption Ionization

   Plasma desorption (PD) is used for the ionization of nonvolatile and thermally

unstable molecules, including proteins and peptides.[63] In PD ionization, the sample is deposited

onto a 0.5-1.0 µm metal foil.[64] A high-energy ion beam bombards the sample foil from the back

side and the energetic ions penetrate the foil inducing desorption of sample ions. These

high-energy ions are the fission fragments of a radioactive element such as ^{252}Cf with energies

on the order of 100 MeV, for example ^{142}Ba^{18+} and ^{106}Tc^{22+}.[63] A few thousand fission fragments

bombard the sample per second and dissipate their high kinetic energy. Protonated molecules

with different charge states and neutrals are desorbed from the sample surface.[37, 52] The peaks in

a PD spectrum are generally broad because of metastable decomposition of the ions in flight.

With the development of other soft ionization techniques, PD has been largely supplanted by

MALDI and electrospray.[34]

1.2.2.2.3. Secondary Ion Mass Spectrometry

Secondary ion mass spectrometry (SIMS) is used for the composition analysis of a solid

surface through ejected secondary ions when the surface is irradiated with a beam of high-energy

(~10 keV) ions, usually argon ions.[65] The Ar$^+$ ions transfer energy to sample molecules in a

series of collisions. Sample molecules recoil back through the sample surface and lead to more

collisions among sample molecules, thus producing surface sputtering of secondary particles.[66]

Among the ejected secondary particles are neutral species such as atoms, molecules, clusters and

particles, as well as positively and negatively charged species. High vacuum with pressure below

10^{-6} Torr is required in the ion source to ensure no collision between secondary ions and the

background gas.

Two major variants of SIMS, static and dynamic, are applied for different measurements.[37] Ion sources with pulsed primary ion beams of low current in the range of $10^{-10} - 10^{-9}$ A/cm² are called static SIMS because the surface of the sample is not damaged. Surface atomic monolayer analysis is involved in static SIMS. Dynamic SIMS is applied for bulk analysis, using a continuous primary ion beam that produces surface erosion of the sample. Analysis with dynamic SIMS can provide a lateral resolution of 5 nm. Compared with dynamic SIMS, static SIMS causes less damage to molecules on the surface.

1.2.2.2.4. Fast Atom Bombardment

Fast atom bombardment (FAB) is similar to static SMIS but the analyte is dissolved in a non-volatile liquid matrix such as glycerol or 3-nitrobenzyl alcohol (NBA), which protects the analyte from damage by the impact of a high-energy (about 5 keV) atom beam. The neutral atoms in the beam originate from ionized argon or xenon atoms. The Ar or Xe ions are accelerated to about 5 keV and go through a cell filled excess neutral gas atoms where the ions exchange their charge with the neutrals. Thus, high-energy ions are converted to fast atoms with sufficient momentum to bombard the mixture of analyte and matrix.[37, 52] Using neutral atoms instead of ions avoids accumulation of charge on non-conducting samples. Part of the momentum of the fast moving atom beam is transferred to the analyte and matrix molecules by impact on the liquid mixture.[52] High temperature and high density supercritical gas at the point of impact is generated when the energy density is sufficiently large.[67] A intermediate pressure

region between the liquid surface and mass spectrometry vacuum is formed.[52] Positive and negative ions are ejected from the surface. Additional ionization takes place in the selvedge region and continues in the gas phase by the desolvation of ion-solvent clusters and ion-molecule reactions.[52] FAB ionization produces primarily intact protonated molecules $[M+H]^+$ and deprotonated molecules $[M-H]^-$.[57]

1.2.2.2.5. Laser Desorption Ionization

Laser desorption ionization (LDI) is a technique using a pulsed laser beam to deposit energy into a sample inducing desorption of molecules into the gas phase and produce gaseous ions.[37] The sample exposed to the laser pulse is heated quickly and its internal energy increases in a short time, leading to melting, vaporization, ionization, and possibly some decomposition. Ions, neutral molecules, and particles are removed from the sample surface as a plume. In LDI, the energy transfer directly from laser pulse to the sample molecules can induce fragmentation, which limits it application to relatively small molecules. The physical proprieties of the sample determine the fragmentation observed in the mass spectra.[37]

1.2.2.2.6. Matrix-assisted Laser Desorption Ionization

In MALDI, analytes are embedded in a molar excess of matrix, so that analytes are isolated from one other and sample aggregation is prevented. The MALDI matrix strongly absorbs the light at the laser wavelength and also aids in ionization. A pulsed laser irradiates the mixture of analyte and matrix, and rapidly transfers energy into the condensed phase through excitation of

the matrix molecules.[37] Localized sublimation of the matrix and expansion of the matrix into the

gas phase are induced by the rapid addition of energy. Thus, little internal energy is transferred to

the analyte molecules, which protects the analyte from being damaged by direct absorption of

photons.[68] Analyte ions are formed in the expanding plume and the resulting ions of both matrix

and analyte are detected in a mass spectrometer.
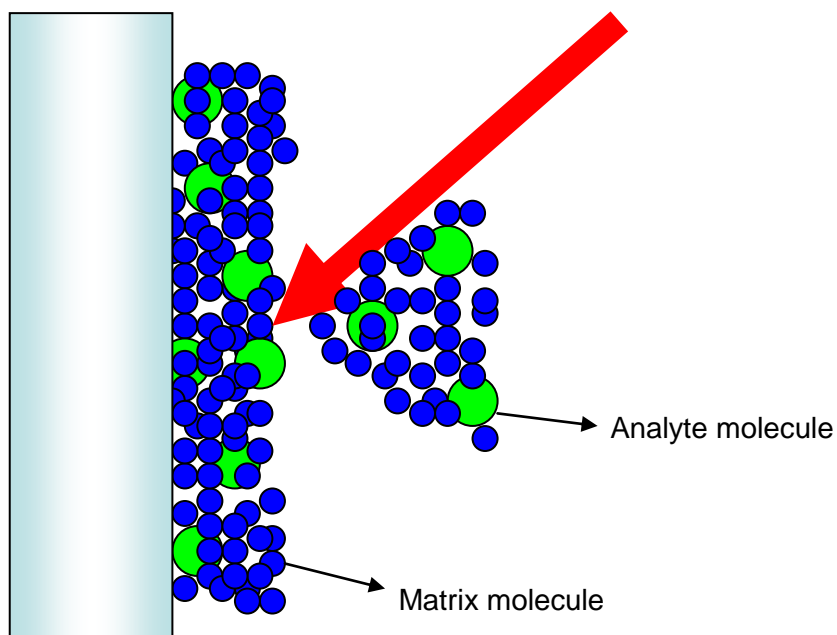
Figure 1-7 Illustration of matrix assisted laser desorption/ionization.

Pulsed ultraviolet lasers, such as 337 nm nitrogen lasers and 355 nm frequency-tripled and

266 nm quadrupled Nd:YAG lasers have been widely used for MALDI mass spectrometry.[4] The

electronic excitation induced by the laser pulse can then relax through a variety of radiative or

non-radiative processes, leading to bond-breaking and ejection of atoms, ions, molecules and

even particles.[69]

Infrared lasers can also be used.[70] Laser energy of pulsed infrared lasers is absorbed by vibrational modes of the matrix molecule.[14] Fixed wavelength Er:YAG (2.94 μm) and CO_2 lasers (10.6 μm) have been employed since early 1990s.[71] More recently, tunable IR wavelength sources such as optical parametric oscillators (OPO) have been introduced.[72-73] Due to the lower absorbance of the IR laser radiation, the fluence required for IR laser material removal and ion formation is approximately ten times higher than the UV.[74] From Beer's law (Eq. 1-18), the relatively low optical absorption of IR-MALDI matrix means that an IR laser can penetrate deeper into the sample than a UV laser. More material is removed in IR-MALDI compared with UV-MALDI.[22] The wavelength dependence of IR-MALDI is quite pronounced in contrast to UV-MALDI. In some cases a change in wavelength for only 10 nm is sufficient to move from a wavelength region that can be used for IR MALDI to one that cannot.[73]

To better understand the ionization mechanisms of MALDI, it is important to distinguish the ionization of the analytes and that of the matrix molecules. Two general models have been proposed.[11-12, 68] One model treats the physical processes of desorption or ablation of material separately from the chemical process of ionization of the analyte.[11] In this model, photoionization of the matrix molecules occurs in the first few nanoseconds after the laser pulse.[75] Aside from positive ions, reactions between photoelectrons and neutral matrix molecules generate the negative species.[76] Radical matrix ions such as $M^{+\bullet}$, and even-electron ions such as $[M+H]^+$ or $[M-H]^-$ are formed.[68] Acid-base charge transfer from matrix ions to the analyte

molecules in the expanding plume of ejected material leads to the ionization of analyte molecules.[11, 76] The photochemical ionization processes are shown in the following (M: analyte, AH: matrix):[76]

$$AH + hv \rightarrow AH^{+\bullet}; \quad AH^{+\bullet} + M \rightarrow (M+H)^{+} + A^{\bullet} \quad \text{(Eq. 1-11)}$$

$$AH + hv \rightarrow AH^{-\bullet}; \quad AH^{-\bullet} + M \rightarrow (M-H)^{-} + (AH+H)^{\bullet} \quad \text{(Eq. 1-12)}$$
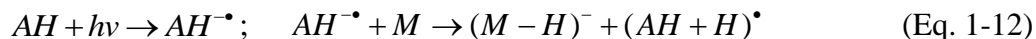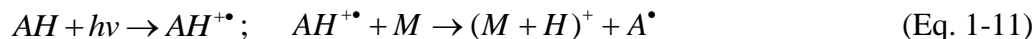
A competing view postulates that the desorption and ionization occur together during the ejection of clusters and particles.[12] This model proposes that analyte molecules retain their solution charge state upon incorporation into the matrix. This assumption is supported by experimental results where pH-indicator molecules retain their color and charge state upon crystal incorporation for acidic, neutral, or basic matrices.[31] The analyte molecules are entrained in a dense plume of the desorbed matrix clusters. Due to the desorption, a break-up of the crystal lattice into small clusters is assumed and some clusters are assumed to carry a positive or negative charge.[68] The clusters transfer protons to the analyte molecules in the expanding plume and are assumed to lose neutral matrix as well as counter ions as free acids or bases.[68] The model explains why mostly singly charged ions are observed in both UV and IR MALDI spectra. The possible reactions are provided in the following (M: analyte, AH: matrix, An: anion, Ba: base, shown in the bracket is a cluster):[12]

$$\{(M+nH)^{n+} + (n-1)An^{-} + xAH\} \rightarrow [M+H]^{+} + (n-1)HAn + xAH \quad \text{(Eq. 1-13)}$$

$$\{(M-nH)^{n-} + (n-1)BaH^{+} + xAH\} \rightarrow [M-H]^{-} + (n-1)Ba + xAH \quad \text{(Eq. 1-14)}$$
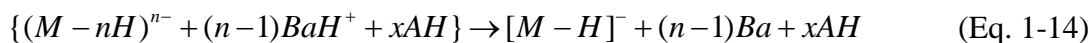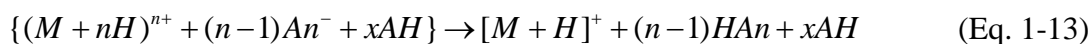
Ambient ionization is a method where ions are generated outside of the mass spectrometer at atmospheric pressure with minimum or without sample pretreatment.[77] In ambient ionization, material is liberated from condensed phase samples which are interacted with ions or charged droplets, sometimes coupled with a laser. Since most ambient ionization techniques are noninvasive in sampling, they are ideal for analysis of the surface composition of different condensed phase samples.[78] Ambient ionization has been widely applied in many areas, such as biomedicine, food safety, antiterrorism, pharmaceuticals, and environmental pollution.[79]

1.2.2.3.1. Desorption Electrospray Ionization
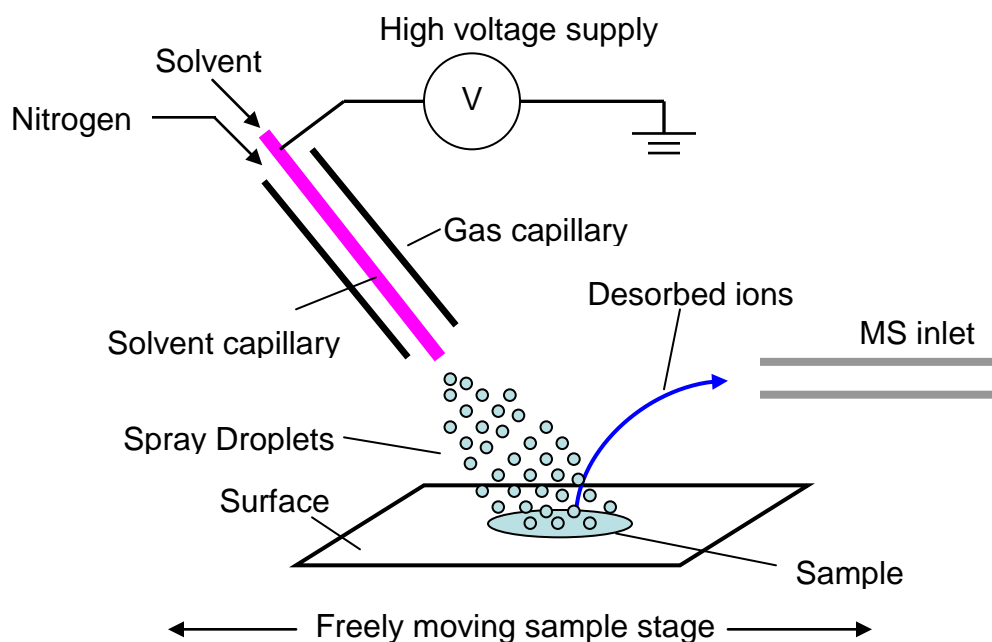
Figure 1-8 Schematic diagram of a desorption electrospray ionization source.

Desorption electrospray ionization (DESI) was first reported in 2004.[80] It is a variant of electrospray where ionization is carried out by directing pneumatically assisted electrosprayed

droplets onto a sample surface. The charged solvent on the sample surface is then lifted off as secondary charged droplets. The analyte is picked up while in contact with the charged solvent, and subsequently form analyte ions that are delivered to a mass spectrometer. The ionization efficiency of DESI depends on the chemical composition of sample and sprayed solvent, as well as the parameters of the instrumental setup, such as electrospray voltage, gas and liquid flow rates, and spray angle and ion uptake angle.[81] A schematic diagram of a DESI source is shown in Figure 1-8.

1.2.2.3.2. Direct Analysis in Real Time

In direct analysis in real time (DART), ionization can take place when the sample surface is exposed to a stream of metastable species containing excited state atoms and molecules.[82] A glow discharge with potential in the range of 1 to 5 kV is created to form a plasma in nitrogen or helium gas containing ionized gas, electrons, and metastable species. The plasma passes through electrostatic lenses, which remove charged particles. The remaining metastable species are aimed directly at the sample, which can be a solid, liquid or gas, to desorb and ionize the analyte.

In ionization processes of DART, energy is transferred from an excited state gas species (A^*) to an analyte molecule (M). According to Penning ionization,[83] a radical molecular cation $M^{+\bullet}$ and an electron will be produced, if the ionization potential of the analyte (M) is lower than the energy of the excited state species (A*).

$$A^* + M \rightarrow A + M^{+\bullet} + e^- \qquad\qquad\qquad \text{(Eq. 1-15)}$$

While helium is used in the source of DART, water cluster ions are generated according to

$$He^* + nH_2O \rightarrow He + (H_2O)_{n-1}H^+ + OH^- \qquad \text{(Eq. 1-16)}$$
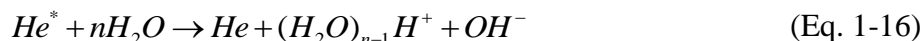
Protonated molecules are generated by the reaction between cluster ions and desorbed analytes.

$$(H_2O)_{n-1}H^+ + M \rightarrow [M + H]^+ + (H_2O)_{n-1} \qquad \text{(Eq. 1-17)}$$

1.2.2.3.3. Atmospheric Pressure Matrix-assisted Laser Desorption Ionization

Atmospheric pressure matrix-assisted laser desorption/ionization (AP-MALDI) is an ambient variant of MALDI. AP-MALDI works in a similar manner to vacuum MALDI whereby a laser is used to irradiate sample consisting of matrix and analyte in open air. Unlike vacuum MALDI, the ion source and the mass analyzer in AP-MALDI are decoupled, which makes AP-MALDI a quasi-continuous source. Desorption and ionization takes place at atmospheric pressure and the resulting ions are sampled into the mass spectrometer through a small orifice, similar to that used for ESI.[84] AP-MALDI eliminates some of the drawbacks of vacuum MALDI, such as mass resolution at high laser fluence and sample handling.[5] One of the unique characteristics of AP-MALDI is that it is an even softer ionization technique than vacuum MALDI because of the collisional cooling of the expanding plume and fast thermalization of the ion internal energy.[85] This feature makes AP-MALDI a particularly useful technique in the analysis of labile biomolecules and non-covalent complexes.[86]

1.2.2.3.4. MALDESI and ELDI

An electrospray ionization source can be combined with a pulsed laser to realize ionization.

The pulsed laser irradiates a condensed phase sample, and desorbs gas molecules and ablates particles that are ejected upward in a plume of material. The ejected neutral molecules are entrained in the charged electrospray droplets and the ablated particles merge with the electrospray. The interactions between the charged droplets and neutral molecules/particles induce the formation of analyte ions under ambient conditions.[18] The use of the laser with the ESI separates the location of desorption from that of ion formation. The ionization of ablated particles and gas molecules by the ESI source yields multiply-charged ions.[6-7] If a matrix is mixed with the analyte, this method is called matrix assisted laser desorption electrospray ionization (MALDESI).[7] If there is no matrix, it is called laser desorption electrospray ionization (LDESI).[6] Both UV and IR laser have been used in MALDESI and LDESI.[6-8, 18] Shown in Figure 1-9 is the schematic diagram of an IR-MALDESI/LDESI ion source.
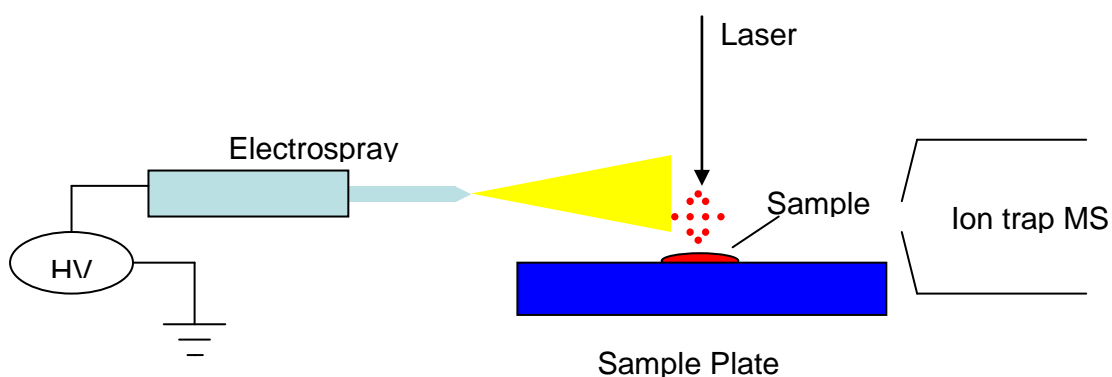
Figure 1-9 Schematic diagram of IR-MALDESI/LDESI.

1.3. The Physics of Laser Desorption and Ablation

Although laser desorption ionization is broadly applied in many fields, the fundamental

studies aimed at understanding the processes involved in material desorption, ablation, and ion formation needs to be better understood for the best application of current techniques.

Laser desorption and ablation involves the transfer of material from a condensed sample to the gas phase using a pulsed laser. Laser desorption refers to laser-induced thermal evaporation of individual molecules from the outermost layers of the sample.[13, 15] While the energy of pulsed laser is increased, particles can be removed from the upper layers of a surface and transferred into the gas phase by laser-induced nonthermal processes, for example photomechanical stress or bond-breaking, which is called laser ablation.[13, 15] More material removal occurs in laser ablation compared to laser desorption. The material ejection process is strongly dependent on the irradiation parameters, including pulse width, laser fluence and wavelength, as well as optical and thermomechanical properties of the material, such as thermal diffusivity, tensile strength, and wavelength dependent absorption coefficient.[13, 87]

1.3.1. Physical Processes of Energy Deposition

1.3.1.1. Energy Deposition

It is critically important to match the laser parameters such as wavelength, fluence, and pulse duration, with the thermal and optical properties of the sample.[15] Energy deposition from the laser to the material is strongly affected by the optical properties of material at the wavelength of the laser radiation. The optical absorption of the material from the laser beam is governed by Beer's law.[88]

$$H = H_0 e^{-\alpha z}$$
(Eq. 1-18)

where H_0 is the laser fluence at the sample surface, H is the laser fluence at depth z in the sample. α is the attenuation coefficient, which is the product of the molar absorption coefficient α_n and the concentration of the absorbing molecules c_n in the sample. The molar absorption coefficient α_n is a wavelength dependent property.[88]

In addition to the laser energy and the optical properties of the material, the rate that the energy supplied by the laser pulse is an important parameter affecting laser ablation.[89] If the laser energy is deposited quickly, a condition known as stress confinement is obtained, in which the rate of energy flow into the sample exceeds the rate of energy loss through the collective molecular motion (acoustic waves).[87] In this regime, a high pressure builds up within the absorbing region and propagates from the absorption region into the surrounding sample. If the resulting pressure exceeds the dynamic tensile strength of the sample material, this leads to mechanical fracture, which is called spallation.[90] For longer laser pulses, the absorbed energy is redistributed by thermal conduction during the laser pulse. If rate of energy flow into the sample exceeds the rate of removal by thermal diffusion, this is called thermal confinement.[22, 87] At same fluence, high speed photography of the ablation plume shows lift-off of the entire irradiated layer under stress confinement conditions compared to a less dense plume of material created under thermal confinement conditions.[27]
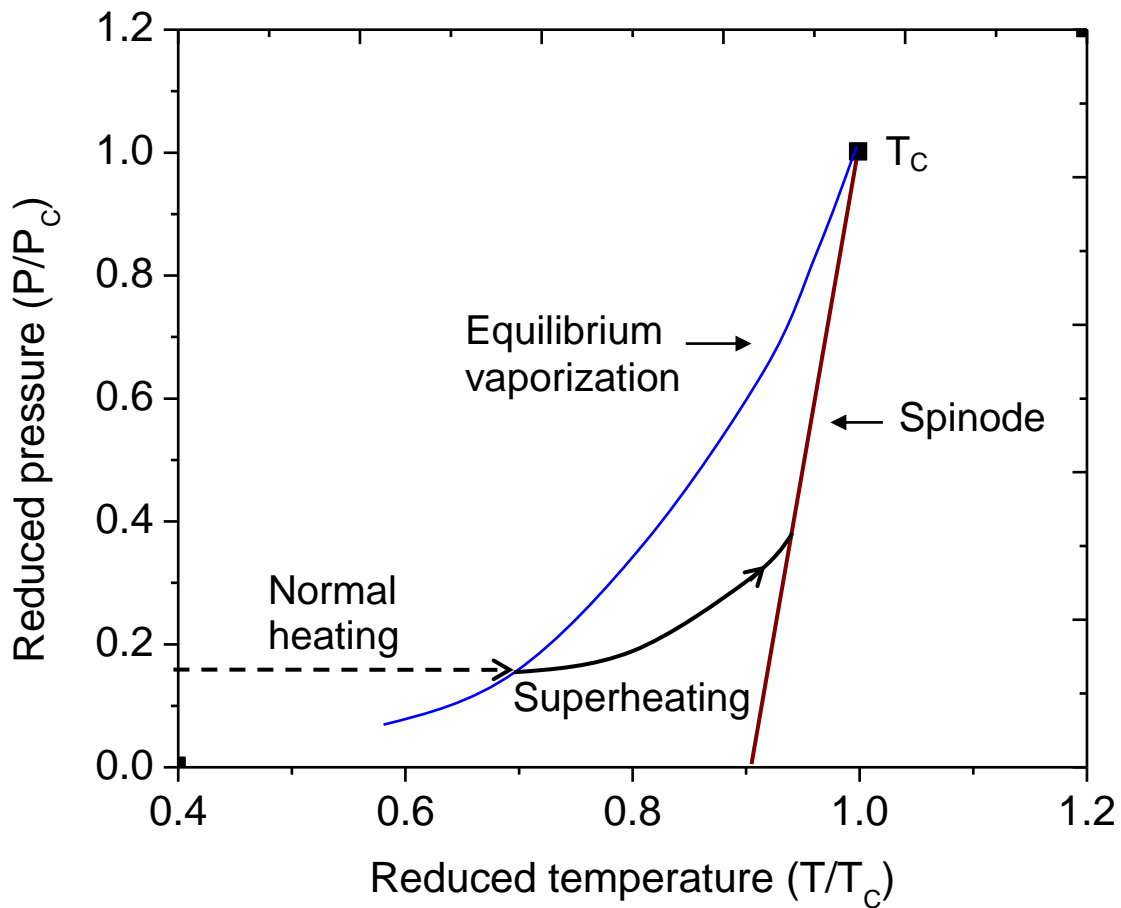
Figure 1-10 Phase diagram near the critical point indicating normal heating and superheating.

A distinct feature of material ejection as a function of laser energy is the large increase in the total amount of the ejected material at a threshold fluence. In the fluence regime below threshold, the surface layer of the material is heated and individual molecules are desorbed and ejected by thermal desorption.[91] At threshold, the onset of particle ejection is responsible for the jump in the total material removal.[89]

Figure 1-10 shows a phase diagram indicating normal heating and superheating, which can be used to illustrate the heating process of a liquid material by a pulsed laser. In a normal heating process, when temperature of the material reaches the boiling temperature, the liquid and the vapor phases are in equilibrium (equilibrium vaporization line).[92] As the fluence increases, energy deposition from the laser pulse can induce heating at rates in excess of 10^6 K/s.[15] It is possible to superheat the liquid above the boiling point. If the temperature exceeds 90% of the critical temperature T_c, the phase of superheated material breaks through the spinode line, the upper boundary of metastable equilibrium.[92] The superheated liquid material becomes unstable and catastrophically relaxes to a liquid-vapor mixture.[91, 93] Under these conditions, phase explosion occurs, which transits the superheated liquid to a mixture of gas phase molecules, clusters, and liquid droplets.[92] By the overheating of the absorbing volume, a plume of ejected material is formed.[15, 94]

Phase explosion can occur in both the thermal confinement and the stress confinement regimes. In the thermal confinement regime, the threshold fluence for laser ablation is defined as the energy that overheats the sample surface up to the limit of metastable equilibrium, leading to the ejection of a mixture of vapor, clusters, and particles.[94-96] Compared with thermal confinement, the particles ejected in the stress confinement regime are larger and more numerous.[89, 97-99] Plume ejection can be caused by the combination of phase explosion and stress

confinement. In molecular dynamics simulations, the threshold fluence for phase explosion

under stress confinement was found to be 22% lower than the regime of thermal confinement. [87]

1.3.1.3. Wavelength Effects

According to Beer's law, wavelength dependence of laser desorption and ablation is

governed by the attenuation coefficient of the material. Wavelength has a dramatic effect on the

quantity of material ablated and on the ablation rate. For UV laser ablation, the laser ablation was

compared at 193, 213 and 266 nm using a 1064nm Nd:YAG laser source for harmonic

generation and an optical parametric oscillator.[100] The ablation rate obtained for a sample with

higher optical absorption is greater than that measured for a lower optical absorption sample. In

the IR region, the wavelength dependence is pronounced and roughly tracks the IR absorption

spectrum of the matrix material.[101-102] In another study, a wavelength-tunable pulsed IR laser was

used to irradiate thin films of glycerol at atmospheric pressure at a limited wavelength range

between 2.95 and 3.1 μm.[22] The mean particle diameter ranged between 900 and 1600 nm.

Although the accessible wavelength range was limited, there were hints that the diameter of the

ablated particles tracked the IR absorption of the glycerol. At 3.0 mm, where glycerol has a

strong IR absorption due to the OH stretch vibration, the observed particles were the smallest

with a mean diameter of 900 nm. At 0.1 μm higher or lower wavelength, the mean particle

diameter was about 20% larger. These results are consistent with an explosive phase transition in

the stress confinement regime, in which the laser energy is deposited more rapidly than it can be removed through collective molecular motion (acoustic waves).[24, 87, 103]

1.3.2. Ablation Plume Evolution

Measurements of the dynamic distributions of the ejected ions, neutral molecules, and particles, form the fundamental investigations for laser desorption and ablation. Two factors determine the characteristic of ablation plume: plume composition and temporal evolution of the plume.[13]

The abundance of ions, neutral molecules, and particles, as well as the particle size distribution, have a strong dependence on the laser irradiation conditions, such as incident laser fluence, pulse width, laser wavelength, irradiation spot size, and ambient gas pressure.[104-105] In the ablation plume, smaller particles are formed by condensation in the expanding plume and relatively larger ones by the ejection of melted material or photomechanical sputtering.[87, 98] Smaller particles are tens of nanometers or less whereas larger particles are those approaching 100 nm in size.

The dynamics of the expanding material plume includes the temporal regimes of condensed phase disintegration, the collisions among plume components and between the the ambient gas and plume components, and intermolecular reactions.[13] The radial (parallel to the sample surface) and axial (normal to the surface) velocity distributions of the expending plume describe the characteristic dynamic evolution.[106] The spread in the radial velocities can be described by the

thermal motion in the plume, because the radial velocity distributions have been found to fit well

to a Maxwell-Boltzmann distribution.[98, 106] Compared to the distribution of the radial velocity, a

considerably broader distribution of the axial velocity of ejected molecules and particles has

been found due to the relaxation of laser induced pressure.[107]

Laser desorption and ablation have been used under both vacuum and ambient conditions

depending on the purpose. Compared to the expansion into a vacuum, the interaction between the

plume species and the ambient gas is a relativly complex gas phase dynamic process. In a

vacuum or at low background pressure ($< 10^{-2}$ Torr), the ablation plume expands freely.[27, 105]

With the increase of ambient gas pressure, some physical processes such as attenuation,

deceleration, recombination, and formation of shock waves are involved.[105] The interaction of

the plume with the ambient gas induces a partial energy conversion from kinetic energy to heat

which in turn increases the temperature of the plume.[105] The velocity of expanding plume drops

because of numerous collisions with ambient gas molecules.

1.4. Experimental Investigations of Laser Desorption

To investigate the physical process and mechanism of laser desorption and ablation, some

experimental methods and procedures have been applied in previous studies.

1.4.1. Particle Counting and Size Measurement

1.4.1.1. Microscopy

Microscopy has been applied to particle analysis using laser microprobe mass analysis

(LAMMA), which utilizes a pulsed laser to desorb and create ions from collected particles.[108] Particles were mounted on a transmission electron microscopy (TEM) grid coated with a thin organic or metal supporting foil (≤ 0.1 μm) in a vacuum (about 10^{-6} Torr) chamber.[109] The ions were extracted into a mass analyzer to to obtain a mass spectrum A high-resolution optical microscope was used to observe the size distribution, morphology, chemical composition, and even the surface composition of particles.[108]

Another method using microscopy was applied to the measurement of laser ablated particles. Particles were formed by UV laser ablation from a thin film of 2,5-dihydroxybenzoic acid matrix and poly(ethylene glycol) analyte.[24] The ejected particles were intercepted by a silica wafer trapping plate and the particle size was analyzed by atomic force microscopy (AFM). It was found that the relative quantity of material ejected as molecules compared to particles is strongly dependent on the laser volatilization technique. High energy densities in the sample enhanced the yield of individually desorbed molecules.

1.4.1.2. Particle Sizing

A differential mobility particle sizer has been used to detect particles below 1 μm created by UV laser irradiation of solid samples containing a MALDI matrix.[20] Two size distributions were observed: one at 10 nm and a second at $100 - 200$ nm. The former is interpreted as resulting from nucleation and condensation and, for the latter, coagulation. In our laboratory, a light scattering particle sizer was used to measure particles larger than 500 nm removed from a

MALDI matrix using a 337 nm pulsed laser.[21] Particles with a mean diameter of 680 nm were

observed at a laser fluence of 500 J/m^2. These results suggest that a significant fraction of the

material ablated under MALDI conditions is removed as large particulate. The quantity of

material removed was close to that found using other methods for the total material removed

from a sample under MALDI conditions. These studies have been extended to IR MALDI

conditions and the results indicate that larger particles are ejected from a liquid matrix with an IR

laser as compared to either a solid or liquid matrix when irradiated with a UV laser.[22]

1.4.2. Plume Imaging

Plume imaging can be used to directly examine material desorption and ablation processes

and investigate their temporal behavior. Such imaging can be done with a high-speed camera that

uses a nanosecond pulsed laser as the illumination source.[110] In the dark-field schlieren approach,

the sample is illuminated from behind by the collimated beam of the illumination laser. The

illumination beam is focused into the camera past a stop (such as a knife-edge) that blocks part

of the light. Variations in the density of the transparent medium cause variations in the intensity

of the light hitting the camera. In the light scattering approach, the sample is illuminated at right

angles with respect to the camera view. For laser-desorbed material, the schlieren approach is

sensitive to desorbed molecules and the side scattering configuration is sensitive to ablated

particles.

Rohlfing *et al.* used a CMOS camera to monitor the UV laser desorption plume of a 3-nitrobenzyl alcohol in dark-field and in scattered-light geometries.[111] A frequency-quadrupled Nd:YAG laser with 5 ns pulse width and 266 nm wavelength was employed in the desorption process. Images were taken at laser fluence slightly below and well above the ion detection threshold. Emission of the dominating gaseous fraction was found in the lower fluence regime. The amount of ejected material increased at the fluence above the threshold.

In another work by the Hillenkamp group,[27] a high-speed CMOS camera was used to image the IR laser desorption plume of a glycerol sample using schlieren and scattered light imaging. The plume imaging study corroborated the group's piezoelectric pressure sensor study in that there were two ablation regimes, the one at higher fluence corresponding to high material removal and large particle formation with a shorter pulse width OPO (6 ns pulse width) compared to a Er:YAG laser (100 ns). The difference is attributed to the OPO pulse being in the pressure confinement regime:[98] the transit time for the acoustic wave through the layer of excited material is approximately 1 ns and comparable to the OPO pulse width. The resulting build-up of tensile stress accompanied by a rapid phase change for the entire volume (phase explosion) results in the production of large particles. In a related study, Apitz and Vogel used an Er:YAG laser to irradiate water and mechanically stronger tissue samples.[28] High-speed schlieren and side scattered light images were obtained. It was found that the stress caused by explosive boiling led to the explosive ejection of material.

1.4.3. Photoacoustic Measurements

Plume ejection can be induced by a photoacoutic stress wave generated by the laser-material interaction.[28, 90] Rohlfing and co-workers utilized a fast piezoelectric detection system to record time-resolved photoacoustic signals, which reflect the thermal expansion and the rate of material ablation in IR-MALDI.[90] Two different IR lasers with pulse durations of 6 ns (tunable OPO laser) and 100 ns (Er:YAG laser) were employed. Compared to excitation with the Er:YAG laser, the dissipation of photoacoutic stress generated in glycerol by the OPO laser at 2.94 μm is significantly reduced. The time evolution of the ablation rate signals with OPO laser ablation shows an approximately Gaussian in shape with a fwhm (full width at half maximum) of 25-30 ns. In the case of excitation with the Er:YAG laser, the distribution of ablation rate signals recorded from photoacoustic signals reached the maximum after around 50 ns, followed by an exponential decay until about 1 μs. The prolonged material ejection in the 100 ns pulse width laser ablation were also confirmed by the observation of the plume dynamics by fast photography (see above).[27]

1.4.4. Ion Velocity Measurements

Investigations of the initial kinetic energy of ions and particles have been used as a direct approach to the physical mechanism of the MALDI processes.[112-113] Different experimental methods for the determination of mean initial ion velocities have been applied,[114] such as the delayed extraction method (DEM) and field-free drift method (FFDM). In the DEM,

measurement of mean initial axial velocity relies on the change in ion flight time upon variation of the delay time between laser and ion extraction pulse.[112] In the FFDM, initial velocity is deduced from the change in flight time upon variation of the field free distance between first extraction electrode and target.[113] Hillenkamp and co-workers used both DEM and FFDM to measure the mean initial velocities of analyte ions with molecular weight from 1000 Da to 150 kDa desorbed with a pulsed Er:YAG laser.[112] The initial velocities of analyte ions are affected by the matrix used. If glycerol is the matrix, the mean initial velocities of analyte ions are 850–990 and 1180-1570 m/s measured by DEM and FFDM, respectively. If succinic acid is used as the matrix, the velocities are 590-790 and 750-1100 m/s recorded by DEM and FFDM for the same analytes.[112] Based on the measurement principles, it was suggested that the initial axial ion velocities are between the limits set by the DEM and the FFDM values.

1.5. Research Objectives

The objectives of this research were to study mid-IR laser ablation in the context of laser desorption ionization mass spectrometry. Mechanisms of IR laser ablation and plume evolution were postulated and investigated to understand the fundamental physical processes of laser ablation.

The wavelength dependence of size distributions of particles ablated from glycerol was carried out using a pulsed optical parametric oscillator (OPO) laser system at atmospheric pressure. The wavelength of this laser system was tunable between 2.6 and 3.8 µm near the OH

stretch absorption as well as the CH stretch region. Through the change in wavelength, conditions of stress or thermal confinement can be selected. After irradiation of the target, the particle count and size distribution of the ablated material was recorded. The effects of the laser fluence on the ablated particle size and concentration were investigated. Also, the wavelength dependence of the energy threshold for particle formation in laser ablation processes was studied.

The effect of a UV post ablation laser on the size and concentration of IR laser generated particles was investigated. An IR laser at 2.94 μm wavelength was used to ablate particles from a thin film of the liquid MALDI matrix 3-nitrobenzyl alcohol at atmospheric pressure. A 351 nm excimer laser directed parallel to and a few millimeters above the target surface was used to irradiate the plume of desorbed material. The particle concentration, mean particle size, and particle size distributions were recorded as a function of the time delay between the IR and UV laser pulses. The mean initial velocities of the ejected particles from sample target were obtained from the time delay plots.

To study on the dynamics of plume formation and evolution during the mid-infrared laser ablation process, fast photographic images of scattered light from glycerol ablation at room temperature and atmospheric pressure were obtained. The IR OPO laser was focused onto the sample and the resulting plume was illuminated with an excimer pumped dye laser. The time delay between the IR and visible laser was varied to investigate the time behavior of material

removal. The wavelength was scanned from 2.7 to 3.5 μm and laser fluence was in the range

from 1000 to 6000 J/cm^2.

CHAPTER 2. EXPERIMENTAL

The goal of the laser ablated particle detection was to determine the quantity and size distribution of material ablated under various conditions, and compare the size and relative abundance of particles to the efficiency of laser ionization. Particles were generated by laser ablation of thin-film samples on a stainless steel target that was held at the center of an ablation chamber. A commercial light scattering particle sizer mounted under the chamber was used in this work to measure the size and number of particles in tandem with the laser ablation analysis at atmospheric pressure. A wavelength tunable IR laser was used in the experiments to investigate the particle size, concentration, and energy threshold for particle formation as a function of the wavelength.

In the experiments of IR laser ablation with UV irradiation of particles, the process of IR laser ablation of particles with UV laser post-ablation was used as a tool to investigate the ablation process. A higher UV absorption coefficient for the ablated material leads to greater particle breakup. The size distribution and quantity of post-ablated particles were measured using the same commercial light scattering particle sizer. The time scale of material ejection, the velocities of ejected particles, the size and number of particles at different delayed time are elucidated.

Plume imaging using a fast camera was introduced to my work to obtain data on the quantity, size, ejection velocity, and temporal extent of the ablated material that will be an immediate

practical aid in optimizing the design of ambient ionization. The computer controlled camera with microscope objective was illuminated by an excimer pumped dye laser with a side scattering configuration. The influence of IR laser wavelength was obtained to compare to the results of wavelength tunable laser ablation. The imaging results also give information about the velocity of the plume front that can be compared to the IR/UV two laser velocity measurements.

2.1. Laser Ablated Particle Detection
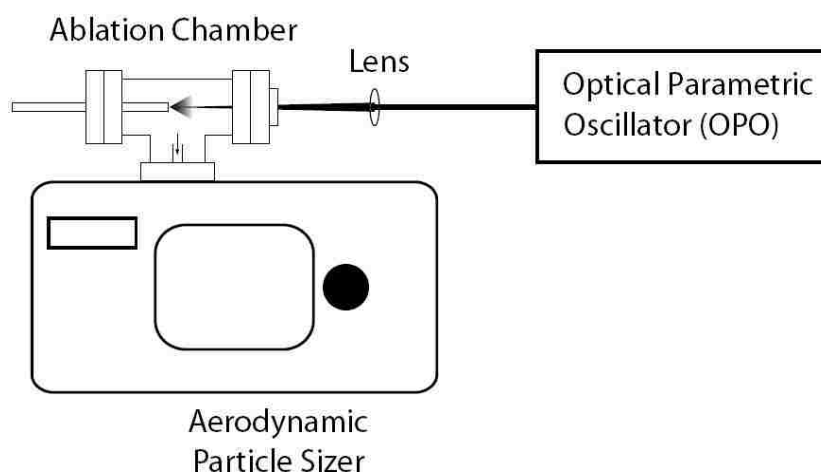
Figure 2-1 Schematic of the experimental system for laser ablation particle size measurements.

The instrument used for particle detection was a commercial aerodynamic particle sizer coupled to an ablation chamber. A diagram of the experimental system for laser ablation particle size measurements is shown in Figure 2-1. A 2 μL deposit of glycerol on a sample target resulted in a deposit 6 mm in diameter and approximately 1 mm thick. The glycerol was used directly without further purification. The stainless steel target was held at the center of the 140 cm^3 tee chamber that was constructed from a 2.75 in. conflat flange tee.

A wavelength tunable optical parametric oscillator (OPO) laser system operating at 2 Hz repetition rate was directed at the target at normal incidence through a sapphire window on the ablation chamber. A 254 mm focal length CaF_2 lens was used to focus the laser to an elliptical spot on the target. The spot size of focused laser beam varied from 290 μm × 390 μm at 3.8 μm to 350 μm × 460 μm at 2.6 μm, which was measured by irradiating a small piece of laser burn paper attached to a target and inspecting the burn mark visually with a measuring microscope. The OPO laser was attenuated by inserting a combination of uncoated calcium fluoride, zinc selenide, zinc sulfide, silicon, and germanium optical flats into the beam. The energy was measured using the pyroelectric detector (ED-104AX, Gentec, Palo Alto, CA) and read out using a digital oscilloscope (Model 9350M, Lecroy, Chestnut Ridge, NY).

Particles were formed by laser ablation from the target into the chamber that was flushed using filtered compressed air to transport the ablated particles to the detection system at a flow rate of 5 L/min. Ejected particles were directed into the inlet of the aerodynamic particle sizer, which was mounted directly under the chamber. The concentration and the size distribution of particles ablated from the sample target by the IR laser at different wavelengths were recorded by the particle sizer.

2.1.1. Aerodynamic Particle Sizer

The size distribution and concentration of the ablated aerosol particles were analyzed by the aerodynamic particle sizer (Model 3321, TSI, Shoreview, MN). The particle sizer measured the

velocity of particles in an accelerating air-flow through a nozzle (Figure 2-2). The aerodynamic

size of a particle determines its acceleration rate because inertia increases with particle size.

After entering the instrument, particles were confined to the center line of the accelerating flow

by sheath air, after which they passed through two focused beams from a 655 nm diode laser.

Side-scattered light is collected using an elliptical mirror that focuses the light onto a solid-state

photodetector. Each particle produces a two-peaked signal. The time spacing between the two

peaks is used to determine the velocity of each particle and the particle aerodynamic diameter is

obtained in real-time from the velocity. The amplitude of the signal is recorded for

light-scattering intensity.
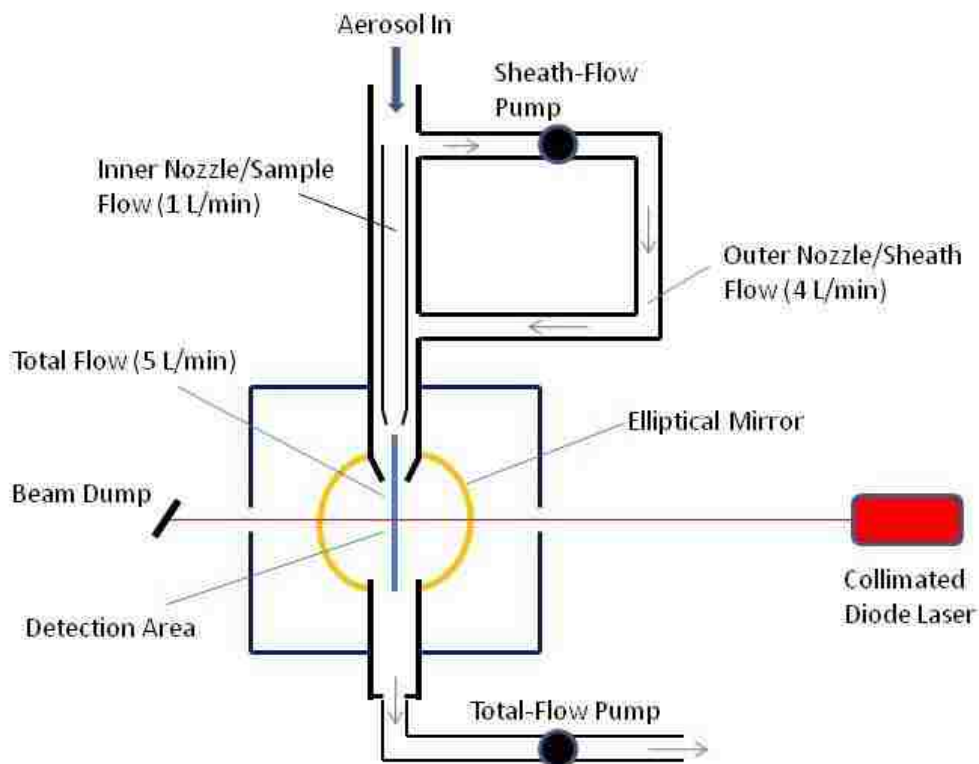
Figure 2-2 Aerodynamic particle sizer.
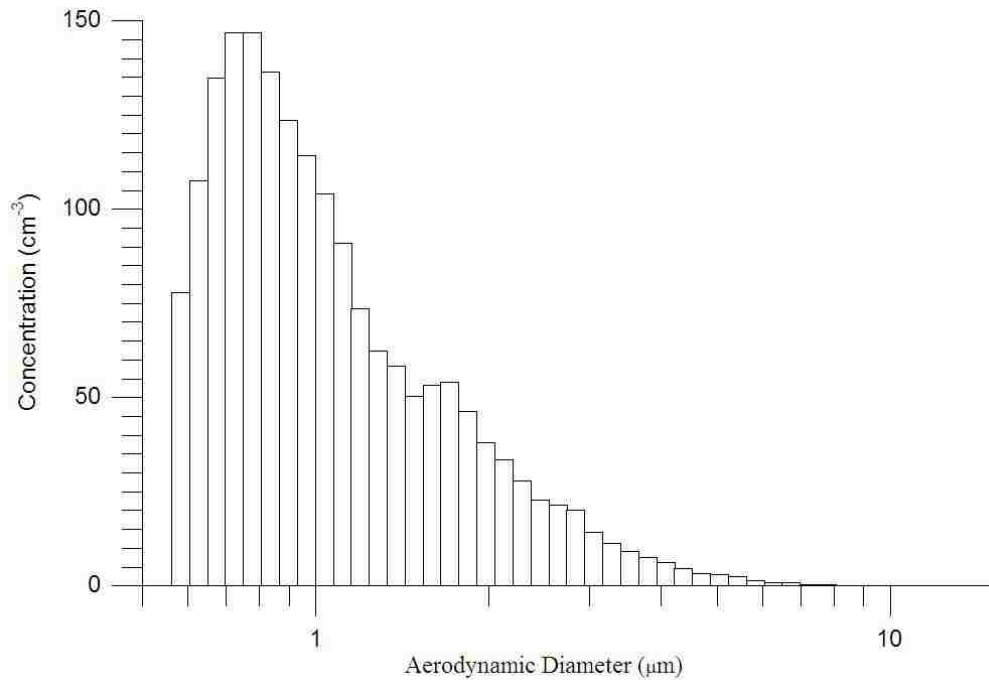
Figure 2-3 Particle size distribution plot of glycerol particles ablated by a 3.0 μm pulsed laser.

The measurement range of the particle sizer is from 300 nm to 20 μm. Particles between 500 nm and 20 μm in aerodynamic diameter can be measured to a precision of ±30 nm. Particles between 500 and 300 nm are recorded in a separate channel due to the larger uncertainty in the size measurement in this range (limited by the wavelength of diode laser beams). Particle concentrations up to 10,000 /cm^3 can be monitored. Shown in Figure 2-3 is a particle size distribution plot measured from glycerol ablated by the OPO at 8.0 kJ/m^2 fluence. The height of each vertical bar indicates the concentration of ejected particles measured in the indicated aerodynamic diameter range.

2.1.2. OPO Laser

An optical parametric oscillator (OPO) consists of a nonlinear optical crystal and an

optical resonator. Shown in Figure 2-4 is the optical layout of an optical parametric oscillator. By means of nonlinear optical interaction, the non-linear crystal converts the input pump beam (wavelength λ_p) into two output longer wavelength beams called the signal (λ_s) and idler (λ_i; $\lambda_s \leq \lambda_i$) waves. The sum of the output frequencies is equal to the input frequency: $\omega_s + \omega_i = \omega_p$. The wavelengths of the signal and idler are tunable by changing the angle of the pump beam with respect to the crystal axis. The function of optical resonator is to achieve resonance with at least one of the signal and idler wavelengths, leading to a amplitude gain (parametric amplification) at each round-trip.[115]
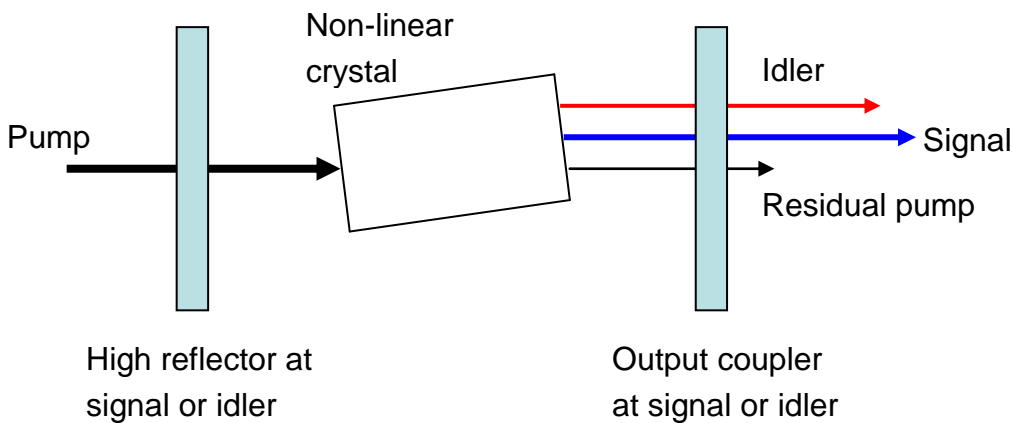
Figure 2-4 Optical layout of an optical parametric oscillator.

Since the signal and idler wavelengths can be varied in a wide range, it is possible to access wavelengths from the mid-infrared to the far-infrared that are difficult to obtain with other laser systems An OPO must be pumped by another laser. At low pump energies there is insufficient

gain for oscillation. Only when the pump power reaches a particular threshold level, oscillation

occurs.[115]
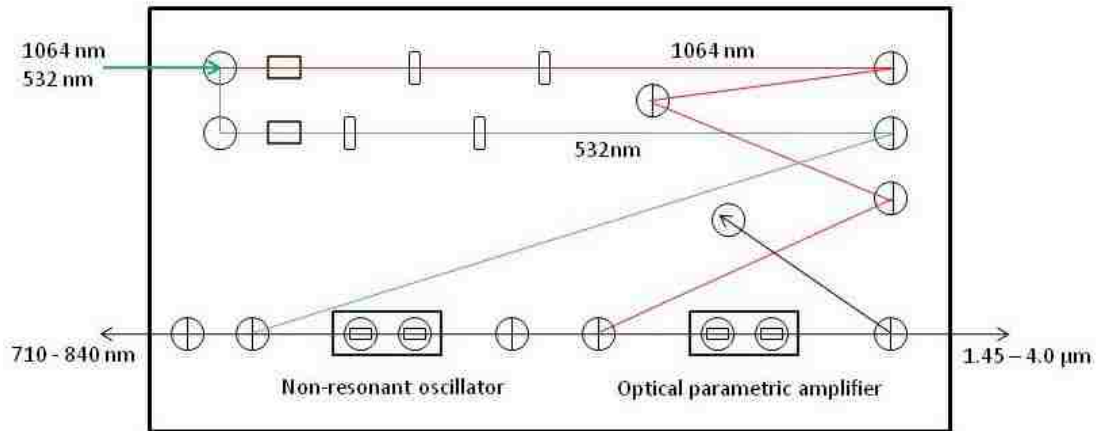
Figure 2-5 Schematic of the OPO laser system.

In this work, a wavelength tunable OPO (Mirage 3000B, Continuum, Santa Clara, CA), pumped by 1064 nm fundamental and 532 nm second harmonic of a Nd:YAG laser (Powerlite 8000, Continuum, Santa Clara, CA), was used for sample ablation. The OPO produces a 5 ns laser pulse and is tunable from 1.45 to 4.0 μm with mJ pulse energies throughout this range. The tunable radiation was generated by a two-stage device consisting of a non-resonant oscillator (NRO) and an optical parametric amplifier (OPA) with the layout shown in Figure 2-5. Both the NRO and OPA consisted of two potassium titanyl phosphate (KTP) crystals. The NRO is pumped by the 532 nm doubled Nd:YAG output. The signal and idler frequencies are determined by the phase-matching conditions within the KTP crystal. Wavelength tuning in the Mirage 3000B can be accomplished by changing the angle of the

crystal.[116] The NRO idler beam with wavelengths ranging from 1.45 to 2.12 μm (depending on the crystal orientation) is directed into the OPA stage, which also has a pair of KTP crystals pumped by the 1064 nm Nd:YAG output, is a single pass amplifier that operates on the same general principle as the OPO. The OPA signal output (the amplified OPO idler) is tunable from 1.45 to 2.12 μm and the idler output is tunable from 2.12 to 4.00 μm. Both the signal and idler beams exit the OPO as outputs.

2.2. IR Laser Ablation with UV Irradiation of Particles

In some of the experiments using IR laser ablation, a UV laser was used to irradiate the expanding plume and create ions post-ablation). The two laser systems used in this configuration were the OPO laser described above combined with an excimer laser. The excimer laser beam was directed parallel to the OPO beam, requiring additional ports on the ablation chamber. To accomplish this, the tee chamber used in the single laser ablation experiments was replied with a six-way cross chamber that had a volume of 240 cm^3 (Figure 2-6).
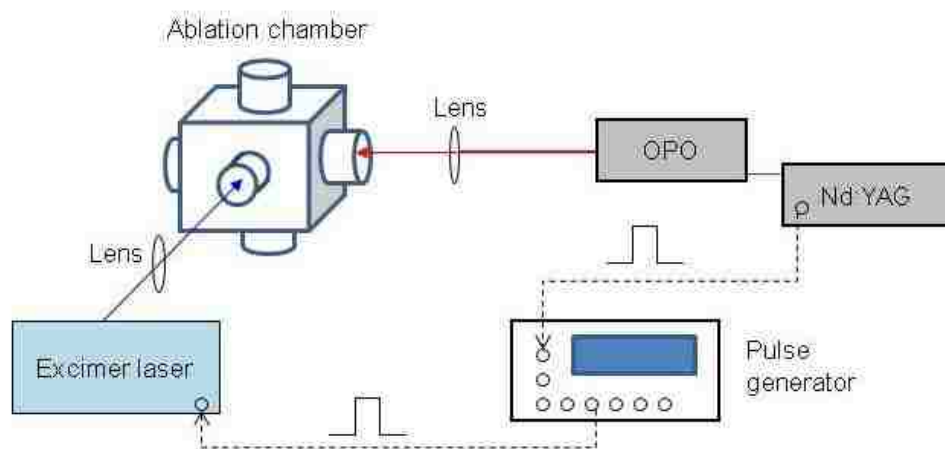
Figure 2-6 Schematic layout of the IR laser ablation with UV irradiation of particles.

A 1 mm thick deposit of 3-nitrobenzyl alcohol was prepared by dropping a 3.0 μL neat NBA

onto a stainless steel sample target, which was placed at the center of the ablation chamber. The

target was irradiated by the OPO laser at normal incidence; a sapphire window was used on the

chamber as above. The UV laser beam was directed perpendicular to the OPO beam and parallel

to the sample target, passing through a quartz window on the chamber. The schematic diagram of

UV laser particle ablation is shown in Figure 2-7. The wavelength of the OPO was fixed at 2.94

μm and the excimer was operated using a xenon fluoride gas mix for operation at wavelength of

351 nm. Both lasers were attenuated by inserting optical flats into the beams. The IR beam was

directed through a 254 mm focal length CaF_2 lens that produced a 250 μm × 300 μm spot on the

target as determined by laser burn paper. The UV laser was focused to a spot size of 1.4 mm ×

0.6 mm directly above the target using a 254 mm focal length cylindrical lens. The distance

between the center of UV beam and the target was 3.5 mm and was adjusted using a single axis

stage (x-stage, LMT-151, MDC, Hayward, CA).
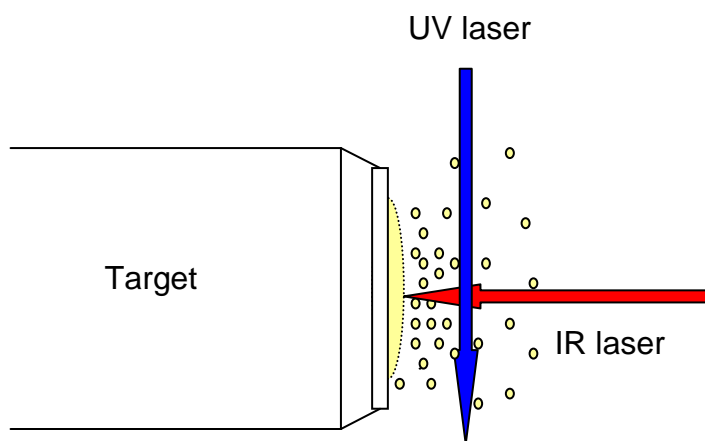
Figure 2-7 Schematic diagram of UV excimer laser particle ablation.

A digital delay generator (Model DG535, Stanford Research System, Sunnyvale, CA) was triggered by the Q-switch synchronization output of the OPO pump laser at a repetition rate of 2 Hz. After a selected delay, the pulser externally triggered the excimer laser at the same repletion rate. The time delay between the lasers is indicated by Δt, where $\Delta t = t_{UV} - t_{IR}$. The time delay was calibrated using the digital oscilloscope to measure the time difference between trigger signals. The timing connection diagram for the two laser systems is shown in Figure 2-6. The aerodynamic particle sizer used in Section 2.1 was mounted under the six-way cross chamber as above and was suffused with filtered compressed air at a flow rate of 5 L/min. The concentration and size distribution of the ejected particles were measured as a function of delay time, Δt.

2.2.1. Excimer Laser
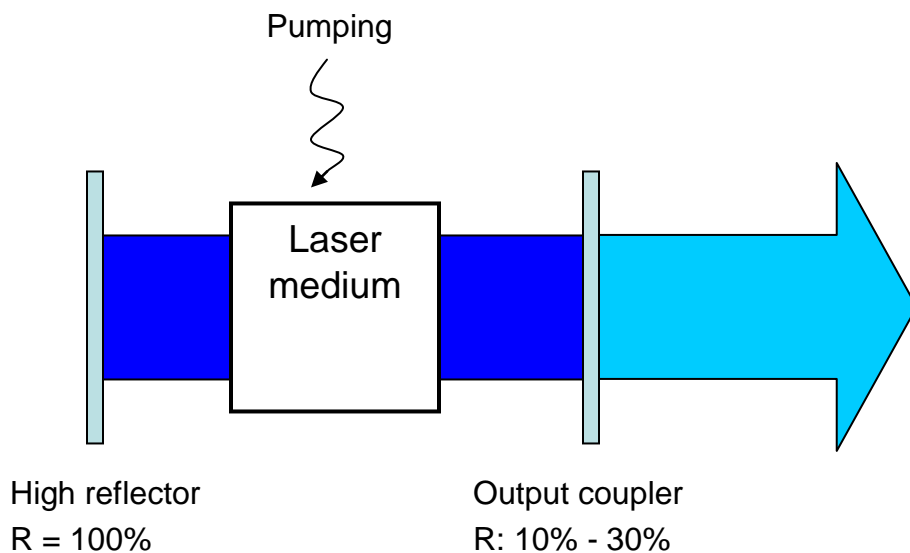
Figure 2-8 Optical layout of an excimer laser cavity.

The term excimer is a short for "excited dimer", which is a short-lived diatomic molecule formed between two atoms or molecules that would not bond if both were in the ground state.[117] After a short time, the excimer emits a photon and returns to the ground state and dissociates back into two unbound atoms. Most excimer lasers use a combination of noble gas (argon, krypton, or xenon) and a halogen gas (chlorine or fluorine) as the laser gain medium. The wavelength of an excimer laser depends on the operating gas, and is usually in the ultraviolet range.[118]

A simple schematic layout of an excimer laser cavity is shown in Figure 2-8. In order to generate laser light, an optical resonator is provided by two mirrors mounted on opposite sides of the laser medium to force the radiation to oscillate within the laser cavity. The back mirror is totally reflective ($R = 100\%$), while the front one lets a part of the light escape from the cavity, thereby forming the laser beam. The laser medium is excited (pumped) by an electrical discharge.[118]

A UV excimer laser (Optex, Lambda Physik AG, Gőttingen, Germany) was used in the experiments. The excimer laser can be operated at the following wavelengths: 193 nm (argon fluoride), 248 nm (krypton fluoride), 308 nm (xenon chlorine), and 351 nm (xenon fluoride) with a repetition rate up to 200 Hz. The maximum laser pulse energy at 193, 248, and 351 nm are 2.5, 13, 22, 10, and 8 mJ, respectively. The pulse temporal at all wavelengths is 8 ns. The pulse energies were measured using the pyroelectric detector.

2.3. Fast Photography

A diagram of the fast photography setup is shown in Figure 2-9. The wavelength tunable

OPO laser was used for plume generation. The digital delay generator was triggered by the

Q-switch synchronization output of the Nd:YAG laser. After a selected delay, the delay

generator triggered the excimer laser and a COMS digital camera. The trigger setup and timing

diagram in fast photography are shown in Appendix A. The excimer laser was operated using a

krypton fluoride (KrF) gas mix for operation at the wavelength of 248 nm. A calcium fluoride

cylindrical lens (33 cm focal length) focused the pulsed UV beam to a horizontal line on a dye

cuvette in a home-built dye laser.
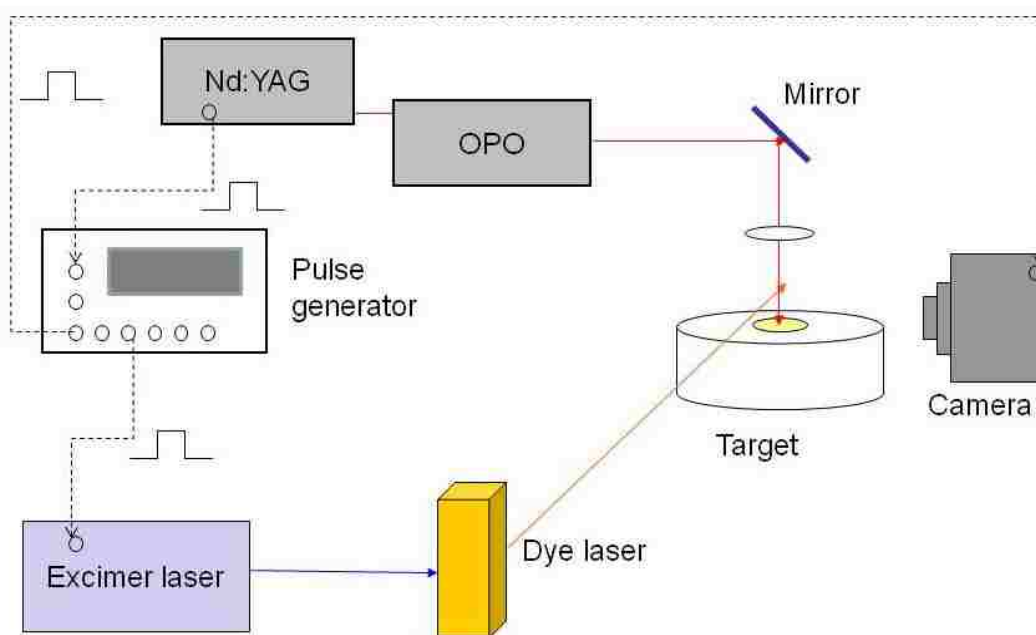
Figure 2-9 Schematic layout of the fast photography experiments.

An approximately 1 mm thick and 6 mm in diameter deposit of liquid sample was prepared by

dropping 3.0 μL of neat glycerol onto a stainless steel sample target, which was mounted on an xyz

stage. The pulsed IR beam was directed through a 254 mm focal length (at 3 μm) CaF$_2$ lens that irradiated the target at normal incidence. The IR laser was attenuated by inserting optical flats into the beam. The dye laser was oriented perpendicular to the ablation laser and parallel to the sample surface to obtain the desired time resolution on the nanosecond and microsecond levels.

At different time delays after the of the IR OPO pulse, the scattered light from the glycerol plume was recorded by the digital camera. The exposure time was defined by the 8 ns illumination laser pulse within the 100 μs shutter time of the camera. Images were transferred from the camera through an IEEE 1394 (Firewire) connection to a microcomputer using in-house written LabView (National Instruments, Austin, Texas) routines. After saving an image, the delay time was adjusted automatically by this program, which saved photos of the plume sequentially. The LabView program is described in detail in Appendix B.

2.3.1. Dye Laser

In contrast to the solid state Nd:YAG and excimer gas laser, a dye laser uses a liquid, in this case an organic dye solution, as the lasing medium. Commonly used laser dyes are rhodamine, fluorescein, coumarin, stilbene, umbelliferone, and tetracene,.[119] These dyes can be used for a wide range of emission wavelengths from the ultraviolet to the near-infrared region, which makes them particularly suitable for tunable lasers.

A fast discharge flashlamp or a high energy pulsed laser is required to pump the dye solution in a dye laser cuvette.[115] For example, after focusing a UV laser beam to a thin line on the

surface of a dye laser cell using a cylindrical lens, the dye was excited along the line on the

inside surface of the cell and form another light beam along the line to both ends of the dye cell.

An optical cavity is also needed to amplify the light produced by the dye's fluorescence. A prism

or diffraction grating can be placed in the beam path select the wavelength. However, in this case

a broad illumination wavelength was acceptable and no wavelength selection elements were

placed in the optical cavity. A schematic layout of dye laser construction is shown in Figure

2-10.
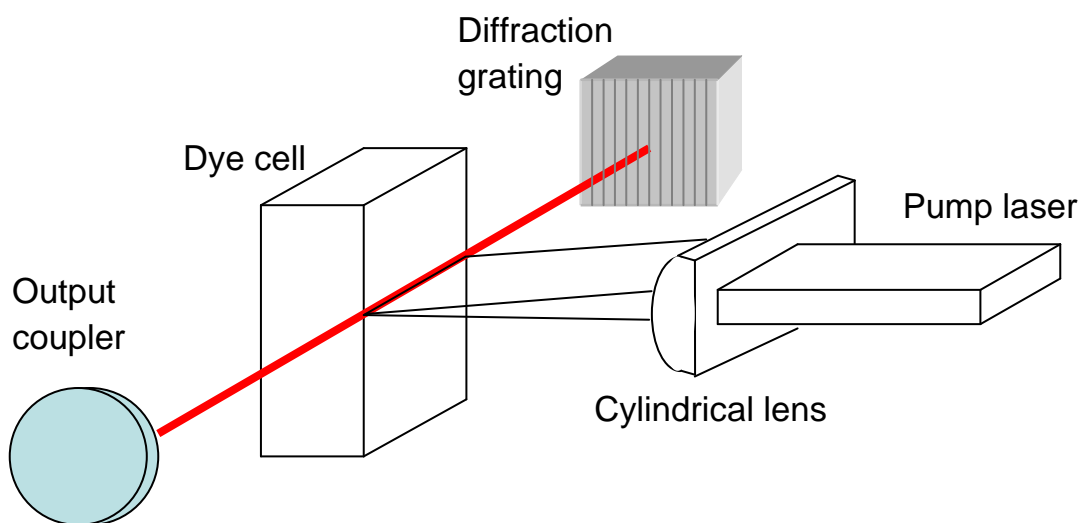
Figure 2-10 Schematic layout of dye laser cavity.

In this work, the dye laser was used for the fast photography experiments, working as the

illumination light. Rhodamine 6G was dissolved in methanol to form a 10^{-3} M dye solution. A

quartz fluorimeter cuvette (with four polished windows) of 10 mm × 10 mm dimensions

contained the dye solution. A calcium fluoride cylindrical lens (33 cm focal length) focused the

pulsed excimer UV beam with wavelength of 248 nm to a horizontal line on the dye cuvette,

which side pumped the dye along the line on the inside surface of the cuvette. The pulsed dye laser cavity (10 cm length) consisted of a flat aluminum coated reflector (>93%, Newport, Irvine, CA) and an output coupler (70% R, Melles Griot, Albuquerque, NM).

2.3.2. Digital Camera

A 1.3 megapixel monochrome digital camera (Pixelink PL-B771F, Vitana Co., Ontario, Canada) was used to monitor the plume dynamic evolution. The camera sensor is based on a CMOS rolling shutter progressive scan sensor. The minimum shutter speed of the camera is 100 μs. The camera can deliver 30 fps (frames per second) at SXGA (1280 × 1024) resolution, 48 fps at XGA (1024 × 768) resolution and 109 fps at VGA (640 × 480) resolution. The images obtained for this work were obtained at a resolution of 1280 × 1024. After receiving a TTL signal from the pulse generator, the shutter was open for photo or video recording and recorded files are saved by a computer connected to the camera through the Firewire interface.

2.4. Reagents and Standards

Liquid material glycerol (99%, Sigma, St. Louis, MO) was used in Chapter 3 and 5 as the testing samples. In Chapter 4, another liquid sample, 3-nitrobenzyl alcohol (NBA, 98%, Aldrich, Milwaukee, WI), was investigated. NBA absorbs both IR and UV lights and only IR light is absorbed by glycerol.

The gas mixtures used for excimer laser were obtained from Spectra Gases Inc, Alpha NJ. The component of gas mix used in Chapter 4 was fluorine 0.166% xenon 0.454% with neon

balance. The component of gas mix used in Chapter 5 was fluorine 0.106% krypton 1.515% with

neon balance.

The 10^{-3} M dye solution used in Chapter 5 was made by dissolving rhodamine 6G (99%,

Sigma-Aldrich, St. Louis, MO) into methyl alcohol (99.9%, Mallinckrodt Baker, Phillipsburg,

NJ).

CHAPTER 3. WAVELENGTH DEPENDENCE OF LASER ABLATION IN THE MID INFRARED*

3.1. Introduction

This chapter describes a study of the size distributions of coarse particles ablated from glycerol at atmospheric pressure using of a wavelength tunable optical parametric oscillator (OPO) laser system. A thin film of glycerol on a metal surface was irradiated with a pulsed IR laser at wavelengths between 2.6 and 3.8 μm, covering the absorption band of the OH and CH stretch vibrations. After irradiation of the target, the particle count and size distribution of ablated material was recorded. The laser fluence ranged from 1000 to 6000 J/m^2. The results suggest that, through the change in wavelength, conditions of stress or thermal confinement can be selected.

3.2. Experimental

Particles were generated from glycerol that was irradiated at atmospheric pressure using the mid-infrared OPO (described in Chapter 2, Section 2.1) at a repetition of 2 Hz. The OPO was set to wavelengths between 2.6 and 3.8 μm for these experiments. Samples were prepared by depositing 3 μL of neat glycerol onto the sample target, which was held at the center of the ablation chamber. The size distribution and quantity of ejected particles with diameters larger than 300 nm were measured using the aerodynamic particle sizer (described in Chapter 2, Section 2.1). The particle size measurement was initiated 10 s after the laser began irradiating the

---

*Reprinted by permission of the Elsevier.

sample to assure that a steady supply of particles was being created. Signals were integrated for a total of 20 s, which corresponds to 40 laser shots.

3.3. Results

Figure 3-1 shows the size distribution of particles ablated from glycerol at wavelengths between 2.8 and 3.6 μm in increments of 0.1 μm. The laser fluence was 8000 J/m^2 at a 2 Hz repetition rate. The particle size distribution did not change significantly as a function of laser repetition rate between 0.5 and 10 Hz. The y-axis in each plot extends from zero concentration to 150/cm^3. The plots with a multiplicative factor indicate an expansion of scale. For example, the scale in Figure 3-1a (2.8 μm wavelength) is expanded by a factor of 2 (from 75/cm^3 to 150/cm^3 full scale) due to the lower concentration of particles observed at this wavelength. The height of each vertical bar indicates the concentration of ejected particles measured in the indicated aerodynamic diameter range; the total particle concentration at each wavelength is given in Table 3-1 and has a maximum of 3000/cm^3 at 3.0 μm (Figure 3-1d). Throughout the wavelength range, the peak particle size is nearly constant between 0.65 and 0.83 μm and the mean particle diameter varies between 0.87 and 1.6 μm. The list of the average, peak and the mean particle size are given in Table 3-1.

Figure 3-1 Particle size distribution measured for irradiation of glycerol at 8.0 kJ/m^2 fluence at different wavelengths: (a) 2.80 μm; (b) 2.90μm; (c) 2.94 μm; (d) 3.00 μm; (e) 3.10 μm; (f) 3.20 μm; (g) 3.30 μm; (h) 3.40 μm; (i) 3.50 μm; (j) 3.60 μm.

Table 3-1 Average and peak size of particles ablated from glycerol near the fluence of 8000 J/m^2 at atmospheric pressure and threshold for particle ablation.

Wavelength (µm)	Particle Concentration (/cm^3)	Mean Particle Size (µm)	Peak Particle Size (µm)	Mass-weighted Concentration (mg/m^3)	Mean Mass-weighted Particle Size (µm)	Peak Mass-weighted Particle Size (µm)	Threshold Fluence (J/m^2)
2.80	825	1.14	0.729	1.00	5.69	6.44	3550
2.90	2006	0.867	0.672	1.05	1.86	1.41	2050
2.94	2521	0.927	0.723	2.14	2.39	1.90	1300
3.00	3070	1.17	0.810	4.77	3.54	3.56	1270
3.10	2358	1.25	0.809	6.86	4.65	5.54	1400
3.20	1812	1.32	0.805	6.28	4.98	5.73	1850
3.30	374	1.58	0.787	2.72	6.08	6.23	2150
3.40	1725	1.06	0.701	3.32	4.88	5.64	1750
3.50	2068	1.06	0.673	3.91	4.93	5.39	1350
3.60	1228	1.32	0.757	2.96	5.37	6.33	1800

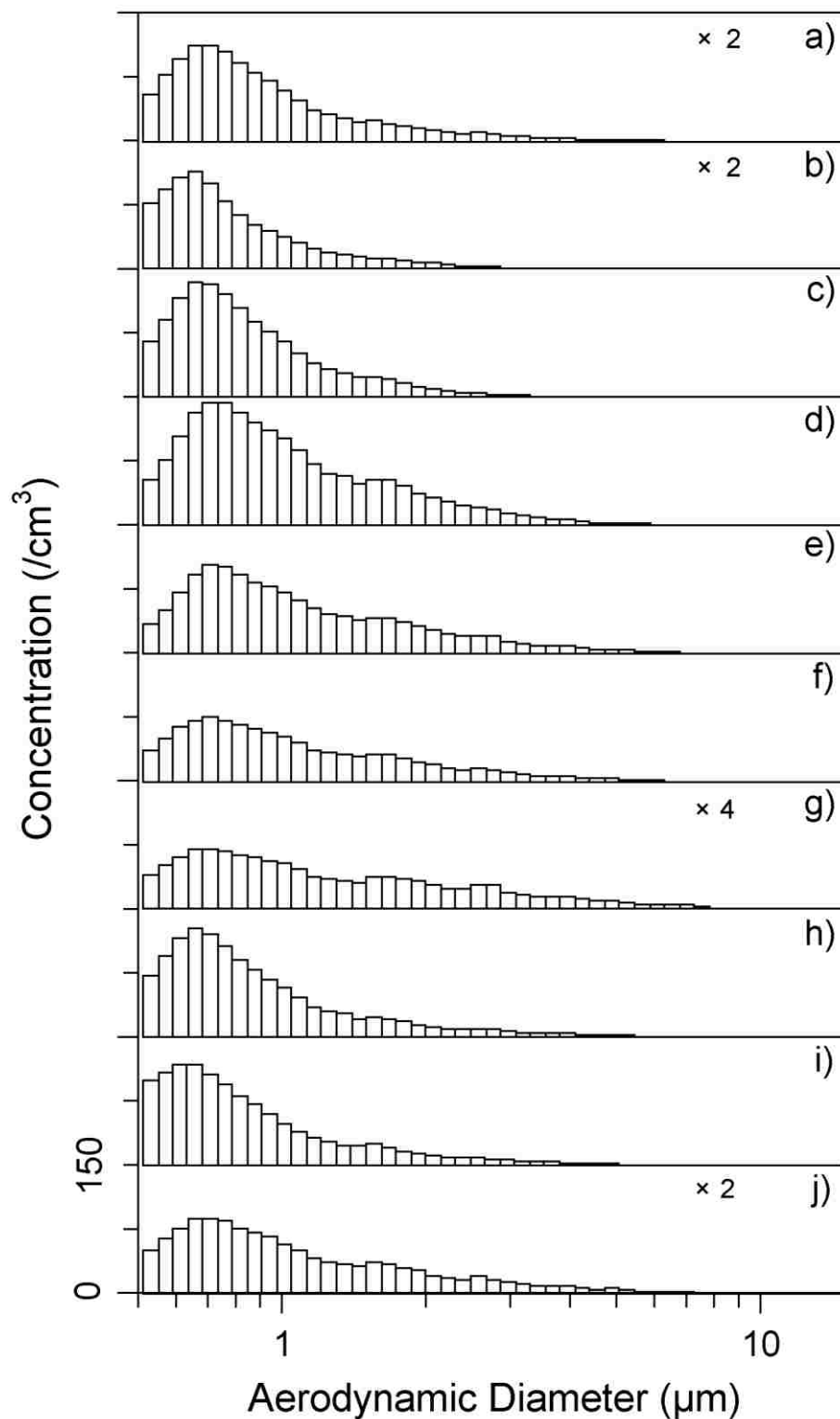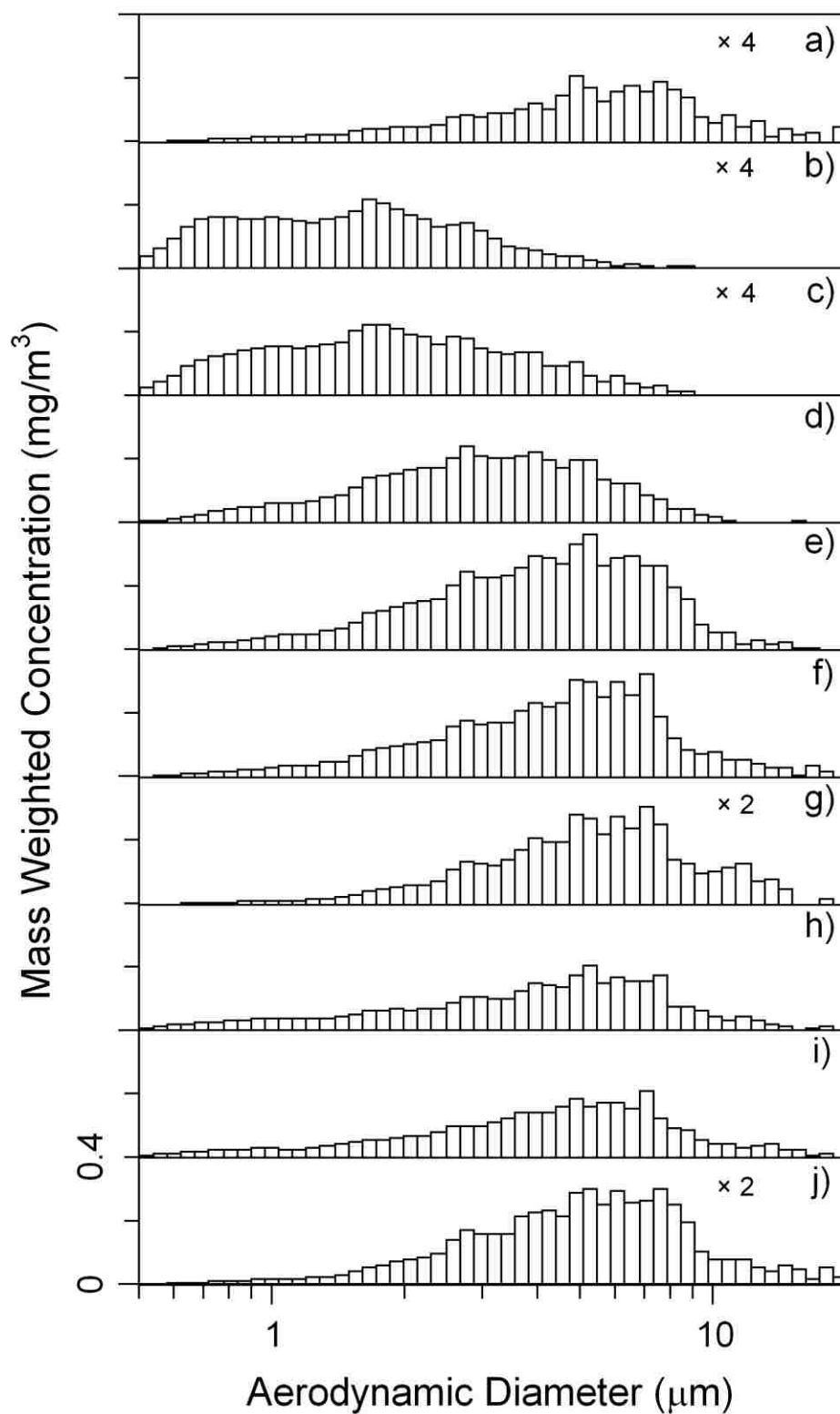**Figure 3-2** Mass-weighted particle size distribution measured for irradiation of glycerol at 8.0 kJ/m^2 fluence at different wavelengths: (a) 2.80 μm; (b) 2.90 μm; (c) 2.94 μm; (d) 3.00 μm; (e) 3.10 μm; (f) 3.20 μm; (g) 3.30 μm; (h) 3.40 μm; (i) 3.50 μm; (j) 3.60 μm.

Shown in Figure 3-2 is the mass-weighted particle concentration as a function of particle size for the glycerol ablation at wavelengths between 2.8 and 3.6 μm. The experimental conditions are identical to that depicted in Figure 3-1, but have been weighted for particle mass. The y-axis of the plots is 0.4 mg/m^3 full scale except where indicated by the multiplication factor. The peak centroid of the mass-weighted particle size distribution varies between 2 and 8 μm, with the smallest values near 2.9 μm wavelength (Figure 3-2 b and c) and a maximum at 3.3 μm (Figure 3-2g). Average values for the peak and mean mass-weighted particle size and concentration are shown in Table 3-1. The maximum particle mass ejected is 7 mg/m^3 at 3.1 μm (Figure 3-2e) and the lowest is at 3.3 μm and below 2.9 μm (Figure 3-2 g, a and b).

As can be seen in Figures 3-1 and 3-2, and in Table 3-1, the physical characteristics of the ablated particles change with the wavelength of the incident IR laser. It is instructive to compare these wavelength variations in the particle concentration and diameter with the IR absorption of glycerol. Figure 3-3a shows the FTIR-ATR spectrum of a glycerol thin film between 2.7 and 3.7 μm wavelength, which has similar absorption features to the IR absorption spectrum of bulk glycerol.[22] An intense and broad peak at 3.0 μm corresponds to OH stretch vibration and two less intense peaks at 3.4 and 3.5 μm correspond to CH stretch vibrational modes. The wavelength dependence of particle concentration and mass-weighted particle concentration in the IR laser ablation process are shown in Figure 3-3b and 3-3c, respectively. The measurements were

performed at a laser fluence of 8000 J/m^2, and the wavelength ranged from 2.7 to 3.7 μm. There

are two broad features near 3.0 and 3.5 μm in Figure 3-3b and 3-3c that coincide with the OH

and CH stretch vibration depicted in Figure 3-3a. There is also a minimum at 3.3 μm in both

Figure 3-3b and 3-3c that corresponds to the minimum in Figure 3-3a.
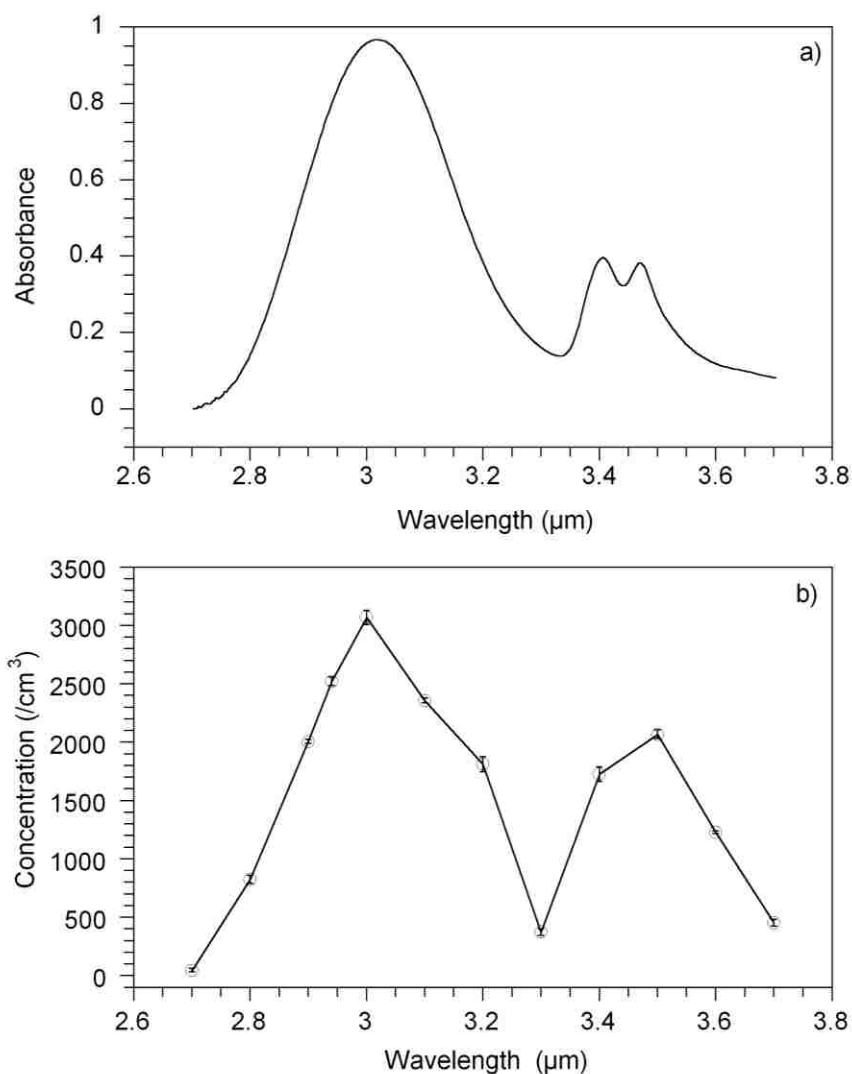
Figure 3-3 Comparison of (a) FTIR-ATR spectrum of a thin film of glycerol, (b) concentration of ablated particles at wavelengths from 2.70 to 3.70 μm at a fluence of 8.0 kJ/m^2 and (c) concentration of mass-weighted particles at wavelengths from 2.70 to 3.70 μm at a fluence of 8.0 kJ/m^2.

The equivalent plots for the wavelength dependence of the mean particle size and mean mass-weighted particle size are shown in Figures 3-4a and 3-4b. The laser fluence is 8000 J/m^2 and the wavelength is from 2.7 to 3.7 μm. In both figures, there are local minima in the particle diameter near 2.9 and 3.5 μm, nearly coincident with the OH and CH stretch absorption. The maximum particle diameter occurs near 3.3 μm, coincident with the local minimum in IR absorption between the OH and CH absorption bands.

The fluence dependence of particle concentration was measured at all wavelengths. Figure 3-5 shows measurements obtained at different wavelengths. In Figure 3-5c, below a fluence of 4000 J/m^2, the particle concentration increases slowly then increases sharply up to 14 kJ/m^2 where it levels off. This sigmoidal curve is observed at all other wavelengths between 2.6 and 3.8 μm. A plot of the threshold fluence as a function of wavelength is shown in Figure 3-6 and indicated in Table 3-1. The value of the threshold fluence was obtained by finding the point on a

plot of the logarithm of the fluence as a function of the laser energy at which the particle

concentration exceeded the background concentration. At 3.2 μm, the fluence threshold is 1850

J/m^2 and is similar to the value reported earlier for mid-IR ablation of glycerol.[22] The threshold

fluence is lowest at 3.0 and 3.5 μm, corresponding to the OH and CH stretch absorption.
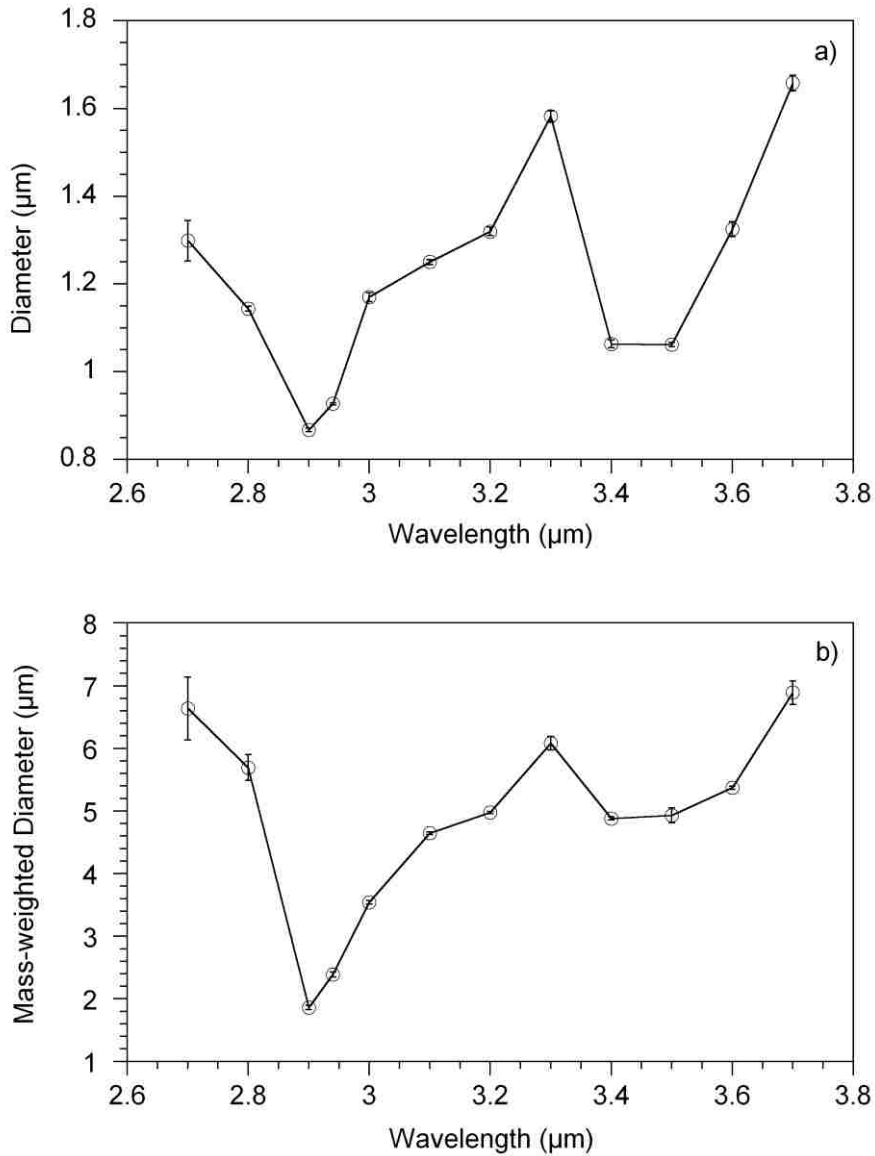
Figure 3-4 Wavelength dependence of the (a) mean particle size and (b) mean mass-weighted particle size for IR ablation of glycerol at a fluence of 8.0 kJ/m^2.
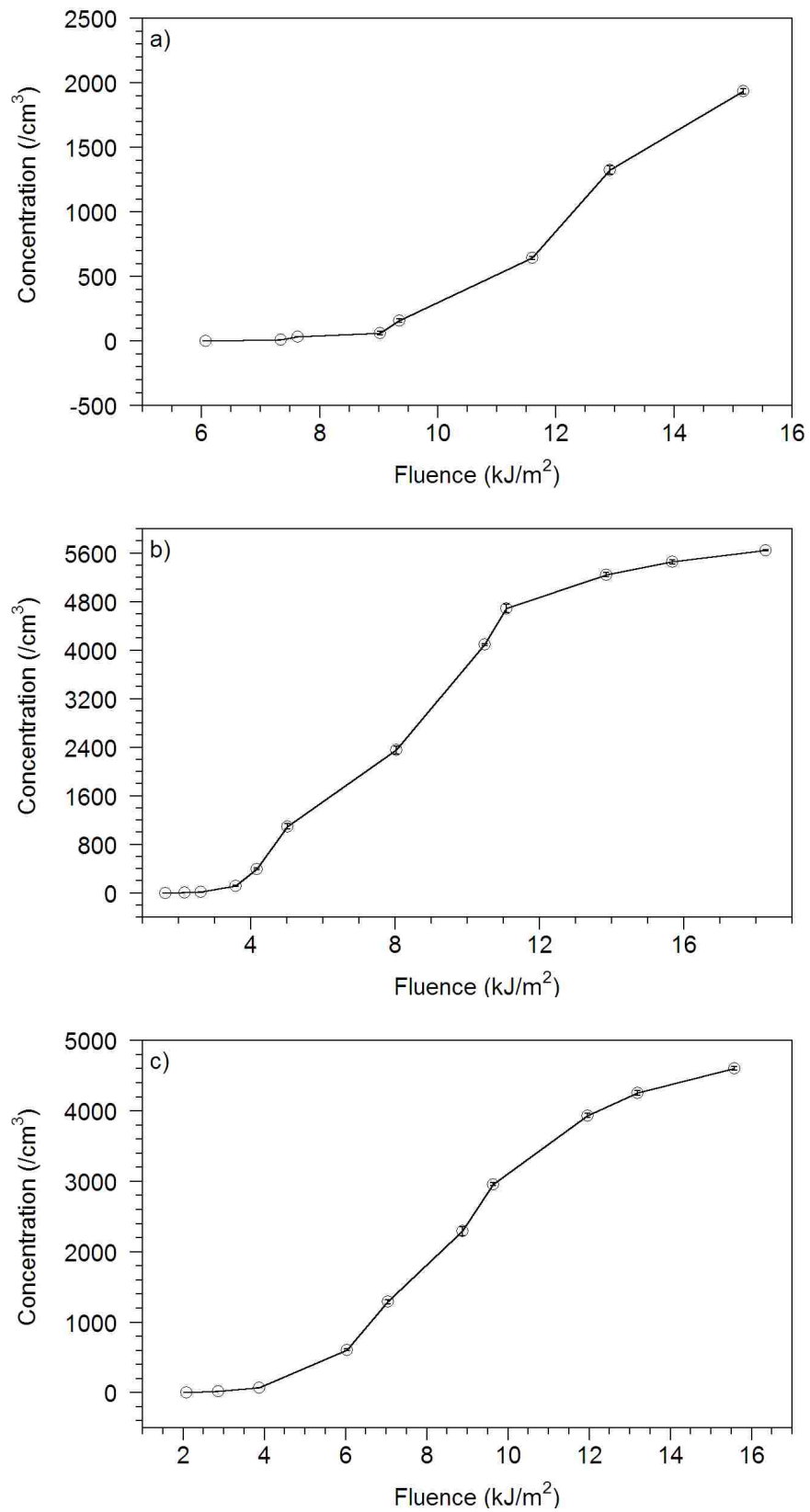
Figure 3-5 IR laser fluence dependence of the coarse particle concentration for ablation of glycerol at a) 2.7, b) 3.0, c) 3.2, and d) 3.5 μm.
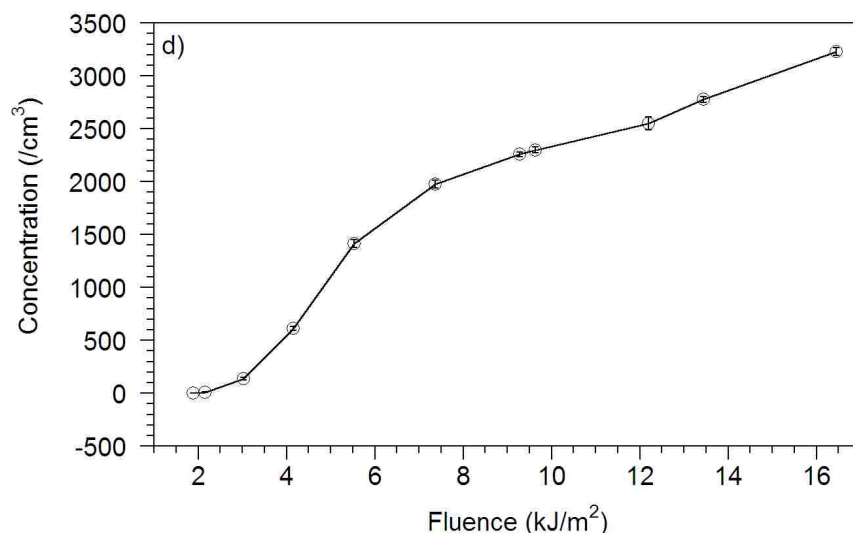
Figure 3-7 contains a three-dimensional graph of the glycerol particle concentration plotted as a function of laser fluence and wavelength. The OH and CH stretch absorption wavelength regions, at 3 µm and 3.5 µm respectively, stand out both for the relatively higher concentrations at a given fluence as well as the lower fluence required for particle formation.
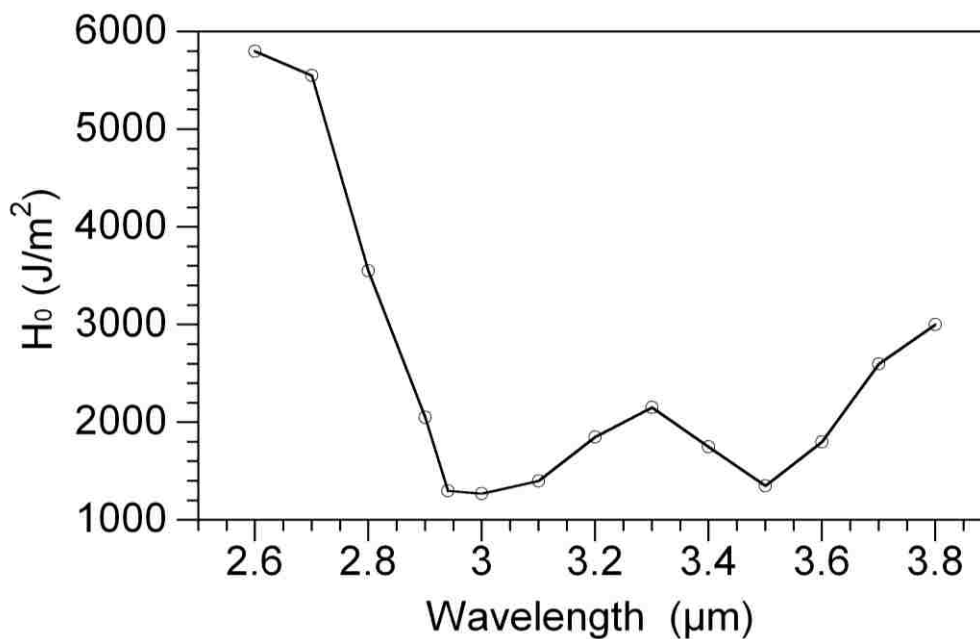
Figure 3-6 IR ablation threshold of particle for glycerol at wavelengths from 2.6 to 3.8 µm.
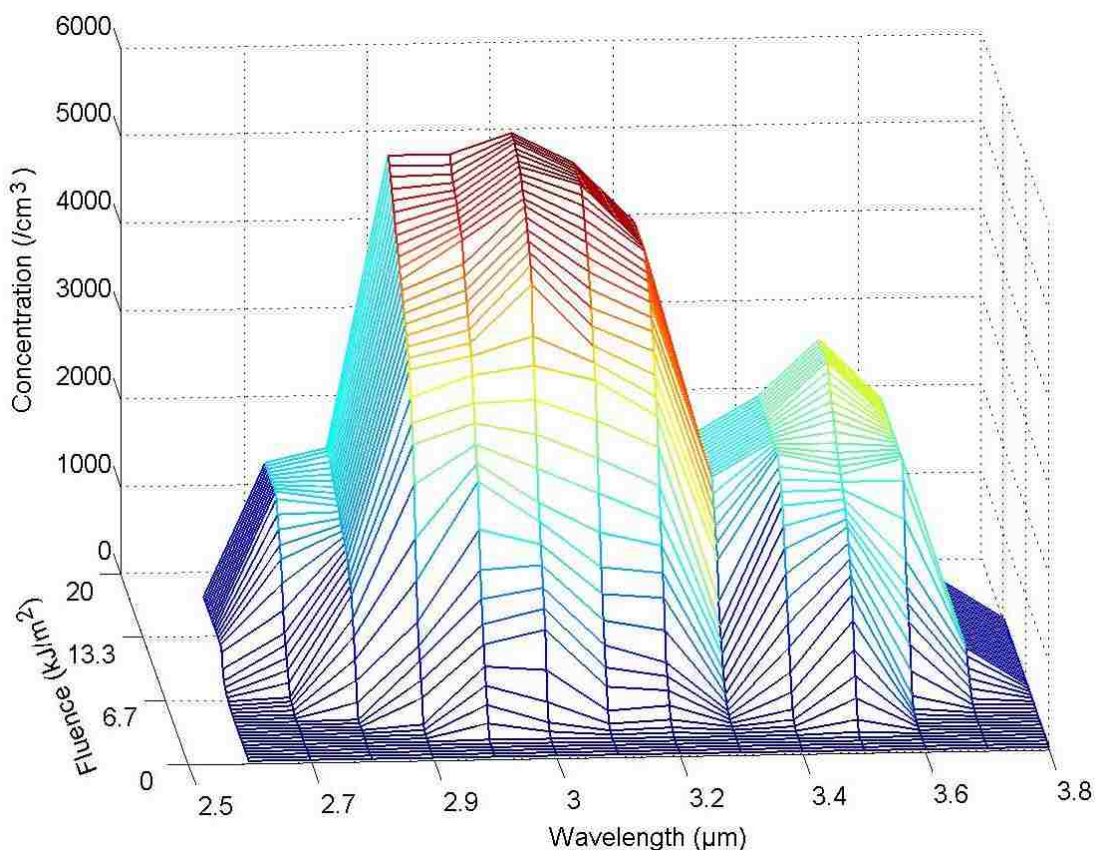
Figure 3-7 Surface plot of the fluence dependence of particle concentration for ablation of glycerol at wavelengths from 2.60 to 3.80 μm.

3.4. Discussion

As discussed in Chapter 1, Section 1.3.1, there are two general regimes for laser removal of material under MALDI conditions that depend on the rate of energy deposition in the material. If the laser energy is deposited more rapidly than it can be removed through thermal diffusion from the irradiated volume, a regime known as thermal confinement occurs. Explosive boiling can occur in thermal confinement regime if the volume is heated above its phase transition temperature and this can result in the rapid ejection of molecules and liquid droplets. If the laser energy is deposited at a more rapid rate, a condition known as stress confinement is obtained, in

69

which the rate of energy flow into the sample exceeds the rate of energy loss through the collective molecular motion of acoustic waves. Explosive boiling can also occur under stress confinement conditions and, in this regime, the particles formed are larger and more numerous.[89, 97-99] If sufficient stress is generated, spallation of material can occur in the stress confinement regime at temperatures below the phase transition temperature and can result in the ejection of large volumes of material in the form of particulate.

The conditions of IR ablation and ion formation in the mid-IR are such that it is possible to move from conditions of stress confinement to thermal confinement with minor changes in system configuration. For example, Leisner et al. used a 5 ns pulse width OPO and a 100 ns Er:YAG laser, which resulted in acoustic confinement with the former and thermal confinement conditions with the latter.[120] In the absence of phase transition or chemical reaction, the characteristic time for thermal energy dissipation in glycerol is given by[99]

$$t_d = \frac{1}{\kappa \alpha^2}$$

where κ is the thermal diffusivity (9×10^{-8} m^2/s) and α is the optical absorption coefficient. At 2.94 µm, the optical absorption coefficient is 650 /mm and the time for thermal energy dissipation is 26 µs. At 3.05 µm, the optical absorption coefficient is 130 /mm and the time is 66 µs. Since the laser pulse width is 5 ns, the conditions for thermal confinement met at all wavelengths used in this experiment.

The characteristic time for acoustic energy dissipation can be calculated from

$$\tau_{ac} = 1/\alpha v ,$$

where, v is the acoustic speed in glycerol and α is the optical absorption coefficient. From the above absorption coefficient values, and the speed of sound in glycerol of 1900 m/s, the time for acoustic energy dissipation is 0.8 ns at 2.94 μm, 2 ns at 3.05 μm, and 4 ns at 3.2 μm. At the peak of the IR absorption, the system is in the regime of stress confinement, but moves away from that regime as the wavelength moves away from the IR absorption maxima.

The volumetric energy density can be calculated from $\varepsilon = \alpha H_0$, where H_0 is the threshold fluence shown in Figure 3-7 and Table 3-1. At threshold, the energy density is nearly the same at all wavelengths and corresponds to approximately 100 kJ/mol, compared to the heat of vaporization of glycerol of 75 kJ/mol.[22] Thus the energy density is comparable at all wavelengths and is sufficient to achieve a complete phase transition for the irradiated volume element. Under all conditions there is sufficient energy for phase transition and therefore spallation of the sample is unlikely to occur. The photoacoustic studies also suggest that material is removed by explosive boiling rather than spallation.[90]

From the above estimates, it appears that the ablation of glycerol with the OPO can be tuned into or out of the regime of stress confinement using the wavelength of the light. Under all conditions there is sufficient energy for an explosive phase transition and the decrease in particle

size in stress confinement regime is consistent with a explosive phase transition mechanism rather than a spallation mechanism, which is expected to lead to ejection of larger particles.[98, 121]

The size distribution of ejected particulate is challenging to model because it encompasses multiple routes to formation in the small and large particle size regimes.[122] Particles below 100 nm in diameter are primarily formed by condensation in the supersaturated plume of ejected gas. The nucleated particles can go on to coagulate and coalesce to form larger particles. Particles above 100 nm can be formed by sputtering and by phase explosion. Because conditions can vary throughout the laser beam and sample, some of the above mechanisms can be occurring simultaneously. For example, condensation of zinc vapor onto copper enriched droplets ablated from brass has been observed previously.[123]

3.5. Summary

Laser ablation of glycerol was accomplished in the thermal and stress confinement regimes with the degree of stress confinement determined by the wavelength of the infrared laser. Stress confinement was obtained over a broad wavelength region that encompassed the CH and OH stretch vibrational absorption peaks and was associated with smaller particles and higher concentration of particles at a given fluence. The energy threshold for particle formation is lowest at the IR absorption maxima for glycerol and highest with the laser tuned off of the vibrational absorption resonance.

CHAPTER 4. POST LASER PARTICLE ABLATION*

4.1. Introduction

In the previous chapter, it was found that the selection of the infrared wavelength and energy

has a profound effect on the resulting particle size distribution.[124] The particle size distribution

can also be changed by irradiating the plume of expanding material with a second laser. In the

work described in this chapter, a UV laser was used to irradiate the plume of expanding material

created by the mid-IR OPO laser system. The 2.94 μm laser was used to ablate particles from a

thin film of the liquid MALDI matrix 3-nitrobenzyl alcohol (NBA) at atmospheric pressure. A

351 nm excimer laser directed parallel to and a few millimeters above the target surface was used

to irradiate the plume of desorbed material. The particle concentration, mean particle size, and

particle size distributions were recorded as a function of the time delay between the IR and UV

laser pulses. The mean initial velocities of the ejected particles from sample target were obtained

from the time delay plots.

4.2. Experimental

A 1 mm thick deposit of NBA was prepared by dropping a 3.0 μL neat NBA onto a stainless

steel sample target, which was placed at the center of the ablation chamber (described in Chapter

2, Section 2.2). The two laser systems used in this experiment were the OPO laser, described in

Chapter 2, Section 2.1, and the excimer laser, described in Chapter 2, Section 2.2. Although the

OPO is tunable from 1.4 to 4.0 μm, it was fixed at 2.94 μm for this work. The excimer used a

---

*Reprinted by the permission of Elsevier.

OPO is tunable from 1.4 to 4.0 µm, it was fixed at 2.94 µm for this work. The excimer used a xenon fluoride gas mix for operation at the wavelength of 351 nm. Particles generated by 2.94 µm pulsed IR laser ablation of liquid NBA were irradiated with a 351 nm UV laser 3.5 mm above and parallel to the sample target. The size and concentration of the ablated particles were measured with the light scattering particle sizer, described in Chapter 2, Section 2.1. The particle size measurement was initiated 10 s after the laser began irradiating the sample to assure that a steady supply of particles was being created. Signals were integrated for a total of 10 s, which corresponds to 20 laser shots.

4.3. Results

The size distributions of ablated particles for different delay times are show in Figure 4-1. The IR and UV fluences were 1900 and 2400 J/m^2, respectively. The height of each vertical bar indicates the concentration of ejected particles measured in the indicated aerodynamic diameter range and the y-axis in each plot extends from zero concentration to 30 cm^{-3}. The total particle concentration, obtained by summing the counts in each of the size ranges, is given in Table 4-1. This table includes both the particle concentration in terms of particles per unit volume as well as the mass-weighted concentration in terms of total mass of particulate per unit volume. The maximum total particle concentration was 400 cm^{-3}, which was observed at 20 µs delay time (Figure 4-1c). This value is more than 5 times the baseline concentration with the IR laser alone (Figure 4-1a).
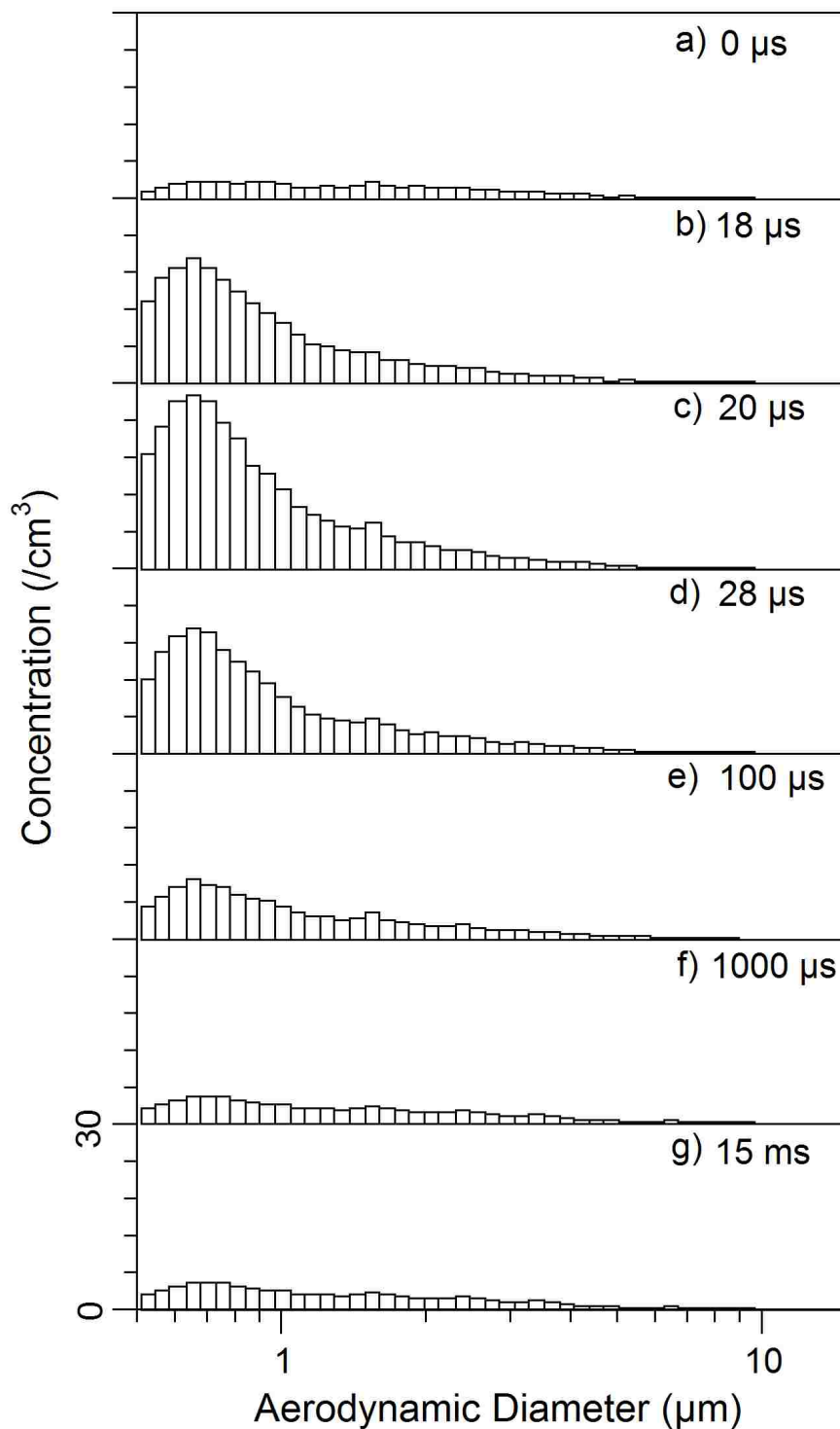
Figure 4-1 Particle size distribution for IR laser ablation and UV post-irradiation of 3-nitrobenzyl alcohol at UV laser delay times of a) 0 µs; b) 18 µs; c) 20 µs; d) 28 µs; e) 100 µs; f) 1000 µs; g) 15 ms. IR and UV fluences were 1900 and 2400 J/m^2, respectively.

Table 4-1 Concentration and average size of ablated particles when IR and UV fluences are 1900 and 2400 J/m^2 at different delay times.

Delay Time (μs)	Particle Concentration (/cm^3)	Mean Particle Size (μm)	Peak Particle Size (μm)	Mass-weighted Concentration (mg/m^3)	Mean Mass-weighted Particle Size (μm)
0	70	2.12	1.17	2.05	9.88
15	100	1.88	0.85	2.03	9.67
18	280	1.27	0.70	2.06	9.20
20	400	1.20	0.70	2.09	9.02
24	330	1.24	0.70	2.08	9.24
37	230	1.36	0.70	2.07	9.51
100	160	1.54	0.70	2.01	9.63
300	100	1.83	0.75	2.09	9.73
1000	90	1.90	0.78	2.02	9.81
7000	80	2.01	0.88	2.08	9.79
15000	70	2.09	1.09	2.04	9.97

A plot of the UV fluence dependence of the particle concentration is shown in Figure 4-2. The IR laser fluence was 1900 J/m^2 and the delay time was 20 μs. The threshold for two-laser particle formation was near 250 J/m^2. Between this fluence and 900 J/m^2, the particle concentration increased linearly with a slope of 25 particles/cm^3 per 1000 J/m^2. Between 900 and 1600 J/m^2, the rise was linear, but the slope increased by a factor of 25. Above 1600 J/m^2, the slope decreased to near the initial value.
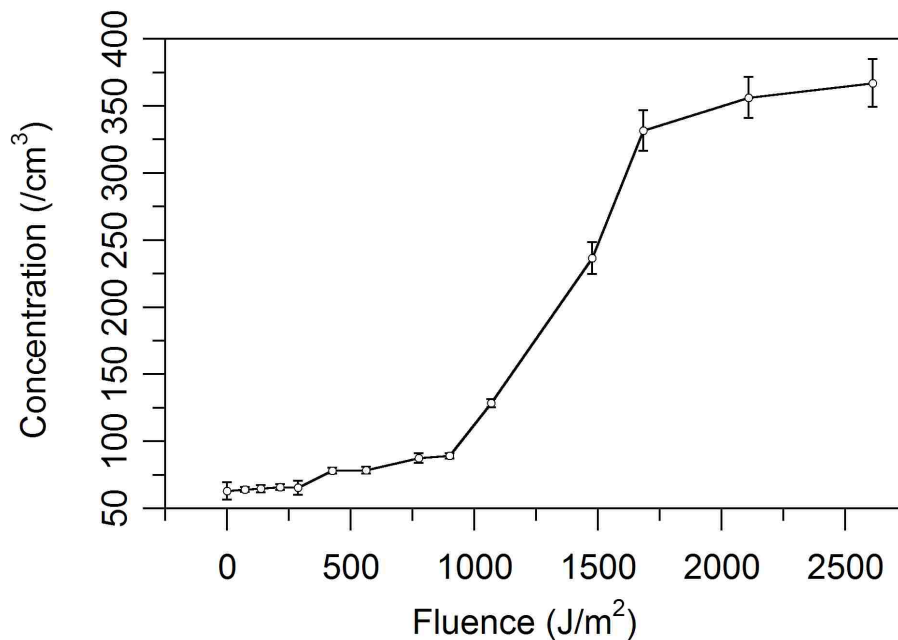
Figure 4-2 UV fluence dependence of the ablated particle concentration at an IR fluence of 1900 J/m^2 and 20 μs delay.

The particle concentration and the size distribution of the particles changed with the delay time. The peak particle sizes at various delay times are listed in Table 4-1. The peak particle size was obtained by determining the centroid of the distribution for all points greater than 60% of the maximum. At zero delay, the peak particle size was 1.17 μm. The peak particle size decreased to

77

0.70 μm after 20 μs and stayed constant from 18 to 100 μs before it began to increase. After 15

ms, the peak particle size increased to 1.09 μm.
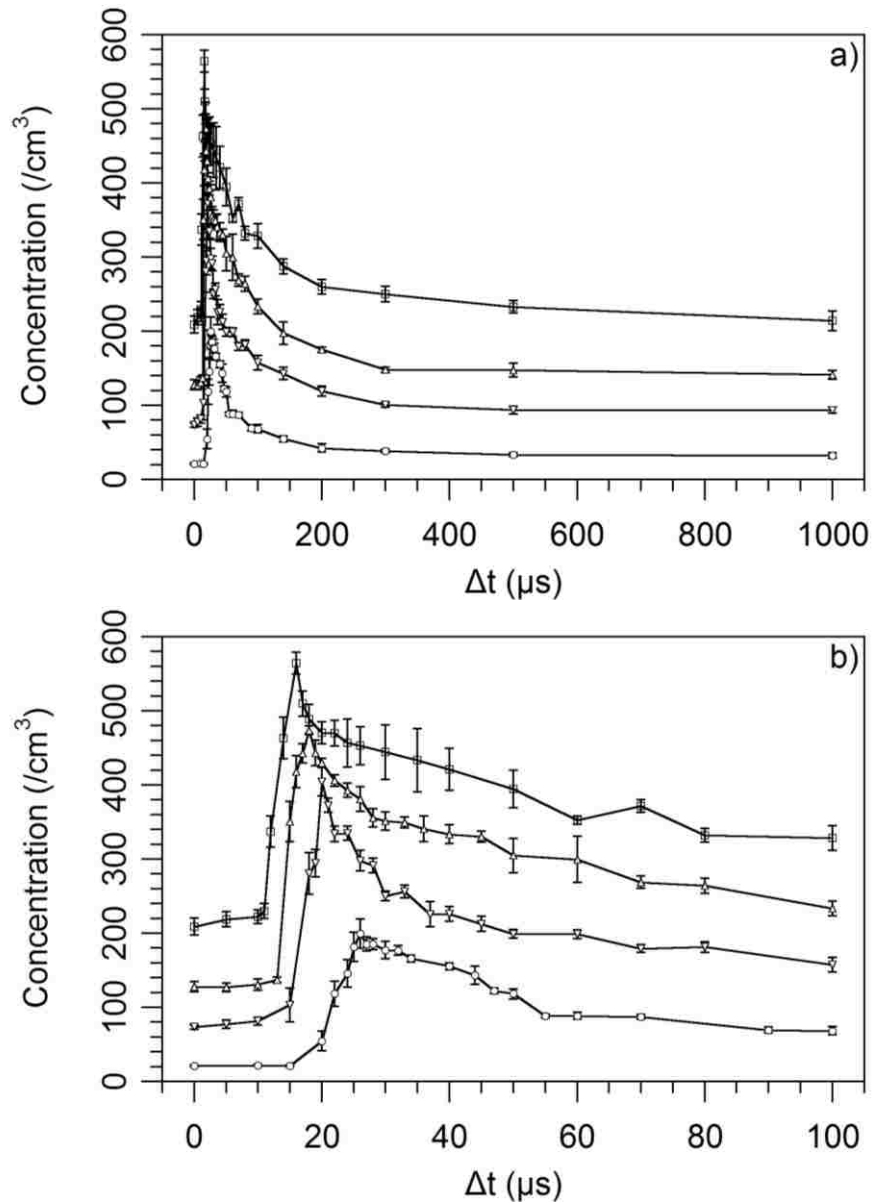
Figure 4-3 Delay time dependence of particle concentration at different IR fluences ((□) 2700 J/m^2, (Δ) 2100 J/m^2, (▽) 1900 J/m^2, (○) 1600 J/m^2) at delay times from zero to (a) 1000 μs and (b) 100 μs. The UV laser fluence was 2400 J/m^2.

Shown in Figure 4-3 is the delay time dependence of the total particle concentration at

different IR fluences of 1600, 1900, 2100, and 2700 J/m^2 with the UV laser fluence held constant

at 2400 J/m^2. Figure 4-3a shows the time behavior between 0 and 1000 μs and Figure 4-3b is an

expansion of the time range between 0 and 100 μs. At zero delay there was no UV laser

interaction with the ablated material and the concentration of particles (baseline) increased with

IR fluence. At delay times between 10 and 30 μs, the plume of ablated material moved into the

path of the UV laser beam and irradiation with the UV laser lead to particle break-up and a

greater particle count. The concentration increase that resulted from the UV laser continued

beyond 200 μs, suggesting that particulate is emitted from the surface long after the IR laser has

irradiated it.
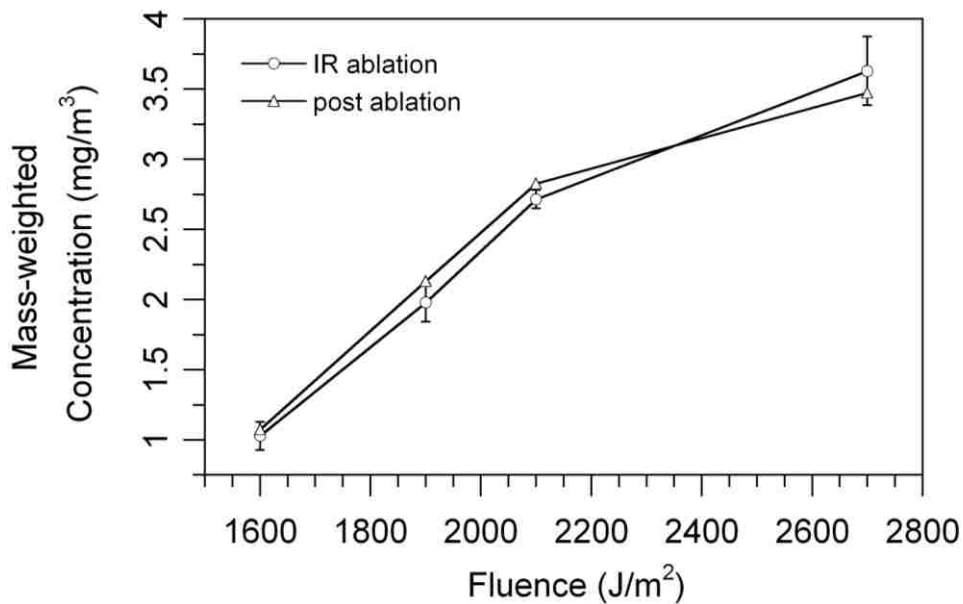
Figure 4-4 Mass-weighted concentration with IR laser (○) and IR plus UV laser (Δ) at the peak particle concentration. The UV laser fluence was 2400 J/m^2.

Figure 4-4 shows the mass-weighted concentration of ablated particles at different IR laser

fluences with the IR laser alone and with the UV laser at a fluence of 2400 J/m^2 and at the delay

time corresponding to maximum particle count at each fluence. Although the UV laser had a

large effect on the total particle concentration (see Figure 4-3), the total mass of particulate was

not significantly affected by the second laser.
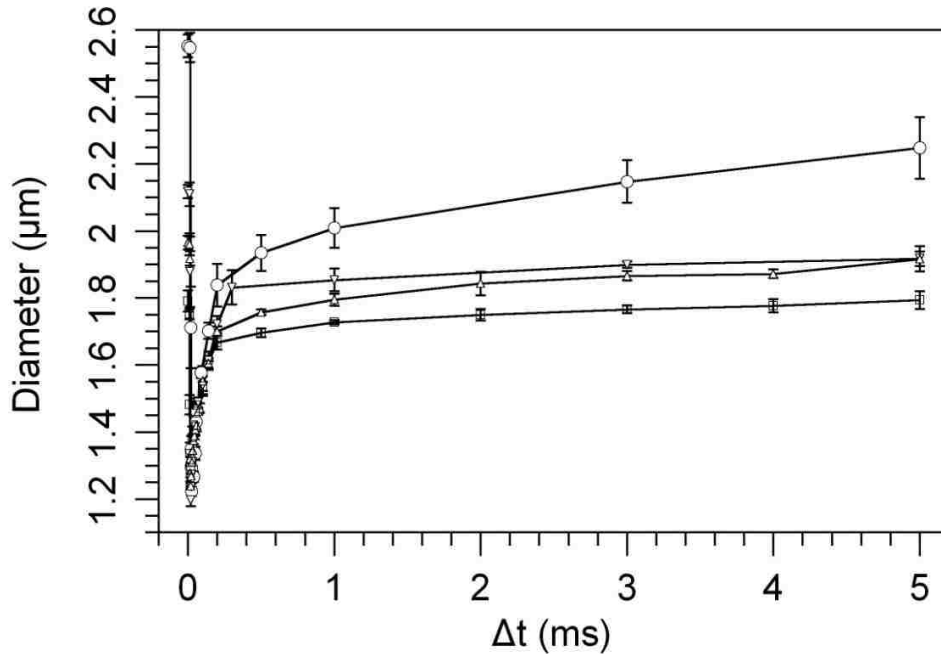
Figure 4-5 Particle diameter as a function of delay time at IR ablation fluences of (○) 1600 J/m^2, (▽) 1900 J/m^2, (△) 2100 J/m^2, and (□) 2700 J/m^2 at delay times from zero to 5000 μs. The UV fluence was 2400 J/m^2.

Plots of the mean particle size at different delay times are shown in Figure 4-5. The UV

fluence was 2400 J/m^2 and the IR fluence was 1600, 1900, 2100, and 2700 J/m^2. In all cases,

there was a rapid decrease in particle size as the plume passed the UV laser beam at delays near

20 μs. There was a minimum for particle size near 26, 20, 18, and 16 μs when the IR fluence was

1600, 1900, 2100, and 2700 J/m^2, respectively. These time delays correspond to the positions of

the maxima of particle concentration (see Figure 4-3). As with the particle concentration results,

the decrease in particle size was observed for delays of several milliseconds between the IR laser

and UV laser firing, suggesting delayed ejection of material from the surface. The mean particle

sizes at different delay times for an IR laser fluence of 1900 J/m^2 are indicated in Table 4-1.
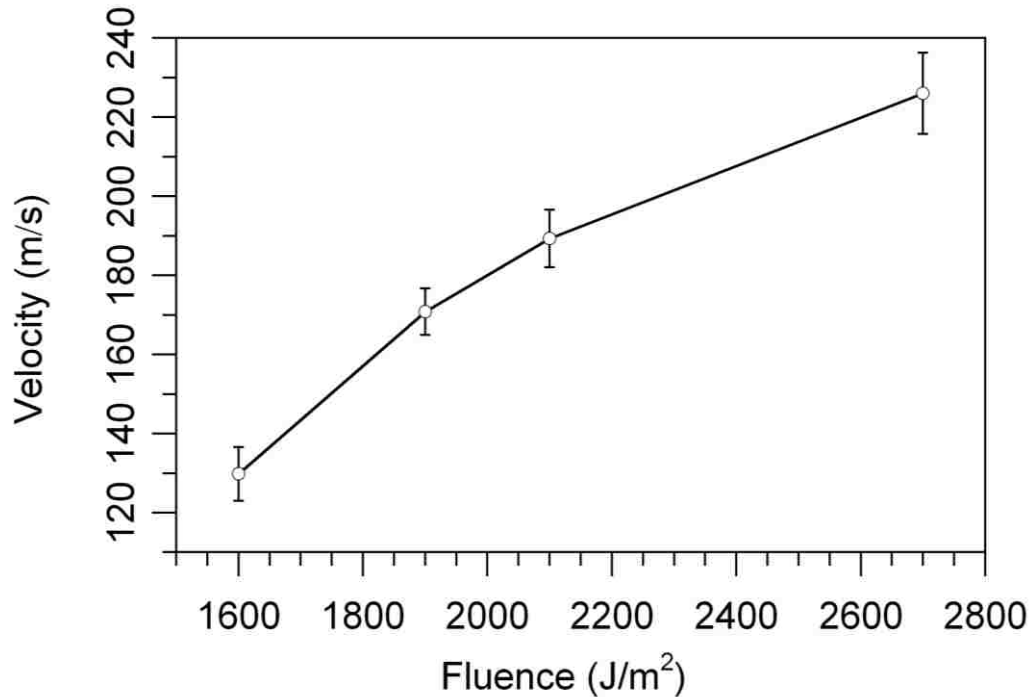
Figure 4-6 The ejected particle velocity as a function of IR fluence.

Since the distance between the target surface and the center of the UV laser beam was fixed

at 3.5 mm, the average velocities of plume front can be obtained from the delay time

corresponding to the maximum of the particle concentration plot of Figure 4-3. Figure 4-6 shows

a plot of the particle plume velocity obtained from the maximum particle concentration. The

plume front velocity increased linearly from 130 m/s at 1600 J/m^2 to 220 m/s at 2700 J/m^2.

4.4. Discussion

The above results demonstrate that it is possible to affect a significant break-up of the

micrometer-sized particulate ablated from a sample using a UV laser. The particle concentration

can be increased by nearly an order of magnitude, but the total mass of ejected material was not greatly affected, suggesting that the UV laser was breaking the large particles into smaller ones rather than causing complete vaporization.

The mechanism of IR laser material ejection can be understood in terms of the thermomechanical response of the nitrobenzyl alcohol matrix material to the pulsed IR laser.[99] The energy per unit volume deposited in the nitrobenzyl alcohol by the IR OPO is given by

$$\frac{E}{V} = 2.3(1 - R)\varepsilon_n c_n H_0$$

where R is the surface reflectance, ε_n is the molar decadic absorption coefficient, c_n is the molar concentration, and H_0 is the laser fluence.[125] The molar decadic absorption coefficient of NBA is not known, but measurements made for glycerol and other alcohols suggest that it is in the range of 100 L/mol cm.[102] The IR laser fluence was in the range of 2000 J/m^2 for these studies and the reflectance is estimated to be 0.1. The molar concentration of the NBA liquid is 8500 mol/m^3. These values lead to an energy density of 4×10^8 J/m^3 or 40 kJ/mol. The heat of vaporization of NBA is not available; however, this value can be compared to the heat of vaporization for benzyl alcohol of 60 kJ/mol.[126] The values are of the same magnitude, suggesting that the volumetric energy density of the NBA following IR laser irradiation is close to that required for a phase transition.

The temperature rise in the absence of phase transition can also be calculated based on the energy absorbed and assuming there is no phase change, the increase in temperature is given by

$$\Delta T = \frac{E}{V}\frac{1}{c_v \rho}$$

where c_v is the heat capacity of NBA and ρ is the density. Taking the heat capacity to be 200

J/mol K, the predicted temperature rise is 210 ºC to a final temperature of 235 ºC. This is well

above the boiling point between 175 and 180 ºC and approximately 75% of the estimated critical

temperature.[127] If the sample is heated rapidly to approximately 90% of the critical temperature,

the superheated material can undergo an explosive phase transition that results in volume

ejection of the upper layers of the sample.[28, 96, 98-99] It appears likely that these conditions may be

in effect, especially for higher laser energy levels.

The phase change can occur in either the stress or thermal confinement regime depending on

the rate of energy relaxation. The time for thermal energy dissipation in a liquid MALDI matrix

is on the order of microseconds,[90] thus the system was most likely within the thermal

confinement regime under all of the experimental conditions described above. The characteristic

time for acoustic energy dissipation is given by

$$\tau_{ac} = \frac{1}{\alpha c}$$

where α is the IR absorption (~200/mm) and c is the speed of sound in NBA (~1000 m/s). When

energy is added to the system on a time scale less than τ_{ac}, the system is in the stress confinement

regime. Using the above values, the acoustic relaxation time is ~5 ns and nearly identical to the

laser pulse width. This puts the system at the stress confinement limit.

Time-resolved imaging has been used to study the ejection of material from liquid samples under vacuum using mid-IR lasers (A fast photography study of IR laser ablation under atmospheric pressure conditions is described in Chapter 5). Leisner *et al.* used dark field images to measure plume density and right angle scattering to image ejected particulate from a glycerol sample.[27] They found different plume dynamics for lasers operating in the thermal and stress confinement regimes. A 5 ns OPO, similar to the one used in this work, was found to generate a denser plume with more particulate compared to a 100 ns Er:YAG laser. Pressure confinement was not achieved with the longer pulse width Er:YAG at 5200 J/m^2 fluence, but it was at or near that regime with the OPO at 2800 J/m^2 fluence. The OPO ejected material plume showed the lift-off of the entire glycerol layer that subsequently disintegrated into particulate. In contrast, the Er:YAG-induced plume resulted in smaller particles that coalesced to form larger particles as the plume expanded. Rohlfing *et al.* performed a photoacoustic analysis of glycerol IR ablation under similar conditions and found a distinct contrast in the pressure pulse signals of the OPO compared to the Er:YAG.[90] The OPO was found to generate more than an order of magnitude greater thermoelastic stress and this led to a rapid phase explosion and lift-off of the entire irradiated volume.

Recent high-speed photographic studies of 2.94 mm Er:YAG laser ablation of water reveal a two-step process involving the rapid boiling and ejection of water molecules at 1000 m/s that is followed by the lift-off of particles at velocities about an order of magnitude slower.[28] The

slower particle ejection process is caused by the recoil of the shock wave induced by the initial laser-induced phase transition. Although the particulate jet extends several millimeters after a few tens of microseconds, the particulate continues to be expelled for as long as 500 ms after the IR laser fires. The onset of shock wave induced material ejection occurred at 5400 J/m^2, which corresponds to an irradiance of 1000 W/m^2, given the 70 ns pulse width of the laser. This can be compared to the results presented above that were obtained at fluences of 1000–2000 J/m^2, which correspond to irradiances of $(2\text{-}4) \times 10^{11}$ W/m^2. The higher irradiance of the OPO leads to volume ejection of material.[27-28, 90]

The UV laser used in our experiments appears to be irradiating a plume of particulate similar to that ablated from water[28] and glycerol[27]. The maximum concentration (Figure 4-3) and minimum particle diameter (Figure 4-5) are consistent with the irradiation of particulate material ejected in the initial formation of droplets after explosive vaporization, followed by irradiation of particulate material at longer time delays that results from the recoil-induced material expulsion process. Although extended material emission to more than 3 µs has been observed with the IR OPO laser system irradiating a glycerol sample at 3000–5000 J/m^2, emission beyond several tens of microseconds was not observed.[27] Under a vacuum, the plume expands freely without collision; the lack of a confined and slowly expanding plume could explain the lack of extended material emission. This is discussed further in Chapter 5.

The velocity of ions emitted from MALDI matrix material under vacuum has been reported at 5000–1000 m/s,[112] consistent with the high velocity of primary material ejection. By contrast, ions formed by irradiation of ablated particles with a second laser are formed for tens of microseconds after the IR irradiation of the target.[120, 128] This is consistent with an initial phase transition that ejects molecules and clusters, followed by a shock wave induced volume ablation of material that has been observed in previous fast photography studies. The rapid rise in the particle concentration seen in Figure 4-3 and drop in particle diameter between 10 and 20 μs after the IR laser pulse indicates the arrival of the front of the particle component of the ejected plume. The slow decay of the signal indicates the delayed emission of material from the sample. The rise in concentration drops below half its maximum within 50 μs and a return to the baseline is observed after more than 300 μs delay. The late time signal may be due to recoil-induced expulsion as well as coagulation of ejected particles above the target. Previous studies of high-speed photography of IR laser induced water ablation shows the formation of a column of material above the surface for more than 300 μs [102] and the studies reported in Chapter 5 show material ejection at even longer times. The column of ablated material is rapidly expelled and after 50 μs collapses into a cone and disintegrates. This is consistent with the strong effect observed in Figures 4-3 and 4-5 between 10 and 50 μs that probes the column of ablated material, followed by the weak effect after 50 μs that probes the disintegrating column.

Molecular modeling has been used to simulate the break-up of particles irradiated with a pulsed laser.[97, 129] The simulations indicate that a weakly absorbing particle that is uniformly heated will be completely evaporated. In the case of a strongly absorbing particle, the energy is absorbed on the side facing the laser. The irradiated material evaporates while the material that has not been heated breaks up into smaller particles. The UV absorption coefficient of NBA has not been reported, but it is known that a typical MALDI matrix has an absorption of 6×10^4 cm^{-1}.[130] This indicates a penetration depth of about 160 nm, which is qualitatively consistent with the observed particle size reduction. The sigmoidal shape of the concentration plot of Figure 4-2 can be interpreted in light of this proposed mechanism. According to this model, the UV fluence range up to 1000 J/m^2 represents removal of material from the surface of the particle by evaporation and limited break-up of the material that has not been irradiated. Using the estimated absorption from above, the energy density in the NBA particle will exceed 60 kJ/mol above 1000 J/m^2 UV fluence. We postulate that the concentration increases rapidly between 1000 and 1800 J/m^2 because there is sufficient volumetric energy to achieve a rapid phase transition throughout the irradiated element. This result in a more efficient break-up of the portion of the particle that has not been irradiated and therefore a higher measured particle concentration. Above 1800 J/m^2, the phase explosion effect is saturated and additional fluence does not lead to a large increase in particle concentration.

4.5. Summary

Particles ablated from a sample of 3-nitrobenzyl alcohol can be broken up by irradiation with a UV laser directed at the plume of expanding material. The optimum delay between the IR and UV lasers was between 16 and 26 µs and was dependent on the fluence of the IR laser: higher fluence leads to a more rapid appearance of particulate. The particle plume expands at a velocity of several hundred m/s and is sufficiently concentrated that the UV laser is able to increase the particle concentration three to nine times while decreasing the particle size by one-third to one-half. The plume velocity is dependent on the IR laser fluence and ranged from 130 m/s at 1600 J/m^2 to 220 m/s at 2700 J/m^2. Ejection of material from the sample occurred over a prolonged time period; the effects of the UV laser on the particle plume were observed for several ms after the IR laser was fired at the sample. The observed particle emission dynamics is consistent with a rapid phase transition and plume expansion, followed by an extended emission of particles ablated from the target surface.

CHAPTER 5. WAVELENGTH AND TIME-RESOLVED IMAGING OF MATERIAL EJECTION IN INFRARED LASER DESORPTION

5.1. Introduction

In the previous two chapters, experiments were described that involve the counting and sizing of particles resulting from ablation of samples and, in the previous chapter, laser irradiation of the plume to induce additional particle breakup. In addition to particle sizing, fast photography can be used to investigate laser ablated plumes. In the work described in this chapter, infrared laser ablation of glycerol at atmospheric pressure was studied using fast photography. Images of 90º scattered light from mid-infrared laser generated plumes were obtained at different delay times. The illumination laser was an excimer pumped dye laser operating in the visible wavelength region and the time delay between the IR and dye laser was varied up to 1 ms. Two models for plume propagation, the shock wave model and drag wave model, were used to fit the experimental data.

5.2. Experimental

An approximately 1 mm thick and 6 mm in diameter deposit of neat glycerol was prepared on a stainless steel sample target, which was mounted on the xyz stage (described in Chapter 2, Section 2.3). The pulsed IR beam from OPO was directed through a 254 mm focal length CaF_2 lens and irradiated the target at normal incidence. The wavelength of the infrared source was tunable and was varied between 2.7 and 3.5 μm for the studies. After an adjustable delay, the

excimer pumped dye laser (described in Chapter 2, Section 2.3) was used to illuminate the

expanding plume and the 90º scattered light was imaged with a high speed CMOS camera

(described in Chapter 2, Section 2.3). The dye laser was oriented perpendicular to the ablation

laser and parallel to the sample surface to obtain the desired time resolution at the nanosecond

and microsecond level. After different time delays of the initial IR OPO pulse, the scattered light

from the glycerol plume was recorded by the CMOS camera.

5.3. Results

Photographs of glycerol ablation at a 2.94 μm wavelength and a fluence of 3000 J/m^2 are

shown in Figure 5-1. This wavelength is close to the OH stretch absorption maximum in liquid

glycerol and is useful for comparison to the fixed wavelength Er:YAG laser. The laser fluence

exceeds the ablation threshold and a plume above the material surface is created. From Figure

5-1, the onset of plume ejection was just barely visible at the 10 ns delay image (Figure 5-1a). In

subsequent exposures, a clear contact boundary was formed between plume and ambient air and

the dynamic expansion of the plume under atmospheric pressure was determined by the

properties of the material and the background gas. The propagation distance of the plume front

was around 100 μm at 100 ns time delay and by 1 μs a mushroom shaped plume was formed. As

the plume evolved into the tens of microsecond time regime (Figure 5-1 e–g), the frontal

boundary became perturbed and the plume deceleration increased. The plume broke up into a

large mushroom-like main plume and distinct larger droplets. The expansion front slowed

90

rapidly and the plume reached a point approximately 3 mm from the target at 1 ms delay. With

the increase of time delay, the diameter of mushroom stem expanded gradually from 200 µm at 1

µs (the laser diameter was 300 µm) to about 800 µm at 500 µs. The observed duration of the

plume was several milliseconds.
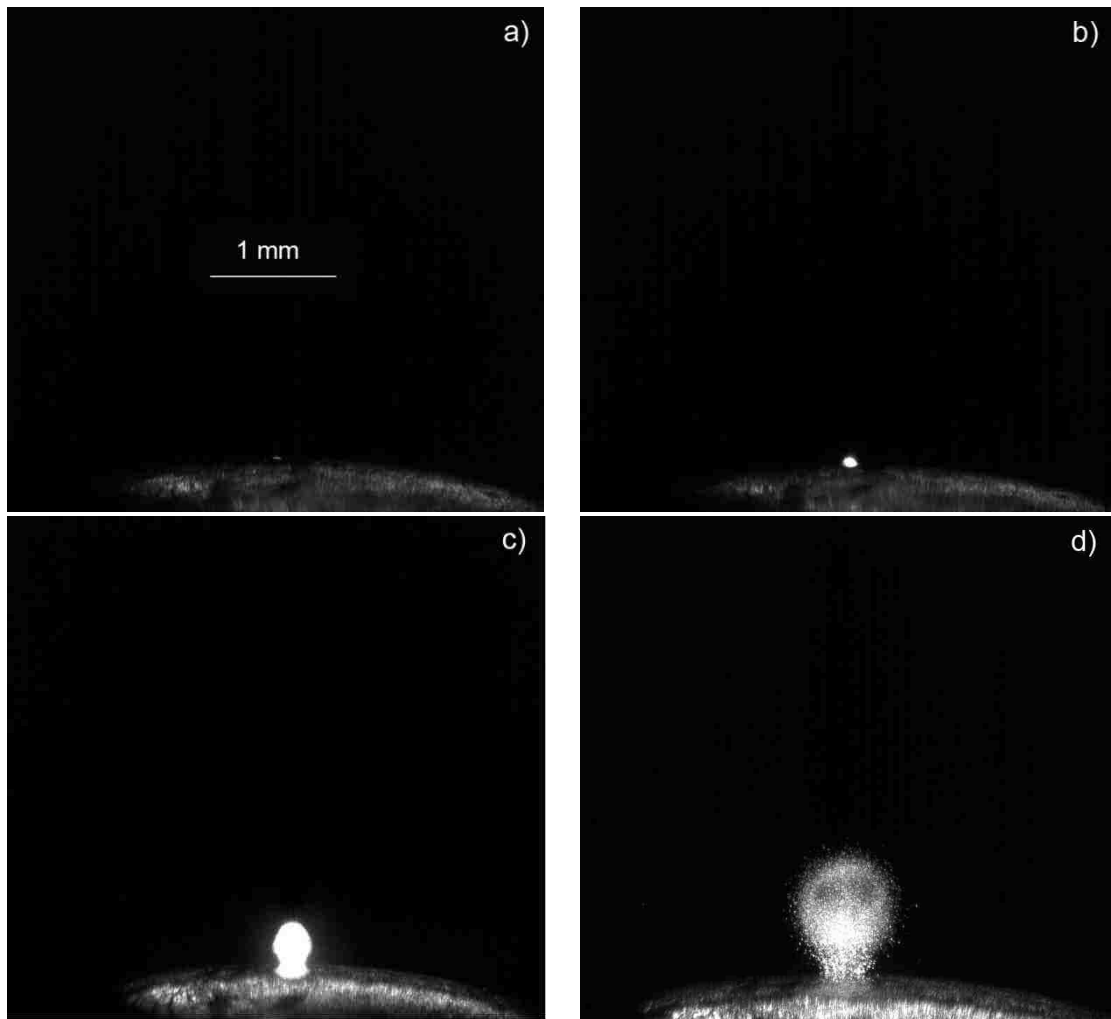
Figure 5-1 Glycerol ablation by OPO laser with wavelength 2.94 µm and fluence of 3000 J/cm^2
at different delay time: a) 10 ns; b) 100 ns; c) 1000 ns; d) 10 µs; e) 24 µs; f) 50 µs; g) 100 µs; h)
200 µs; i) 500 µs; j) 1000 µs.
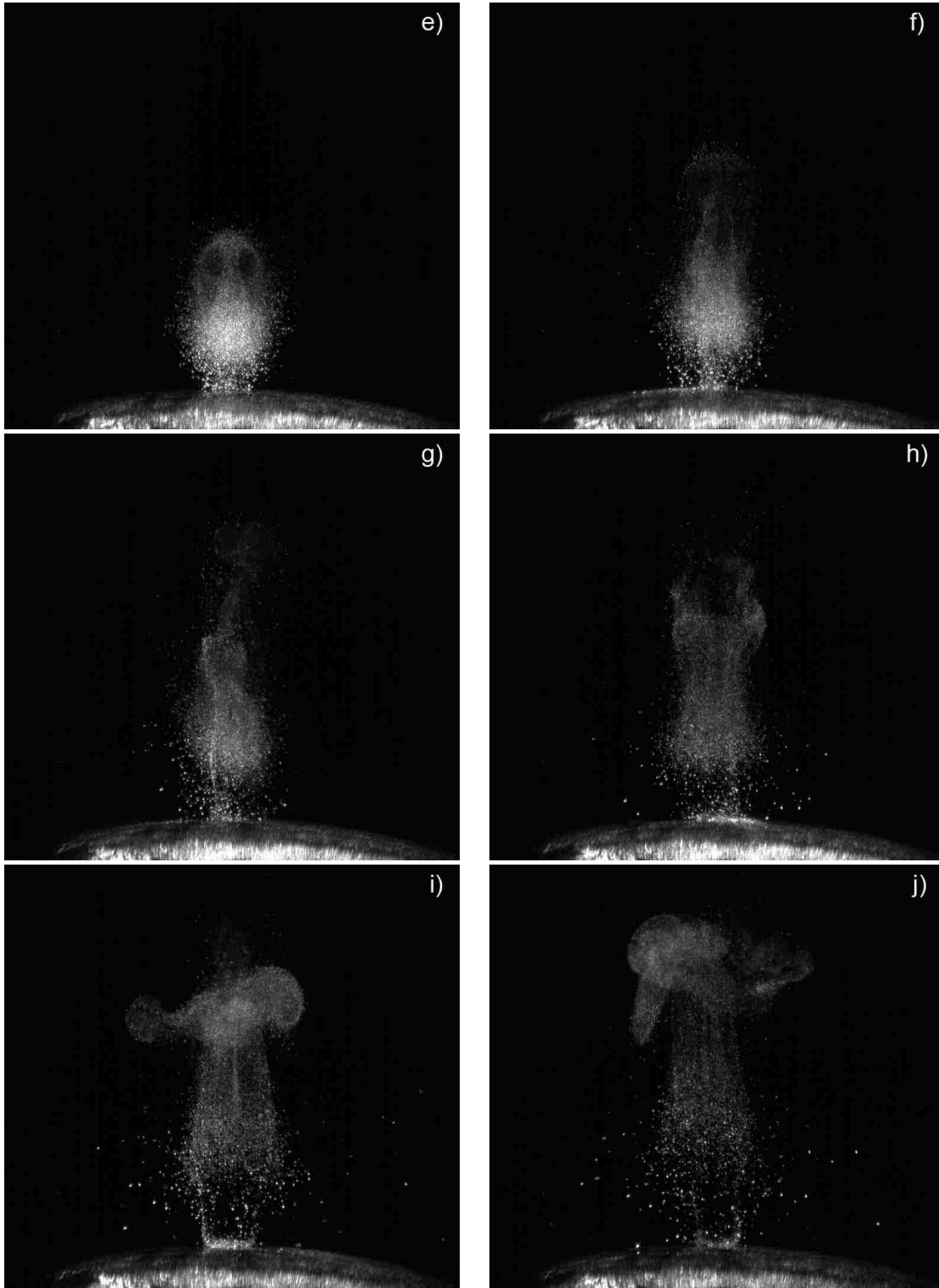
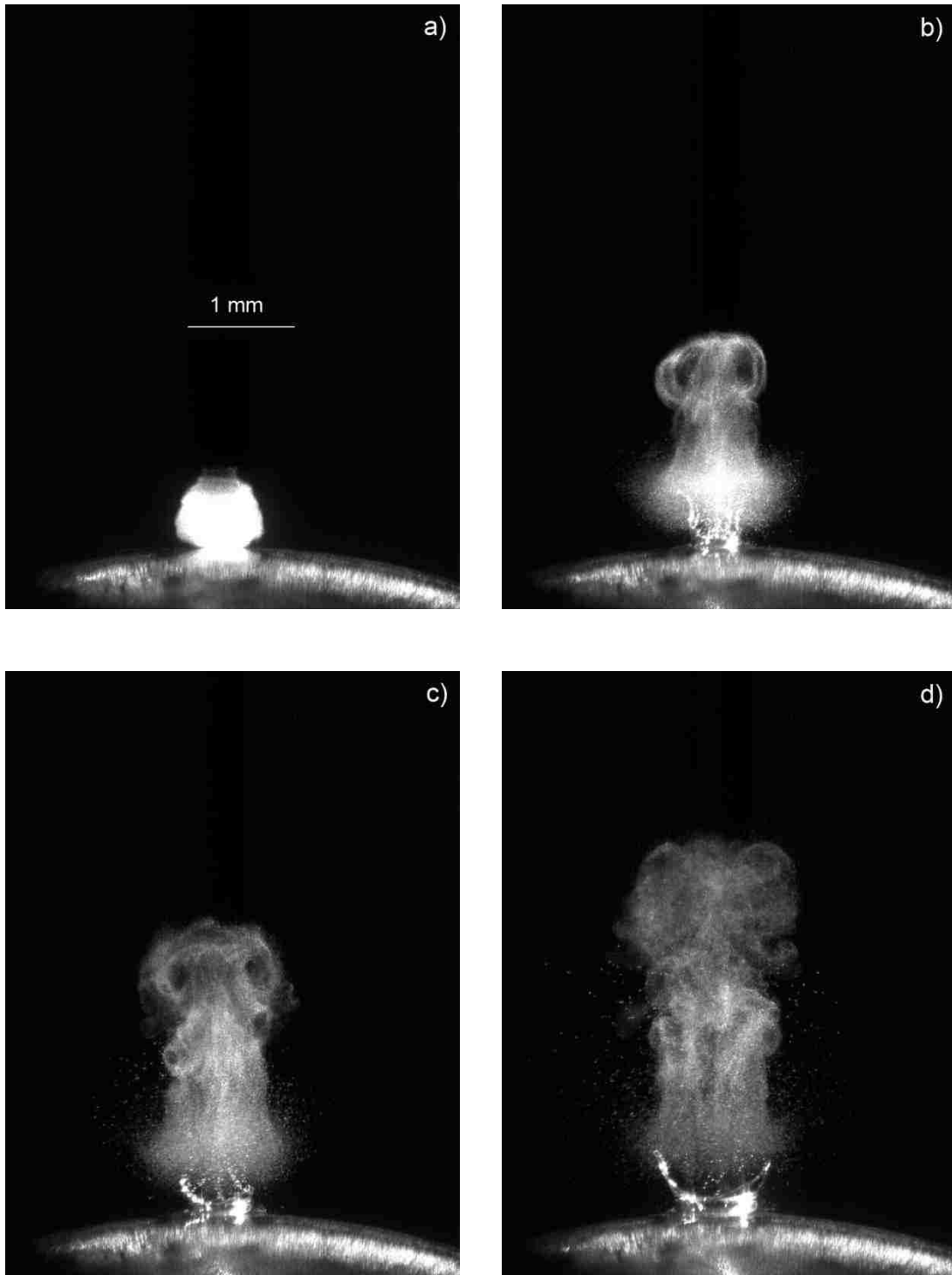**Figure 5-2** 2.94 µm wavelength IR laser-produced glycerol ablation at a fluence of 6000 J/m^2 at different delay time: a) 1 µs; b) 10 µs; c) 24 µs; d) 50 µs; e) 100 µs; f) 200 µs; g) 500 µs; h) 1000 µs.
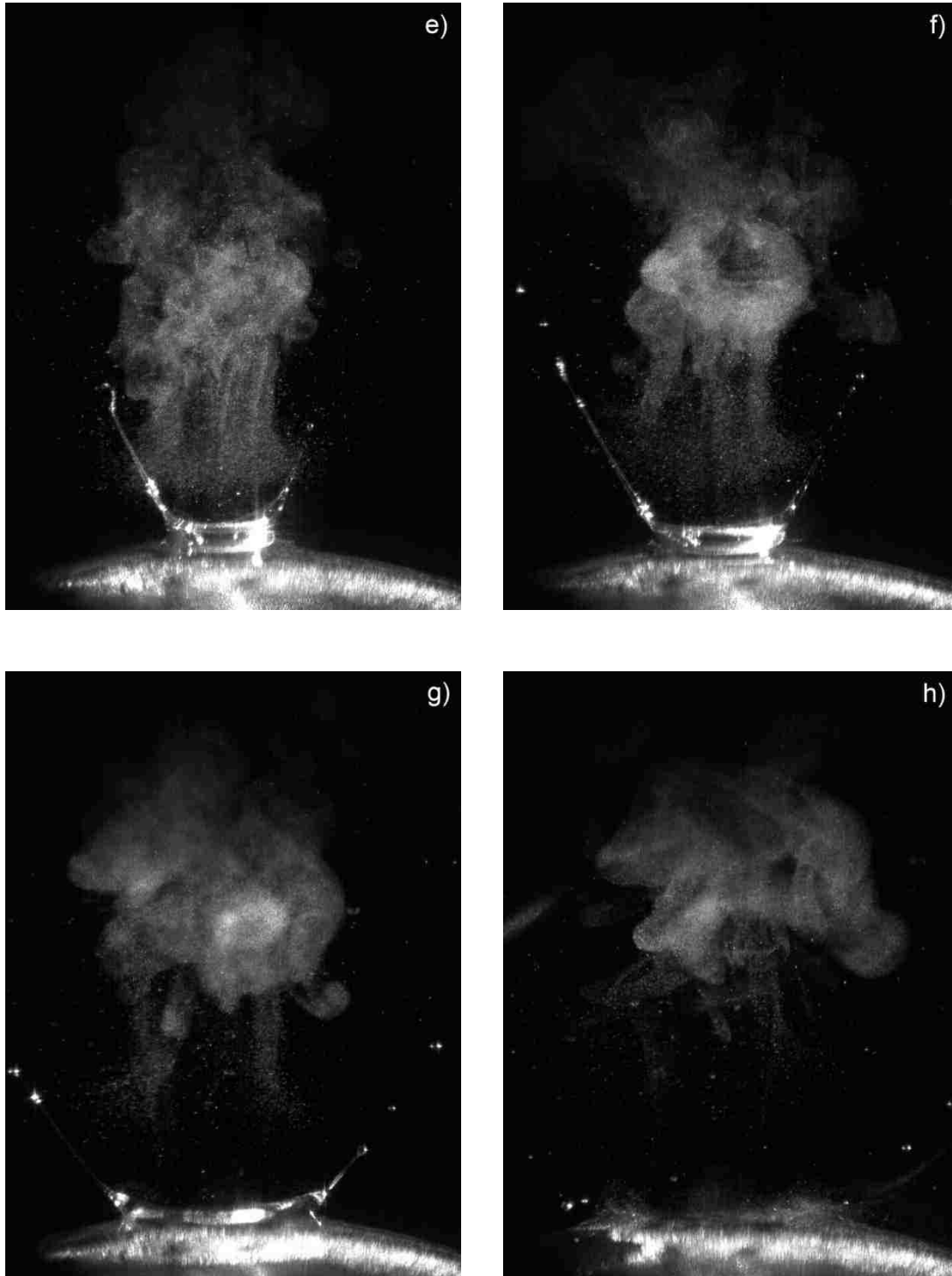
93

Figure 5-2 shows photographs of the glycerol ablation plume at 2.94 μm wavelength with a

laser fluence of 6000 J/m^2, twice the fluence of Figure 5-1. There are two distinct ejection

regimes at higher fluences: an initial ejection which is directed perpendicular to the glycerol surface and a later expulsion of material in a lateral direction, which can be seen in the $50 - 500$ µs delay in Figure 5-2. The latter expulsion is less noticeable at the 3000 J/m^2 fluence used for Figure 5-2, but a small component can be seen at 500 µs in Figure 5-1i. At 6000 J/m^2, the scattered light intensity for both the primary material ejection and the recoil-induced expulsion is greater. Also the diameter of the plume is larger: 350 µm at 1 µs and 1300 µm at 500 µm. The plume evolution of glycerol ablation at 2.94 µm wavelength was also investigated at a fluence of 9000 J/m^2 and corresponding photographs are shown in Appendix C.

Glycerol has a strong IR absorption at 3.0 µm due to the OH stretch and a less intense pair of peaks near 3.5 µm corresponding to the CH stretch bands.[124] Plume photographs were taken between 2.7 and 3.5 µm and the characteristics of the plume differed significantly in the OH stretch absorption region near 3.0 µm compared to the CH stretch region near 3.5 µm. Photographs of the ablation plume at 3.5 µm and 3000 J/m^2 fluence are shown in Figure 5-3. A defining characteristic of the plume at this wavelength is the narrow column of material approximately 50 µm in diameter that can be seen in Figure 5-3b at 10 µs. The propagation distance of plume front was less than 50 µm at 1 µs time delay, which was about one forth of the distance measured at 2.94 µm. At 10 µs delay, the plume front had expanded to a distance that nearly matches that observed at 2.94 µm (Figure 5-1d). However, the lifetime of plume expansion at 3.5 µm was much shorter than that at 2.94 µm. After 10 µs delay, the column of

ablated material broke up into droplets and after 50 µs, only several particles were visible. At

higher fluences, the quantity of ejected material was greater on the tens of microsecond time

scale, but prolonged material emission was not observed. Plume photographs of glycerol ablation

at 3.5 µm with laser fluence of 6000 and 9000 J/m^2 are shown in Appendix C.
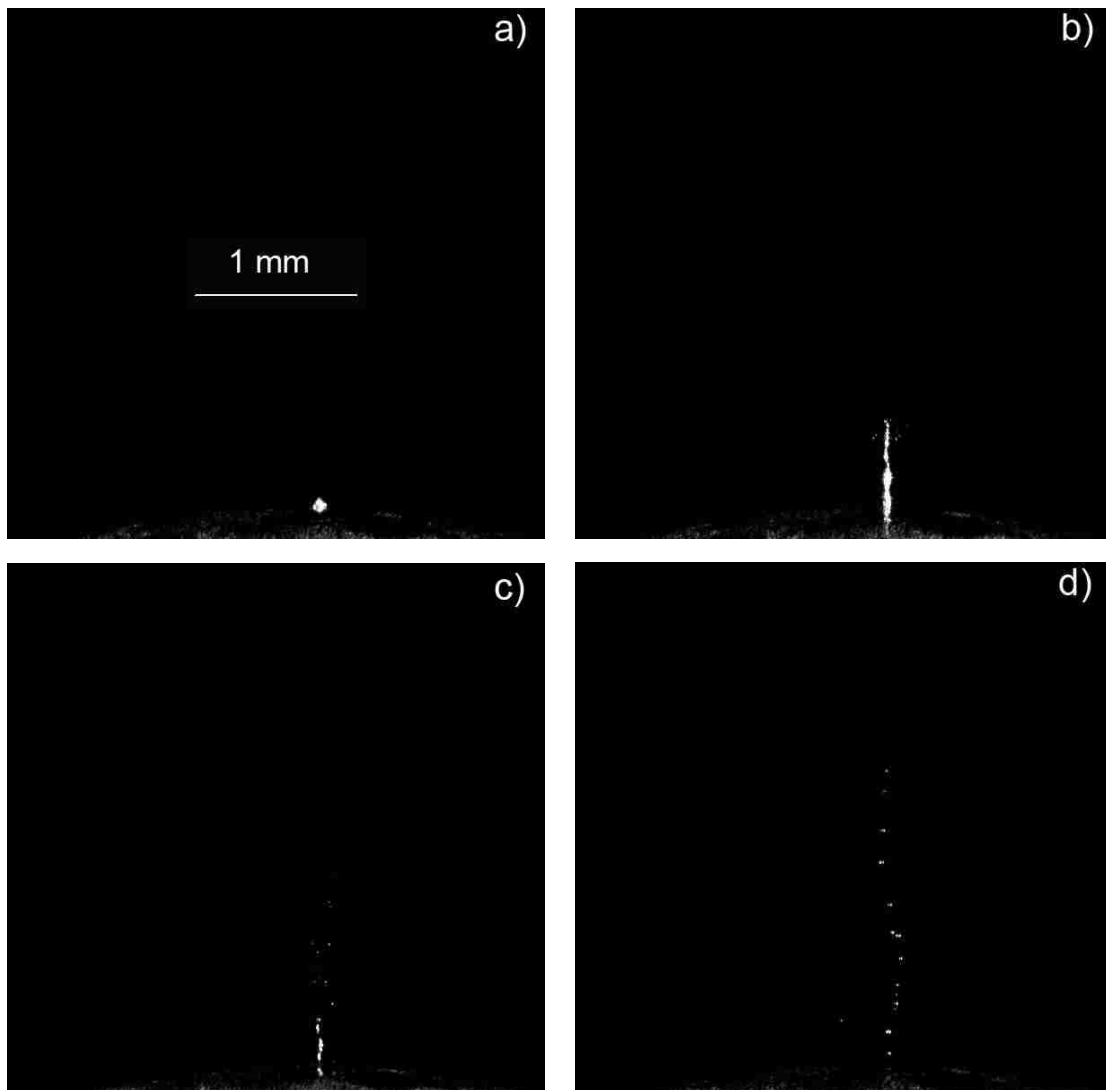
Figure 5-3 3.5 µm wavelength IR laser-produced glycerol ablation at a fluence of of 3000 J/m^2
at a) 1 µs; b) 10 µs; c) 20 µs; d) 50 µs; e) 100 µs; f) 200 µs; g) 300 µs; h) 500 µs delay time.
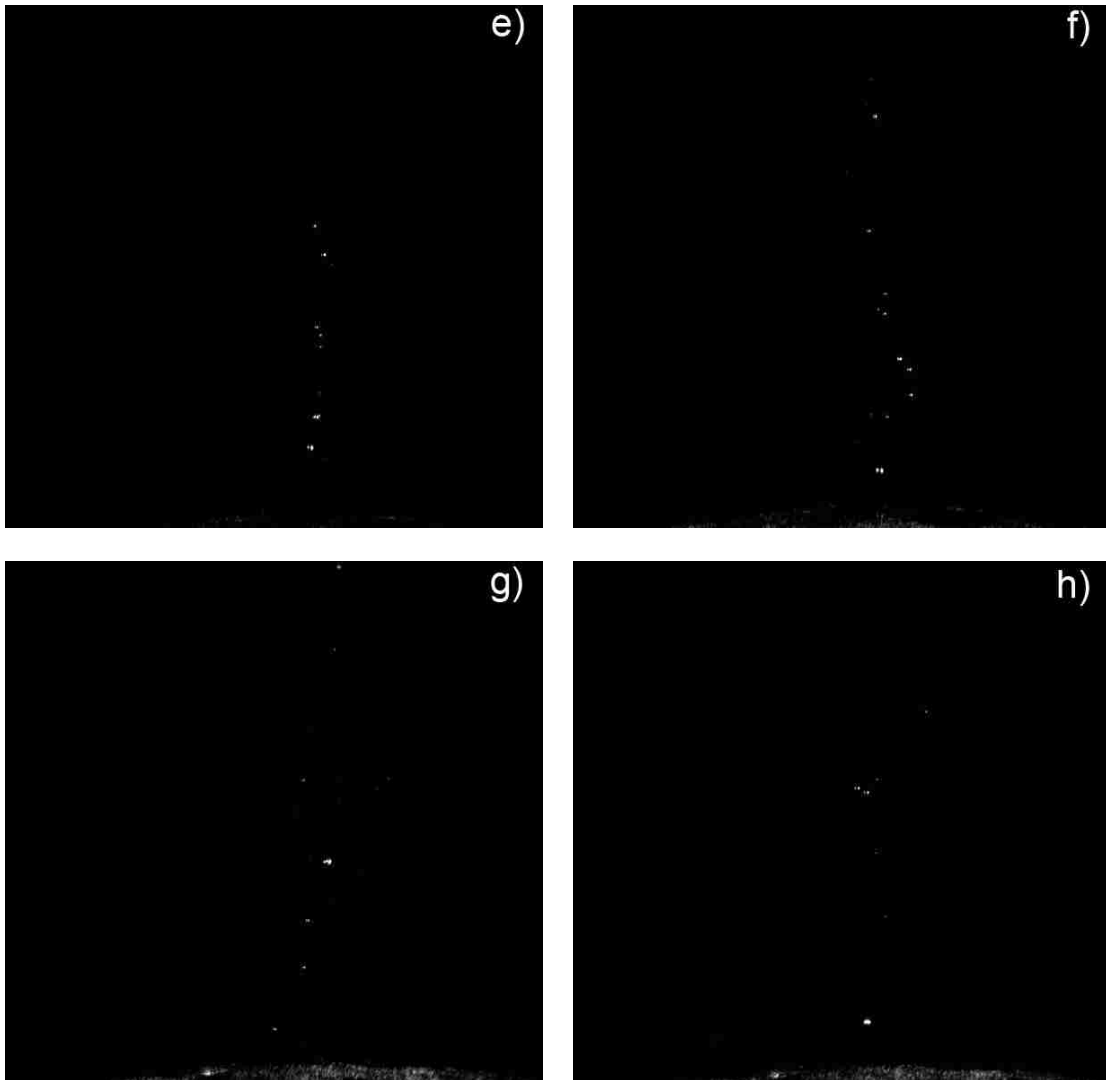
For plume propagation times below 1 µs, the position of the expanding front above the

glycerol droplet can be measured from the high-speed photographs. Figure 5-4 shows a plot of

the plume propagation distance as a function of propagation time for wavelengths between 2.8

and 3.5 µm at 100 nm increments. The measurement at 2.94 µm is also included and note that

data could not be obtained at 3.3 µm because the 3000 J/m^2 fluence was below the threshold for

particle formation. Each data point represents measurements from 4 photographs at each

propagation time for all wavelengths. Above 1 µs propagation time, the plume boundary is difficult to measure. The expansion of the plume was fastest at 3.0 µm and corresponded to a velocity of 320 m/s; the expansion velocity was slowest at 3.5 µm at 40 m/s. Plume expansion velocities are indicated in Table 5-1 and it can be seen that wavelengths in the OH stretch region of glycerol between 2.8 and 3.1 µm can be characterized as fast, whereas wavelengths in the CH stretch region resulted in slow plume expansion. The velocities of liquid material ejection ablated by the OPO laser were also measured in Chapter 4 using the second UV laser and the aerodynamic particle sizer. At 2.94 µm, a velocity of 220 m/s was recorded under 2700 J/m^2 in Chapter 4, which is very close to the results (269 m/s at 3000 J/m^2) measured using fast photography imaging.
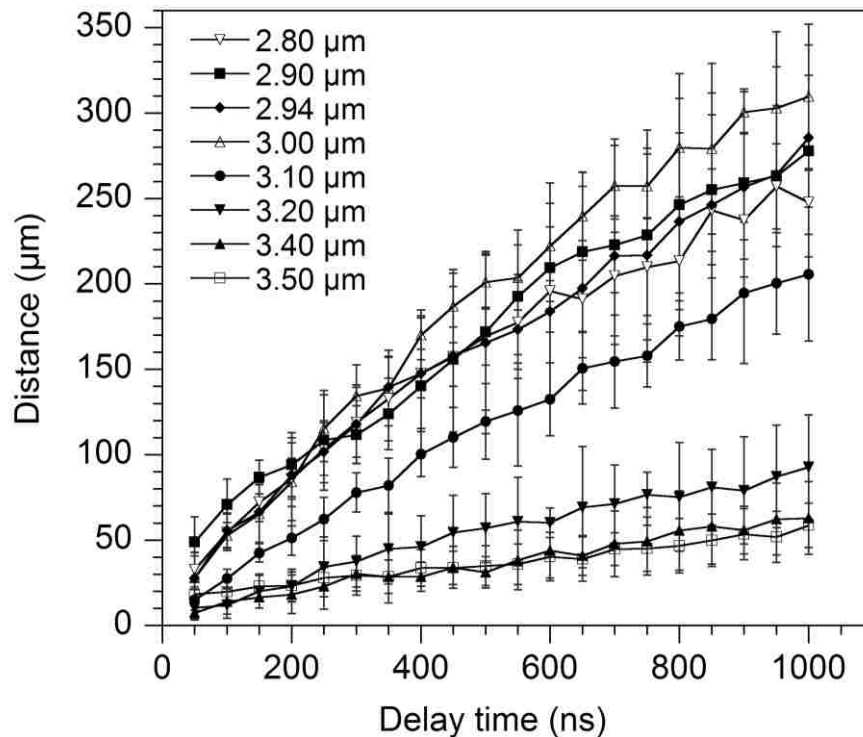

Figure 5-4 Plume front propagation in air at normal direction as a function of delay time at different wavelengths.

Table 5-1 Velocity of plume propagation at mid-IR wavelength range under laser fluence of 3000 J/m^2.

Wavelength (μm)		2.8	2.9	2.94	3.0	3.1	3.2	3.4	3.5
Velocity (m/s)	0-500 ns	286±7	301±13	337±15	384±9	237±6	109±6	59±4	39±2
	500-1000 ns	165±16	169±10	238±8	250±10	180±8	75±6	58±2	40±3
	0-1000 ns	246±7	249±10	269±9	317±9	211±4	92±3	58±2	40±1
A (mm·μs$^{-0.4}$)		14.4	15.4	15.5	17.2	10.7	4.9	3.3	3.2

Evidence of plume deceleration can be found in Figure 5-4; between 2.8 and 3.2, the plume front slowed by about 40% after 500 ns (Table 5-1). Plume deceleration was not observed at 3.4 and 3.5 μm at this fluence, but could be observed at 6000 and 9000 J/m^2.

Figure 5-5 shows plume front propagation as a function of time at different laser fluences at 2.94 (Figure 5-5a) and 3.5 μm (Figure 5-5b). When the laser fluence was increased by a factor of 3, the velocity increased by a factor of 2 at 2.94 μm and a factor of 4 at 3.5 μm. Even at the highest fluence of 9000 J/m^2, the velocity at 3.5 μm was still less than that at 2.94 μm at the lowest (3000 J/m^2) fluence. The velocities are indicated in Table 5-2.

Table 5-2 Velocity of plume propagation at 2.94 and 3.5 μm at a fluence of 6000 and 9000 J/m^2.

	2.94 μm			3.5 μm		
	0-500 ns	500-1000 ns	0-1000 ns	0-500 ns	500-1000 ns	0-1000 ns
6000 J/cm^2	629±23	418±23	537±22	69±1	57±4	66±2
9000 J/cm^2	743±17	462±28	622±24	214±19	166±15	180±7

The threshold fluence for the production of a plume was taken to be the minimum energy necessary to produce an observable signal with the high-speed camera. To measure the threshold

fluence, the time delay was set to 1 μs and the laser energy was adjusted to the value at which

scattered light signal was observed with the camera. A plot of the threshold fluence as a function

of wavelength is shown in Figure 5-6. The threshold fluence was lowest near 2.94 and 3.5 μm,

corresponding to the OH and CH stretch absorption, respectively, as can be seen by comparison

to the FTIR-ATR spectrum of glycerol.[22] Note that there was a small contribution due to water

absorption in the desorption of the 99% purity glycerol.
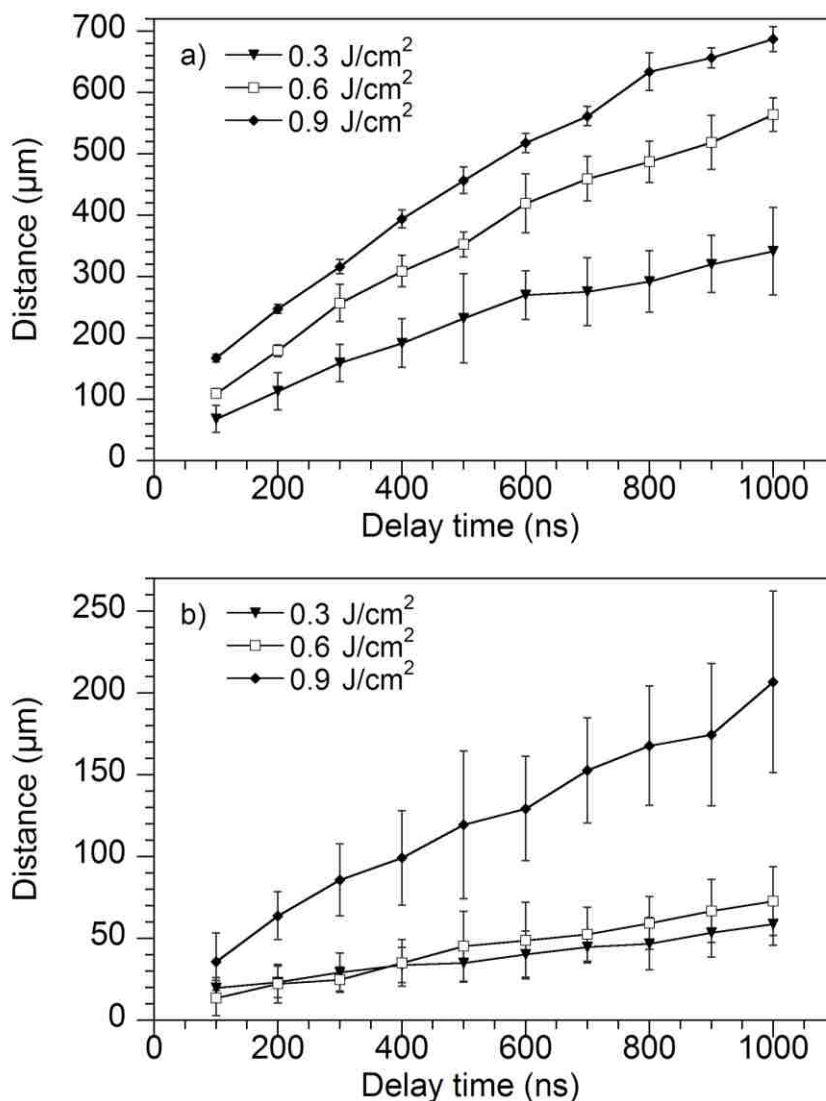
Figure 5-5 Plume front propagation in air at normal direction as a function of delay time at
different laser fluences for a) 2.94 μm and b) 3.5 μm.
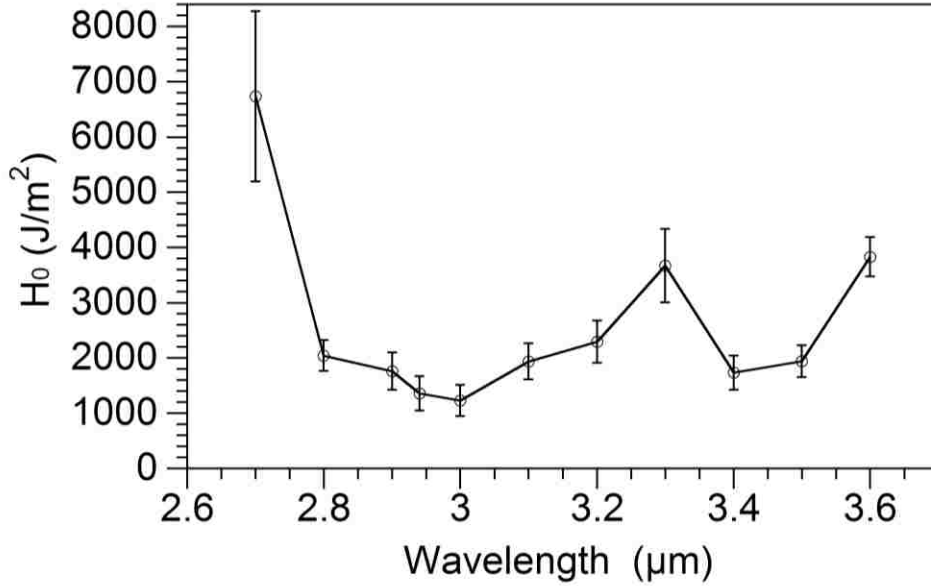
Figure 5-6 Threshold fluence of glycerol ablation at wavelength from 2.7 to 3.6 μm.

5.4. Discussion

The initial propagation of the laser ablation plume can be described by Taylor's shock wave model,[131] which is applicable to the rapid deposition of a finite quantity of energy into a small volume. The spherical shock wave produced under these conditions is described by the expression

$$R = \xi_0 (E_0 / \rho_0)^{1/5} t^{2/5}$$

where R is the distance between the target and the plume front, ξ_0 is a constant that depends on the specific heat of the background gas, ρ_0 is the background gas density, and E_0 is the energy released in the expansion of the plume of ablated material.[132] The plume expansion data was fit to the expression $R = At^{\alpha}$ using the data at 3000 J/m^2 for times up to 25 μs; the result

at 2.94 μm is shown in Figure 5-7a. Similar fits were done for the complete set of wavelengths

and the results are indicated in Table 5-1.

Figure 5-7 Fit of shock wave model (solid line in a and dash line in b) and drag wave model (solid line in b) to the experimental data of front position in plume evolution (symbols in both a and b) at 2.94 μm and 0.3 J/cm^2.

Because the values of ξ_0 and ρ_0 do not change with laser wavelength, the relative values of

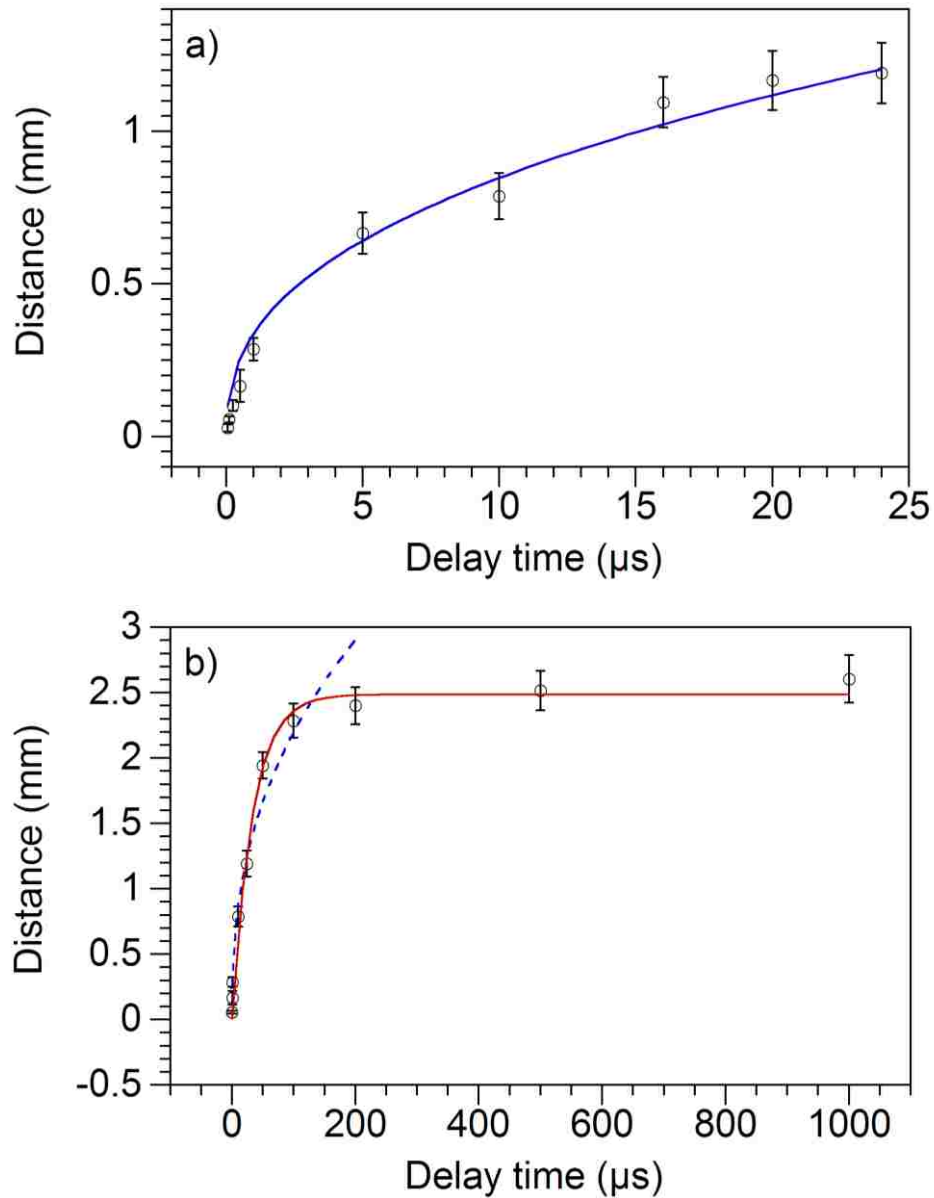the constant A give an indication of the relative values of E_0. It can be seen from the data in

Table 5-1 that the value of A is largest near the absorption maximum of glycerol between 2.8 and 3.1 μm, where the value of A is greater than 10. Near the CH stretch absorption at 3.5 μm, the value of A is between 3 and 5, consistent with a smaller amount of energy released in the expansion at these wavelengths.

These results can be interpreted in terms of the relative contribution of phase explosion to the expansion process. A phase explosion is an explosive boiling process that occurs if the sample is heated rapidly to approximately 90% of the critical temperature.[28, 96, 98-99] Under these conditions, the superheated material can undergo an explosive phase transition that results in volume ejection of the upper layers of the sample. If the glycerol does not reach a temperature that is close to 90% of the critical temperature, there will be no phase explosion and the removal of material will be dominated by surface evaporation rather than the volume removal process of phase explosion.[28, 133] The temperature rise of the glycerol as a function of wavelength can be estimated from

$$\Delta T = \frac{E}{V} \frac{1}{c_v \rho}$$

Where E is the energy absorbed by the glycerol in a volume V, c_v and ρ are the heat capacity and density of glycerol.[74, 125] The energy absorbed per unit volume can be obtained from

$$\frac{E}{V} = 2.3(1-R)\varepsilon_n c_n H_0$$

where R is the surface reflectance, ε_n is the molar decadic absorption coefficient, c_n is the molar concentration, H_0 is the laser fluence. At a constant fluence, the temperature rise is influenced

most strongly by the IR absorption of the glycerol. The molar decadic absorption of glycerol has been determined to 210 L/mol cm at 2.94 μm and 58 L/mol cm at 3.4 μm.[102] Substituting into the above equations, it is found that the temperature rise at 2.94 μm is 585 K for a predicted maximum temperature of 860 K. The critical temperature of glycerol is 765 K, indicating that a phase explosion is likely at this wavelength.[90] The temperature rise at 3.4 μm is only 161 K, for a final temperature of 434 K, suggesting that phase explosion was not occurring at this wavelength.

The shock wave model fits the early expansion stages (less than 100 μs here) of plume propagation. At later stages, the velocity of the plume expansion slows due to the snow plow effect in which the ejected material collides with ambient gas molecules and slows, eventually stopping when the plume pressure equals that of the ambient gas. On these longer time scales, the plume can be described by a drag model through

$$R = R_0[1 - \exp(-\beta t)]$$

where R_0 is the stopping distance and β is the slowing coefficient.[105, 132] The stopping distance can be expressed $R_0 = v_0/\beta$. Where v_0 is the initial plume velocity. A plot of the data at 2.94 μm and 3000 J/m^2 for times up to 1 ms is shown in Figure 8b along with a fit to the drag model. The drag model shows a good agreement with the experimental values as indicated by the solid line in Figure 5-7 (the dashed line indicates the shock wave model fit). The stopping distance indicated by the fit is 2.5 mm. Similar fits at 2.8 and 3.1 μm gave stopping distances of 2.2 and

2.0 mm respectively. It was not possible to obtain good fits to the experimental results at longer wavelengths due to the lack of a defined plume boundary in the photographs.

The time of the expansion greater than 1 μs also shows the effects of the internal shock wave and recoil induced material ejection.[28] Because the internal shock wave is dependent on the effects of phase explosion, it is a strong function of the wavelength. However, in addition to phase explosion the different wavelengths can affect stress and thermal confinement, which depends on the rate of energy deposition in the material.[22] Thermal confinement is achieved when heat is added to the system faster than it is removed by thermal diffusion, whereas stress confinement occurs when the laser adds energy to the system faster than it can be removed through pressure waves (limited by the speed of sound in the material).[98] In recent studies, the conditions for thermal confinement were met for all cases of mid-IR laser ablation of glycerol.[124] For stress confinement, the characteristic time for energy dissipation can be calculated from

$$\tau_{ac} = \frac{1}{\alpha v}$$

where v is the speed of sound in glycerol and α is the absorption coefficient. From the absorption coefficient values and the speed of sound in glycerol,[90, 102] the time for acoustic energy dissipation was found to be 1 ns at 2.94 μm, 4 ns at 3.2 μm, and 8 ns at 3.5 μm. Because the pulse width of OPO is 5 ns, this suggests that stress confinement conditions are met in the OH stretch region, but may not be met in the CH stretch region near 3.5 μm.[124] Comparing the plume expansion at 2.94 (Figure 5-1) and 3.5 μm (Figure 5-3), it can be seen that long time scale

internal shock wave induced material expulsion is much weaker at 3.5 μm compared to 2.94 μm. Thus it appears that both the short and long time plume dynamics is strongly dependent on the laser wavelength.

5.5. Summary

The ablation of glycerol by a wavelength tunable mid-IR source was observed using fast photography in the wavelength range from 2.8 to 3.6 μm at laser fluences between 3000 and 9000 J/m^2. The ablation plume displayed a strong dependence on wavelength and the greatest material removal and longest duration was observed when the laser was tuned to the OH stretch absorption of glycerol at 3.0 μm. At wavelengths off of the OH absorption and near the CH stretch absorption near 3.4 μm, the laser ablated much less material at a given fluence and the duration of the plume was significantly lower. Plume modeling calculations suggest that the vigorous ablation is driven by a phase explosion in the stress confinement regime that leads to the rapid ejection of material in both the early stages of the plume expansion as well as shock wave recoil in the later stages.

CHAPTER 6. CONCLUSIONS AND FUTURE DIRECTIONS

In this dissertation, the physical process of infrared laser desorption and ablation followed by plume evolution was described. This research contributes to the fundamental understanding infrared laser desorption and ionization, and compares the size and relative abundance of particles to the efficiency of laser ionization. A light scattering particle sizer was used to perform particle counting and sizing of ablated materials at difference wavelengths. Post ablation particle irradiation was developed to measure the particle concentration and size as a function of the time delay. The time-resolved ablation plume imaging was accomplished using a fast camera to understand the temporal behavior of ablated plume. These experimental results can be used in the development of IR laser ambient ionization mass spectrometry where the ability to control material removal is critical to efficient ionization. Specifically, these results show that the wavelength and energy of the IR laser can be used to effectively "tune" the composition of the desorption plume. This ability to control the composition of the plume will allow the optimization of mass spectrometry based on laser desorption under ambient conditions.

The concentration and size distribution of particles ablated from deposits of glycerol using a tunable IR laser operated at wavelengths between 2.6 and 3.8 μm were measured in Chapter 3. It was found that the material removal was strongly dependent on the wavelength of IR laser. These results showed the effects of the resonant ablation at 3.0 μm at the OH stretch and 3.5 μm at the CH stretch absorption of glycerol. The number of ablated particles was greater at the same

fluence with resonant absorption. The mean particle size was lowest on resonant excitation compared to off resonant. The threshold fluence for particle formation was lower at wavelengths of resonant absorption and increased as the laser tuned off of the stretch absorption resonance. It was found that the ablation of glycerol with the tunable IR laser could be accomplished in the thermal and stress confinement regimes with the degree of stress confinement determined by the wavelength. At the peak of the OH stretch absorption, the system was in the regime of stress confinement, but moved away from that regime as the wavelength moved away from the IR absorption maxima.

In another work, it was demonstrated that the particle size distribution could be manipulated after desorption and ablation by irradiating the plume of expanding material with a second laser. This two-laser approach to IR laser ablation with UV irradiation of the plume was described in Chapter 4. In this work, particles were ablated from nitrobenzyl alcohol (NBA) with the IR laser tuned to the 2.94 µm OH stretch absorption. After an adjustable delay, the plume was irradiated by a 351 nm UV laser. NBA was used here because it has a strong absorption in the UV. Particles were broken up which changed the size distribution and concentration this was measured as a function of the time delay. The particle concentration increased by nearly an order of magnitude while the particle diameter decreased by one-third to one-half due to the UV irradiation. The timing delay enabled a plume velocity measurement and it was found that at a higher IR fluence, ejected particles were moving faster: 130 m/s at 1600 J/m^2 to 220 m/s at

2700 J/m^2. Particle emission dynamics was consistent with rapid phase transition and plume expansion, followed by an extended emission of particles ablated from the target surface. The ejection of material occurred up to several milliseconds after the IR laser was fired at the sample.

The UV laser break-up of IR ablated particles has important implications analytical applications and in understanding the mechanism of pulsed laser material removal. For example, the performance of laser ablation inductively coupled plasma mass spectrometry and atomic emission spectroscopy is strongly dependent on the size and composition of the ablated material.[122, 134] The addition of a post ablation particle break-up laser opens up the possibility of additional processing the ablated material and potentially improving analytical performance. The technique of IR-MALDESI may also benefit from the use of a post-ablation processing laser.[8, 26, 135] Unfortunately, the long duration of the ablation plume is not ideally suited to a nanosecond pulsed laser due to its millisecond duration: much of the plume material cannot be irradiated with a single pulse. From a mechanistic standpoint, the ability to probe the plume of ablated material in size and composition is an important tool for understanding laser material removal. Although this process can be observed using high-speed photography techniques,[27] these are not always sensitive to small particles at a low number density.

A more direct investigation method, plume imaging, was used to examine the material ablation process and the temporal behavior. As described in Chapter 5, plume evolution of ablated glycerol was recorded using fast photography at IR wavelengths between 2.7 and 3.6 μm,

which covered the OH and CH stretch absorption region of glycerol. As revealed in Chapter 3, the ablation plume has a strong dependence on wavelength, and the photography results revealed that the greatest material removal and longest duration of emission occurs when the laser was tuned to the OH stretch. The several milliseconds of plume evolution echoes the results of Chapter 4. The velocity of the expanding plume was found to be 300 m/s near the 3.0 μm OH stretch absorption, close to the result recorded at similar fluence in Chapter 4. Plume modeling calculations suggest that the vigorous ablation is driven by phase explosion in the stress confinement regime, leading to the rapid ejection of material in both the early stages of the plume expansion as well as shock wave recoil in the later stages.

Future research directions will focus on plume modeling and simulations using finite element method (FEM), a procedure for obtaining solutions to partial differential equations by dividing the system into small but finite elements.[136] The FEM simulations can provide a basic framework for understanding how the laser desorption and ablation processes change with different parameters such as laser energy, wavelength, pulse width, and material properties. Laser-initiated processes can be modeled in two or three dimensions on a micrometer length scale and microsecond time scale. [137-138] Ongoing studies are focused on the early time evolution of the IR laser ablation plume of glycerol. These simulations will be compared to the results of fast plume photography and particle sizing and counting experiments.[139]

REFERENCES

1.   Mao, X.; Russo, R. E., Optimization and calibration of laser ablation inductively coupled plasma atomic emission spectrometry by measuring vertical spatial intensity profiles. *J. Anal. Atom. Spectrom.* 1997, 12, 177-182.

2.   Russo, R. E.; Mao, X.; Liu, H.; Gonzalez, J.; Mao, S. S., Laser ablation in analytical chemistry - a review. *Talanta* 2002, 57, 425-451.

3.   Tanaka, K.; Waki, H.; Ido, Y.; Akita, S.; Yoshida, Y.; Yoshida, T., Protein and polymer analyses up to m/z 100 000 by laser ionization time-of-flight mass spectrometry. *Rapid Commun. Mass Spectrom.* 1988, 2, 151-153.

4.   Hillenkamp, F.; Karas, M.; Beavis, R. C.; Chait, B. T., Matrix-assisted laser desorption ionization mass spectrometry of biopolymers. *Anal. Chem.* 1991, 63, 1193A-1203A.

5.   Daniel, J. M.; Laiko, V. V.; Doroshenko, V. M.; Zenobi, R., Interfacing liquid chromatography with atmospheric pressure MALDI-MS. *Anal. Bioanal. Chem.* 2005, 383, 895-902.

6.   Shiea, J.; Huang, M. Z.; Hsu, H. J.; Lee, C. Y.; Yuan, C. H.; Beech, I.; Sunner, J., Electrospray-assisted laser desorption/ionization mass spectrometry for direct ambient analysis of solids. *Rapid Commun. Mass Spectrom.* 2005, 19, 3701-3704.

7.   Sampson, J. S.; Hawkridge, A. M.; Muddiman, D. C., Generation and detection of multiply-charged peptides and proteins by matrix-assisted laser desorption electrospray ionization (MALDESI) fourier transform ion cyclotron resonance mass spectrometry. *J. Am. Soc. Mass Spectrom.* 2006, 17, 1712–1716.

8.   Rezenom, Y. H.; Dong, J.; Murray, K. K., Infrared laser-assisted electrospray ionization mass spectrometry. *Analyst* 2008, 133, 226–232.

9.   Karas, M.; Hillenkamp, F. H., Laser desorption ionization of proteins with molecular masses exceeding 10000 daltons. *Anal. Chem.* 1988, 60, 2229-2301.

10. Fenn, J. B.; Mann, M.; Meng, C. K.; Wong, S. F.; Whitehouse, C. M., Electrospray ionization for mass spectrometry of large biomolecules. *Science* 1989, 246, 64-71.

11. Knochenmuss, R.; Zenobi, R., MALDI ionization: the role of in-plume processes. *Chem. Rev.* 2003, 103, 441-452.

12. Karas, M.; Kruger, R., Ion formation in MALDI: the cluster ionization mechanism. *Chem. Rev.* 2003, 103, 427-439.

13. Dreisewerd, K., The desorption process in MALDI. *Chem. Rev.* 2003, 103, 395-425.

14. Dreisewerd, K.; Berkenkamp, S.; Leisner, A.; Rohlfing, A.; Menzel, C., Fundamentals of matrix-assisted laser desorption/ionization mass spectrometry with pulsed infrared lasers. *Int. J. Mass Spectrom.* 2003, 226, 189-209.

15. Vertes, A., Soft Laser Desorption Ionization - MALDI, DIOS, and Nanostructures. In *Laser Ablation and Its Applications*, Phipps, C. R., Ed. Springer: New York, 2007; pp 505-528.

16. Sampson, J. S. Development and Characterization of an Atmospheric Pressure Ionization Source Matrix-Assisted Laser Desorption Electrospray Ionization Coupled to Fourier Transform Ion Cyclotron Resonance Mass Spectrometry for Analysis of Biological Macromolecules Ph.D Dissertation, North Carolina State University, Raleigh, 2009.

17. Rezenom, Y. H.; Dong, J. N.; Murray, K. K., Infrared laser-assisted desorption electrospray ionization mass spectrometry. *Analyst* 2008, 133, 226 - 232.

18. Sampson, J. S.; Murray, K. K.; Muddiman, D. C., Intact and top-down characterization of biomolecules and direct analysis using infrared matrix-assisted laser desorption electrospray ionization coupled to FT-ICR mass spectrometry. *J. Am. Soc. Mass Spectrom.* 2009, 20, 667-673.

19. Dong, J. Merged Electrospray Ionization Mass Spectrometry. Ph.D. Dissertation, Louisiana State University, Baton Rouge, 2009.

20. Alves, S.; Kalberer, M.; Zenobi, R., Direct detection of particles formed by laser ablation of matrices during matrix-assisted laser desorption/ionization. *Rapid Commun. Mass Spectrom.* 2003, 17, 2034–2038.

21. Jackson, S. N.; Mishra, S.; Murray, K. K., Characterization of coarse particles formed by laser ablation of MALDI matrixes. *J. Phys. Chem. B* 2003, 107, 13106–13110.

22. Jackson, S. N.; Kim, J. K.; Laboy, J. L.; Murray, K. K., Particle formation by infrared laser ablation of glycerol: implications for ion formation. *Rapid Commun. Mass Spectrom.* 2006, 20, 1299-1304.

23. Zhigilei, L. V.; Kodali, P. B. S.; Garrison, B. J., Molecular dynamics model for laser ablation and desorption of organic solids. *J. Phys. Chem. B* 1997, 101, 2028-2037.

24. Handschuh, M.; Nettesheim, S.; Zenobi, R., Laser-induced molecular desorption and particle ejection from organic films. *Appl. Surf. Sci.* 1999, 137, 125–135.

25. Jackson, S. N., Laser Desorption Mass Spectrometry of Bioaerosols. In *Chemistry*, Emory University: Atlanta, 2003; Vol. PhD.

26. Dong, J.; Rezenom, Y. H.; Murray, K. K., Desorption electrospray ionization of aerosol particles. *Rapid Commun. Mass Spectrom.* 2007, 21, 3995–4000.

27. Leisner, A.; Rohlfing, A.; Rohling, U.; Dreisewerd, K.; Hillenkamp, F., Time-resolved imaging of the plume dynamics in infrared matrix-assisted laser desorption/ionization with a glycerol matrix. *J. Phys. Chem. B* 2005, 109, 11661–11666.

28. Apitz, I.; Vogel, A., Material ejection in nanosecond Er:YAG laser ablation of water, liver, and skin. *Appl. Phys. A* 2005, 81, 329-338.

29. Ludemann, H. C.; Redmond, R. W.; Hillenkamp, F., Singlet-singlet annihilation in ultraviolet matrix-assisted laser desorption/ionization studied by fluorescence spectroscopy *Rapid Commun. Mass Spectrom.* 2002, 16, 1287-1294.

30. Ehring, H.; Sundqvist, B. U. R., Studies of the MALDI process by luminescence spectroscopy. *J. Mass Spectrom.* 1995, 30, 1303-1310.

31. Krüger, R.; Pfenninger, A.; Fournier, I.; Glückmann, M.; Karas, M., Analyte incorporation and ionization in matrix-assisted laser desorption/ionization visualized by pH indicator molecular probes. *Anal. Chem.* 2001, 73, 5812-5821.

32. Richard, K., Ion formation mechanisms in UV-MALDI. *Analyst* 2006, 131, 966-986.

33. Frankevich, V. E.; Zhang, J.; Friess, S. D.; Dashtiev, M.; Zenobi, R., Role of electrons in laser desorption/ionization mass spectrometry. *Anal. Chem.* 2003, 75, 6063-6067.

34. Vestal, M. L., Methods of ion generation. *Chem. Rev.* 2001, 101, 361-375.

35. Silverstein, R. M.; Bassler, G. C., Spectrometric identification of organic compounds. *J. Chem. Educ.* 1962, 39, 546-553.

36. Baldwin, M. A., Mass spectrometers for the analysis of biomolecules. *Methods Enzymol.* 2005, 402, 3-48.

37. Hoffmann, E. d.; Stroobant, V., *Mass Spectrometry: Principles and Applications (2nd ed.)*. John Wiley and Sons: 2001.

38. Cody, R. B.; Tamura, J.; Musselman, B. D., Electrospray ionization/magnetic sector mass spectrometry: calibration, resolution, and accurate mass measurements. *Anal. Chem.* 1992, 64, 1561-1570.

39. Date, A. R.; Gray, A. L., Plasma source mass spectrometry using an inductively coupled plasma and a high resolution quadrupole mass filter. *Analyst* 1981, 106, 1255-1267.

40. Moyer, S. C.; Cotter, R. J., Peer reviewed: atmospheric pressure MALDI, a new method for proteomics and other biological studies requiring high-throughput analyses. *Anal. Chem.* 2002, 74, 468A-476A.

41. Hoffmann, E., Tandem mass spectrometry: a primer. *J. Mass Spectrom.* 1996, 31, 129-137.

42. Allen, J. S., An improved electron multiplier particle counter. *Rev. Sci. Instru.* 1947, 18, 739-749.

43. Marshall, A. G.; Hendrickson, C. L.; Jackson, G. S., Fourier transform ion cyclotron resonance mass spectrometry: a primer. *Mass Spectrom Rev* 1998, 17, 1-35.

44. Hu, Q.; Noll, R. J.; Li, H.; Makarov, A.; Hardman, M.; Cooks, R. G., The orbitrap: a new mass spectrometer. *J. Mass Spectrom.* 2005, 40, 430-443.

45. Dempster, A., Positive ray analysis of lithium and magnesium. *J. Phys. Rev.* 1921, 18, 415-422.

46. Ashcroft, A. E., *Ionization Methods in Organic Mass Spectrometry*. The Royal Society of Chemistry: Cambridge, 1997.

47. Inghram, M. G.; Hayden, R. J., *Mass spectroscopy*. National Academy of Sciences: Washington D.C., 1954.

48. Harrison, W. W.; Barshick, C. M.; Kiingier, J. A.; Rall, P. H.; Mei, Y., Glow discharge techniques in analytical chemistry. *Anal. Chem.* 1990, 62, 943A-949A.

49. Chapman, B., *Glow Discharge Processes* Wiley: New York, 1980.

50. Kuhn, H. R. Laser Ablation ICP-MS: Fundamental Investigations on Aerosols Generated by Laser Ablation at Ambient Pressure. Ph.D. Dissertation, ETH, Zürich 2005.

51. Munson, B.; Field, F. H., Chemical ionization mass spectrometry. I. General introduction. *J. Am. Chem. Soc.* 1966, 88, 2621-2630.

52. Dass, C., *Principles and Practice of Biological Mass Spectrometry*. Wiley-Interscience: New York, 2000.

53. Ghaderi, S.; Kulkarni, P. S.; Ledford, E. B.; Wilkins, C. L.; Gross, M. L., Chemical ionization in Fourier transform mass spectrometry. *Anal. Chem.* 1981, 53, 428-437.

54. Hunt, D. F.; Sethi, S. K., Gas-phase ion/molecule isotope-exchange reactions: methodology for counting hydrogen atoms in specific organic structural environments by chemical ionization mass spectrometry. *J. Am. Chem. Soc.* 1980, 102, 6953-6963.

55. Herman, J. A.; Harrison, A. G., Effect of reaction exothermicity on the proton transfer chemical ionization mass spectra of isomeric C_5 and C_6 alkanols. *Can. J. Chem.* 1981, 59, 2125-2132.

56. Gross, J., *Mass Spectrometry - A Textbook*. Springer: New York, 2004.

57. Morris, H.; Panico, M.; Barber, M.; Bordoli, R. S., RD; Tyler, A., Fast atom bombardment: a new mass spectrometric method for peptide sequence analysis. *Biochem. Biophys. Res. Commun.* 1981, 101, 623-631.

58. Busch, K. L., Desorption ionization mass spectrometry. *J. Mass Spectrom.* 1995, 30, 233-240.

59. Zaikin, V.; Halket, J., Derivatization in mass spectrometry -- 8. soft ionization mass spectrometry of small molecules. *Euro. J. Mass Spectrom.* 2006, 12, 79-115.

60. Green, B. N., A comparison of mass spectrometric methods for the analysis of protein mixtures. *Biochem. J.* 1992, 284, 603-604.

61. Schindler, P. A.; Dorsselaer, A. V.; Falick, A. M., Analysis of hydrophobic proteins and peptides by electrospray ionization mass spectrometry. *Anal. Biochem.* 1993, 213, 256-263.

62. Li, K. Y.; Tu, H. H.; Ray, A. K., Charge limits on droplets during evaporation. *Langmuir* 2005, 21, 3786-3794.

63. Hiff, E. R.; Kammer, F.; Wien, K., *PDMS and Clusters*. Springer-Verlag: New York, 1986.

64. Chapman, J. R., *Practical Organic Mass Spectrometry: A Guide for Chemical and Biochemical Analysis, 2nd Edition*. John Wiley & Sons Ltd: New York, 1995.

65. Van, V. L.; Adriaens, A.; Gijbels, R., Static secondary ion mass spectrometry (S-SIMS) Part 1: methodology and structural interpretation. *Mass Spectrom. Rev.* 1999, 18, 1-47.

66. Benninghoven, A.; Rüdenauer, F. G.; Werner, H. W., *Secondary Ion Mass Spectrometry: Basic Concepts, Instrumental Aspects, Applications, and Trends*. Wiley,: New York, 1987.

67. Sunner, J., Ionization in liquid secondary ion mass spectrometry (LSIMS). *Org. Mass Spectrom.* 1993, 28, 805-823.

68. Hillenkamp, F.; Peter-Katalinic, J., *MALDI MS: A Practical Guide to Instrumentation, Methods and Applications*. Wiley-VCH: Weinheim, 2007.

69. Itoh, N.; Stoneham, A. M., *Materials Processing by Electronic Excitation*. Oxford University Press: Oxford, 2001.

70. Murray, K. K., Infrared Matrix-Assisted Laser Desorption Ionization. In *The Encyclopedia of Mass Spectrometry: Volume 6: Ionization Methods* Caprioli, R. M.; Gross, M. L., Eds. Elsevier: New York, 2006; pp 701-705.

71. Overberg, A.; Karas, M.; Bahr, U.; Kaufmann, R.; Hillenkamp, F., Matrix-assisted infraredlaser (2.94 mm) desorption/ionization mass spectrometry of large biomolecules. *Rapid Commun. Mass Spectrom.* 1990, 4, 293-296.

72. Sadeghi, M.; Olumee, Z.; Tang, X.; Vertes, A.; Jiang, Z. X.; Henderson, A. J.; Lee, H. S.; Doroshenko, V. M.; Prasad, C. R., Compact tunable Cr:LiSAF laser for infrared matrix-assisted laser desorption/ionization. *Rapid Commun. Mass Spectrom.* 1997, 11, 393-397.

73. Caldwell, K. L.; McGarity, D. R.; Murray, K. K., Matrix-assisted laser desorption/ionization with a tunable mid-infrared optical parametric oscillator. *J. Mass Spectrom.* 1997, 32, 1374-1377.

74. Fan, X.; Murray, K. K., UV laser irradiation of IR laser generated particles ablated from nitrobenzyl alcohol. *Appl. Surf. Sci.* 2009, 255, 6297-6302.

75. Wang, B. H.; Dreisewerd, K.; Bahr, U.; Karas, M.; Hillenkamp, F., Gas-phase cationization and protonation of neutrals generated by matrix-assisted laser desorption *J. Am. Soc. Mass Spectrom.* 1993, 4, 393-398.

76. Ehring, H.; Karas, M.; Hillenkamp, F., Role of photoionization and photochemistry in ionization processes of organic molecules and relevance for matrix-assisted laser desorption ionization mass spectrometry. *Org. Mass Spectrom.* 1992, 27, 472-480.

77. Cooks, R. G.; Ouyang, Z.; Takats, Z.; Wiseman, J. M., Ambient Mass Spectrometry. *Science* 2006, 311, (5767), 1566-1570.

78. Huang, M. Z.; Yuan, C. H.; Cheng, S. C.; Cho, Y. T.; Shiea, J., Ambient ionization mass spectrometry. *Ann. Rev. Anal. Chem.* 2010, 3, 43-65.

79. Venter, A.; Nefliu, M.; Cooks, R. G., Ambient desorption ionization mass spectrometry. *Trends Anal. Chem.* 2008, 27, 284-290.

80. Takáts, Z.; Wiseman, J. M.; Gologan, B.; Cooks, R. G., Mass spectrometry sampling under ambient conditions with desorption electrospray ionization. *Science* 2004, 306, 471-473.

81. Takáts, Z.; Wiseman, J.; Cooks, R., Ambient mass spectrometry using desorption electrospray ionization (DESI): instrumentation, mechanisms and applications in forensics, chemistry, and biology. *J. of mass spectrom.* 2005, 40, 1261–1275.

82. Cody, R. B.; Laramee, J. A.; Durst, H. D., Versatile new ion source for the analysis of materials in open air under ambient Conditions. *Anal. Chem.* 2005, 77, (8), 2297-2302.

83. Penning, F. M., Ionization by metastable atoms. *Naturwissenschaften* 1927, 15, 818.

84. Zalusec, E. J.; Gage, D. A.; J. T. Watson, Matrix-assisted laser desorption ionization mass spectrometry: applications in peptide and protein characterization. *Prot. Expres. Purific.* 1995, 6, 109-123.

85. Fitzgerald, M. C.; Smith, M., Mass spectrometry of nucleic acids: the promise of matrix-assisted laser desorption-ionization (MALDI) mass spectrometry. *Ann. Rev. Biophys. Biomole. Struc.* 1995, 24, 117-140.

86. Ding, L.; Sudakov, M.; Brancia, F. L.; Giles, R.; Kumashiro, S., A digital ion trap mass spectrometer coupled with atmospheric pressure ion sources,. *J. Mass Spectrom.* 2004, 39, 471-484.

87. Zhigilei, L. V.; Leveugle, E.; Garrison, B. J.; Yingling, Y. G.; Zeifman, M. I., Computer simulation of laser ablation of molecular substrates. *Chem. Rev.* 2003, 103, 321-347.

88. Karas, M.; Bachmann, D.; Hillenkamp, F., Influence of the wavelength in high-irradiance ultraviolet laser desorption mass spectrometry of organic molecules. *Anal. Chem.* 1985, 57, 2935-2935.

89. Zhigilei, L. V.; Garrison, B. J., Mechanisms of laser ablation from molecular dynamics simulations: dependence on the initial temperature and pulse duration. *Appl. Phys. A* 1999, 69, S75-S80.

90. Rohlfing, A.; Menzel, C.; Kukreja, L. M.; Hillenkamp, F.; Dreisewerd, K., Photoacoustic analysis of matrix-assisted laser desorption/ionization processes with pulsed infrared lasers. *J. Phys. Chem. B* 2003, 107, 12275-12286.

91. Zhigilei, L. V.; Garrison, B. J., Molecular dynamics simulation study of the fluence dependence of particle yield and plume composition in laser desorption and ablation of organic solids. *Appl. Phys. Lett.* 1999, 74, 1341-1343.

92. Song, K. H.; Xu, X., Explosive phase transformation in excimer laser ablation. *Appl. Surf. Sci.* 1998, 127, 111-116.

93. Kodali, P. B. S.; Zhigilei, L. V.; Garrison, B. J., Phase transition at low fluences in laser desorption of organic solids: a molecular dynamics study. *Nucl. Instrum. Methods Phys. Research B* 1999, 153, 167-171.

94. Martynyuk, M. M., Mechanism for metal damage by intense electromagnetic radiation. *Sov. Phys. Tech. Phys.* 1976, 21, 430-433.

95. Kelly, R.; Miotello, A., Does normal boiling exist due to laser-pulse or ion bombardment? *J. Appl. Phys.* 2000, 87, 3177-3179.

96. Miotello, A.; Kelly, R., Laser-induced phase explosion: new physical problems when a condensed phase approaches the thermodynamic critical temperature *Appl. Phys. A* 1999, 69, S67-S73.

97. Zhigilei, L. V.; Yingling, Y. G.; Itina, T. E.; Schoolcraft, T. A.; Garrison, B., MD simulations of MALDI desorption - connections to experiment. *Int. J. Mass Spectrom.* 2003, 226, 85-106.

98. Zhigilei, L. V.; Garrison, B. J., Microscopic mechanisms of laser ablation of organic solids in the thermal and stress confinement irradiation regimes. *J. Appl. Phys.* 2000, 88, 1281-1298.

99. Vogel, A.; Venugopalan, V., Mechanisms of pulsed laser ablation of biological tissues. *Chem. Rev.* 2003, 103, 577-644.

100. Gonzalez, J.; Mao, X. L.; Roy, J.; Mao, S. S.; Russo, R. E., Comparison of 193, 213 and 266 nm laser ablation ICP-MS. *J. Anal. At. Spectrom.* 2002, 17, 1108-1113.

101. Laboy, J. L.; Murray, K. K., Characterization of infrared matrix-assisted laser desorption ionization samples by fourier transform infrared attenuated total reflection spectroscopy. *Appl. Spectrosc.* 2004, 58, 451-456.

102. Menzel, C.; Dreisewerd, K.; Berkenkamp, S.; Hillenkamp, F., Mechanisms of energy deposition in infrared matrix-assisted laser desorption/ionization mass spectrometry. *Int. J. Mass Spectrom.* 2001, 207, 73-96.

103. Paltauf, G.; Dyer, P. E., Photomechanical processes and effects in ablation. *Chem. Rev.* 2003, 103, 487–518.

104. Zhigilei, L. V., Dynamics of the plume formation and parameters of the ejected clusters in short-pulse laser ablation. *Appl. Phys. A* 2003, 76, 339-350.

105. Harilal, S. S.; Bindhu, C. V.; Tillack, M. S.; Najmabadi, F.; Gaeris, A. C., Internal structure and expansion dynamics of laser ablation plumes into ambient gases. *J. Appl. Phys.* 2003, 93, 2380-2388.

106. Zhigilei, L. V.; Garrison, B. J., Velocity distributions of analyte molecules in matrix-assisted laser desorption from computer simulations. *Rapid Commun. Mass Spectrom.* 1998, 12, 1273-1277.

107. Zhang, W.; Chait, B. T., Radial velocity distributions of molecular ions produced by matrix-assisted laser desorption/ionization. *Int. J. Mass Spectrom. Ion Processes* 1997, 160, 259-267.

108. Denoyer, E.; Natusch, D. F. S.; Surkyn, P.; Adams, F. C., Laser microprobe mass analysis (LAMMA) as a tool for particle characterization: a study of coal fly ash. *Environ. Sci. Technol.* 1983, 17, 457–462.

109. Verbueken, A. H.; Bruynseels, F. J.; Griekent, R. E. V., Laser microprobe mass analysis: a review of applications in the life sciences *Biom. Mass Spectrom.* 1985, 12, 438-463.

110. Takamizawa, A.; Kajimoto, S.; Hobley, J.; Hatanaka, K.; Ohta, K.; Fukumura, H., Explosive boiling of water after pulsed IR laser heating. *Phys. Chem. Chem. Phys.* 2003, 5, 888-895.

111. Rohlfing, A.; Leisner, A.; Hillenkamp, F.; Dreisewerd, K., Investigation of the desorption process in UV matrix-assisted laser desorption/ionization with a liquid 3-nitrobenzyl alcohol matrix by photoacoustic analysis, fast-flash imaging, and UV laser postionization. *J. Phys. Chem. C* 2010, 114, 5367-5381.

112. Berkenkamp, S.; Menzel, C.; Hillenkamp, F.; Dreisewerd, K., Measurements of mean initial velocities of analyte and matrix ions in infrared matrix-assisted laser desorption ionization mass spectrometry. *J. Am. Soc. Mass Spectrom.* 2002, 13, 209-220.

113. Ermer, E. R.; Baltz-Knorr, M.; Haglund, R. F., Intensity dependence of cation kinetic energies from 2,5-dihydroxybenzoic acid near the infrared matrix-assisted laser desorption/ionization threshold. *J. Mass Spectrom.* 2001, 36, 538-545.

114. Glückmann, M.; Karas, M., The initial ion velocity and its dependence upon matrix, analyte, and preparation method in ultraviolet matrix-assisted laser desorption/ionization. *J. Mass Spectrom.* 1999, 34, 467−477.

115. Duarte, F. J., *Tunable Laser Applications*. 2nd ed.; CRC: New York, 2009.

116. Wright, J. C.; LaBuda, M. J.; Thompson, D.; Lascola, R.; Russel, M., Nonlinear laser spectroscopy. *Anal. Chem.* 1996, 68, 600-607.

117. Birks, J. B., Excimers. *Rep. Prog. Phys.* 1975, 38, 903-974.

118. Basting, D.; Marowsky, G., *Excimer Laser Technology* Springer New York, 2005.

119. Duarte, F. J., *High-power Dye Lasers*. Springer New York, 1992.

120. Leisner, A.; Rohlfing, A.; Berkenkamp, S.; Hillenkamp, F.; Dreisewerd, K., Infrared laser post-ionization of large biomolecules from an IR-MALDI plume. *J. Am. Soc. Mass Spectrom.* 2004, 15, 934-941.

121. Leveugle, E.; Ivanov, D. S.; Zhigilei, L. V., Photomechanical spallation of molecular and metal targets: molecular dynamics study. *Appl. Phys. A* 2004, 79, 1643-1655.

122. Hergenroeder, R., Laser-generated aerosols in laser ablation for inductively coupled plasma spectrometry *Spectrochim. Acta B* 2006, 61B, 284-300.

123.   Liu, C. Y.; Mao, X. L.; Greif, R.; Russo, R. E., Particle-size dependent chemistry from laser ablation of brass. *Anal. Chem.* 2005, 77, 6687-6691.

124.   Fan, X.; Little, M. W.; Murray, K. K., Infrared laser wavelength dependence of particles ablated from glycerol. *Appl. Surf. Sci.* 2008, 255, 1699-1704.

125.   Feldhaus, D.; Menzel, C.; Berkenkamp, S.; Hillenkamp, F.; Dreisewerd, K., Influence of the laser fluence in infrared matrix-assisted laser desorption/ionization with a 2:94 mm Er :YAG laser and a flat-top beam profile. *J. Mass Spectrom.* 2000, 35, 1320-1328.

126.   Papina, T. S.; Pimenova, S. M.; Lukyanova, V. A.; Kolesov, V. P., Standard enthalpies of formation of benzyl alcohol and α,α,α-trichlorotoluene. *Russ. J. Phys. Chem. (Engl. Transl.)* 1995, 69, 1951-1953.

127.   Klincewicz, K. M.; Reid, R. C., Estimation of critical properties with group contribution methods. *AIChE J.* 1984, 30, 137-142.

128.   Huang, F.; Fan, X.; Murray, K. K., Matrix-assisted laser desorption ionization of infrared laser ablated particles. *Int. J. Mass Spectrom.* 2008, 274, 21-24.

129.   Schoolcraft, T. A.; Constable, G. S.; Zhigilei, L. V.; Garrison, B. J., Molecular dynamics simulation of the laser disintegration of aerosols particles. *Anal. Chem.* 2000, 72, 5143-5150.

130.   Chen, X.; Carroll, J. A.; Beavis, R. C., Near-ultraviolet-induced matrix-assisted laser desorption/ionization as a function of wavelength. *J. Am. Soc. Mass Spectrom.* 1998, 9, 885-891.

131.   Taylor, G., The instability of liquid surfaces when accelerated in a direction perpendicular to their planes. I. In *Royal Society of London, Series A, Mathematical and Physical Sciences*, London, 1950; Vol. 201, pp 192-196.

132.   Misra, A.; Thareja, R. K., Investigation of laser ablated plumes using fast photography. *IEEE Trans. Plasma Sci.* 1999, 27, 1553-1558.

133.   Chen, Z. Y.; Vertes, A., Early plume expansion in atmospheric pressure midinfrared laser ablation of water-rich targets. *Phys. Rev. E* 2008, 77, 036316.1-036316.9.

134.   Günther, D.; Hattendorf, B., Solid sample analysis using laser ablation inductively coupled plasma mass spectrometry. *Trends Anal. Chem.* 2005, 24, 255–265.

135.   Nemes, P.; Vertes, A., Laser ablation electrospray ionization for atmospheric pressure, in vivo, and imaging mass spectrometry. *Anal. Chem.* 2007, 79, 8098-8106.

136.   Reddy, J. N., *An Introduction to The Finite Element Method*. 3rd ed.; McGraw-Hill Education: New York, 2005.

137.   Oliveira, V.; Vilar, R., Finite element simulation of pulsed laser ablation of titanium carbide. *Appl. Surf. Sci.* 2007, 253, 7810-7814.

138.   Vila Verde, A.; Ramos, M. M. D., Boundary conditions for 3D dynamic models of ablation of ceramics by pulsed mid-infrared lasers. *Appl. Surf. Sci.* 2005, 247, 354-361.

139.   Huang, F.; Fan, X.; Murray, K. K., Modeling matrix-assisted laser desorption electrospray ionization. In *the 58th ASMS Conference on Mass Spectrometry*, Salt Lake City, UT, 2010.

APPENDIX A. TRIGGER SETUP AND TIMING FOR FAST PHOTOGRAPHY
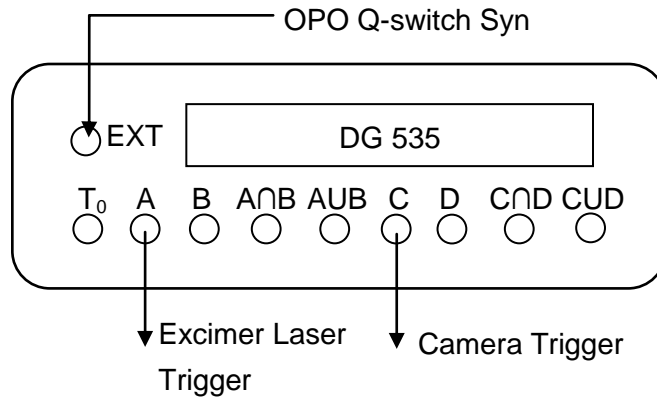
Figure A-1 Schematic of the trigger setup in the experiments of fast photography. All connections are made with 50Ω BNC cables. EXT is input and T_0, A, B, AB, -AB, C, D, CD and -CD are outputs. The time delay between EXT and T_0 is 85 ns. Time delay between T_0 and other outputs can be regulated from 0 to 1000 s with 5 ps resolution. Both external and internal trigger modes can be realized by DG-535 and external trigger was chosen as the trigger mode in the experiments. In external trigger mode, external signals are sent to EXT to trigger the delay generator and single or multiple signals are then generated and transferred to other instruments through outputs on the panel. In the experiments of fast photography, initial trigger signals from Q-switch synch out of OPO system were sent to EXT. This signal is 175 ns ahead of the center of laser pulse (5 ns pulse width). After a certain delay time trigger signals (TTL signal, +5 V) were transferred to the excimer laser from Channel A and to the camera through Channel C. To regulate the delay time between the OPO and excimer laser pulses, decrease or increase the delay of Channel A. The timing diagram for the signals of Channel EXT, T_0, A and C are shown in Figure A-2.
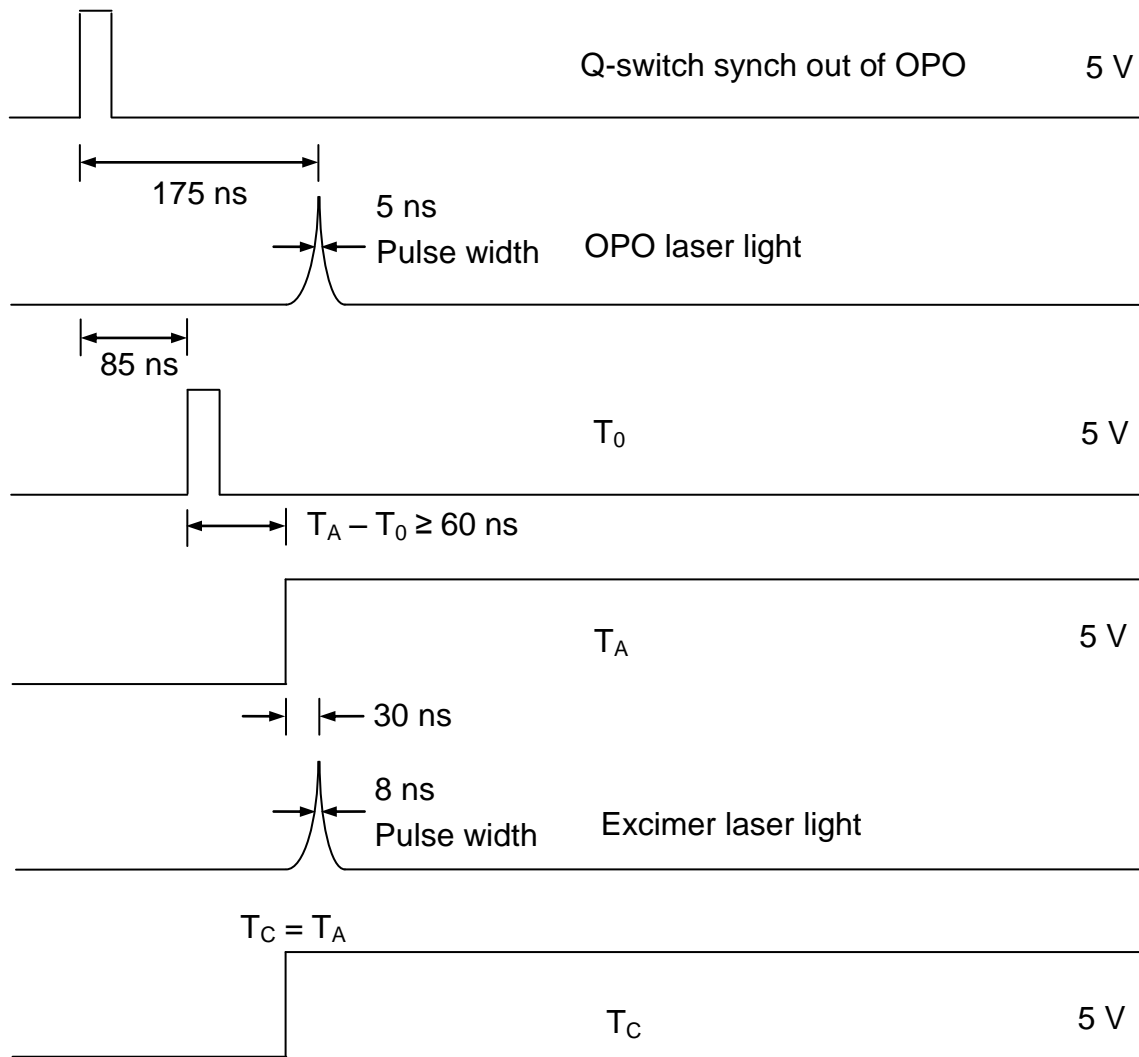
Figure A-2 Timing diagram in fast photography.

APPENDIX B. LABVIEW CAMERA CONTROL PROGRAM

LabView (Laboratory Virtual Instrumentation Engineering Workbench) is a commercial graphical software system provided by National Instruments for developing instrument control, data acquisition, and industrial automation on various platforms including Microsoft Windows and Mac OS X. Windows Vista was the operating system used in this experiment. Virtual instruments (VIs) are the LabView programs consisting of a front panel and a block diagram. The front panel is the user interface, which includes input components such as software knobs and switches and output such as numerical readouts and graphs. The block diagram is a representation of the executable code and consists of icons that represent data processing and virtual wires that represent the transfer of data between them. In this work, the photograph acquisition and processing were controlled by LabView programs. The front panel and block diagrams of the photograph acquisition and processing programs are shown in the figures below.

Loop and Grab Frame-2.vi is the program used to control the pulse generator and CMOS camera, and save photos on a microcomputer. Shown in Figure B-1 is the front panel of Loop and Grab Frame-2.vi and corresponding block diagram is shown in Figure B-2. The "Start Time" on the front panel is the initial time delay between the OPO and excimer laser. The information of time delay was transferred from the microcomputer to the delay generator using the GPIB protocol. The delay generator was triggered by the OPO laser. After the initial time delay, the delay generator triggered the excimer laser and the camera. The camera was connected to the

computer by a Firewire (IEEE 1394 interface) cable, which is frequently used for high-speed

communications and isochronous real-time data transfer. A photo was taken by the camera at the

initial time delay and saved on the computer at the selected "File Path" with the selected "File

Name", which was named by the user in advance on the front panel. The "Time Increment" on

the front panel is automatically added to the time delay after saving the first photo. The

procedure of photo shooting and saving is repeated at the new delay time and a second photo is

saved. The time delay increased continuously until the delay time was equal to or greater than

the "End Time" on the front panel. The "Cycles" on the front panel is the number of repetitions

for the scan of delay times.

Frame Grab.vi shown in Figure B-3 is the sub VI of Loop and Grab Frame-2.vi used for a

single photo shooting and saving at a selected file path. Frame Grab.vi includes IMAQdx, a free

driver for acquiring from GigE Vision, IEEE 1394 and USB interface cameras.
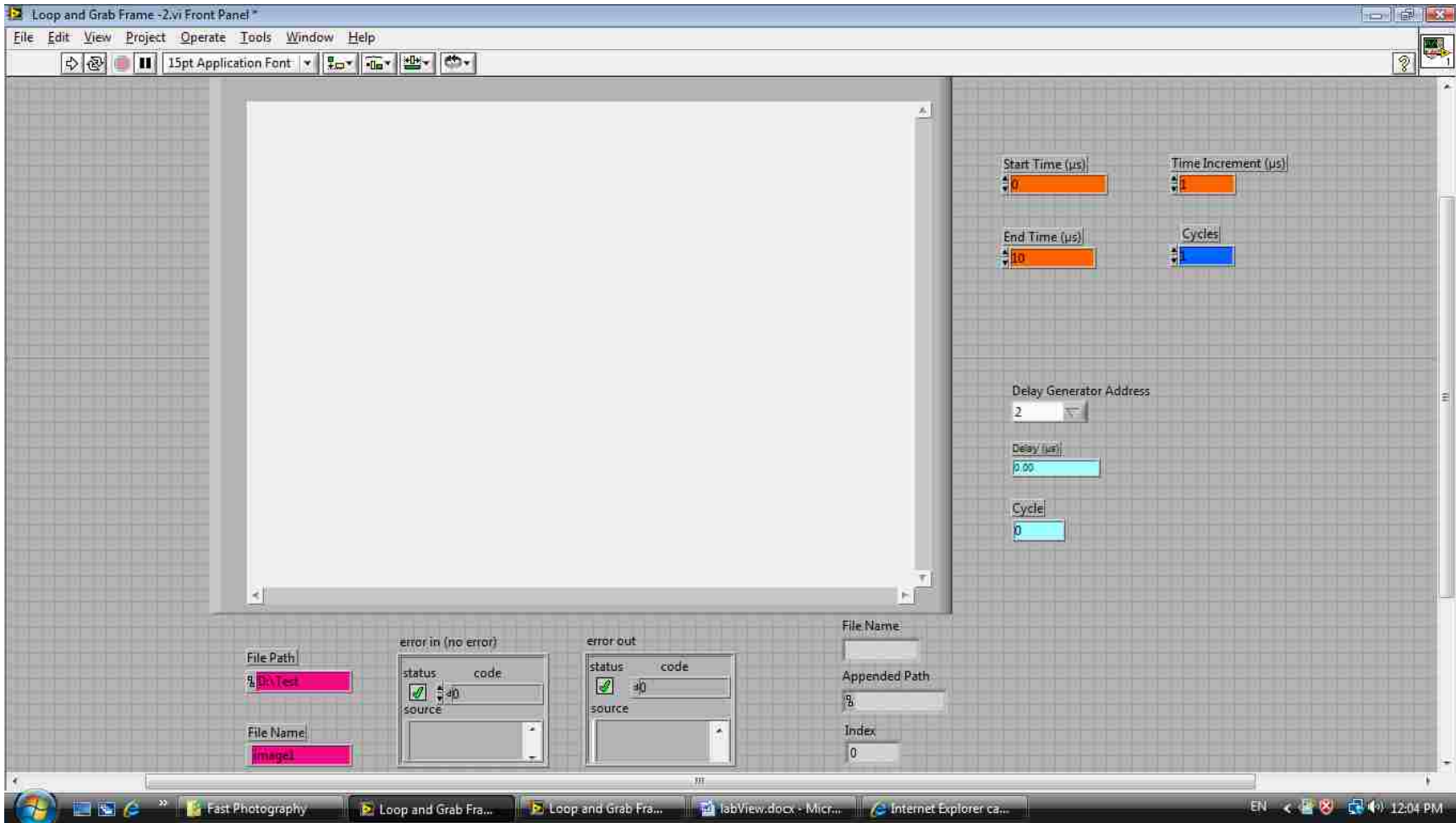
Figure B-1 Front panel of "Loop and Grab Frame-2.vi". The photographs acquired from the camera are shown in big box on the front panel.
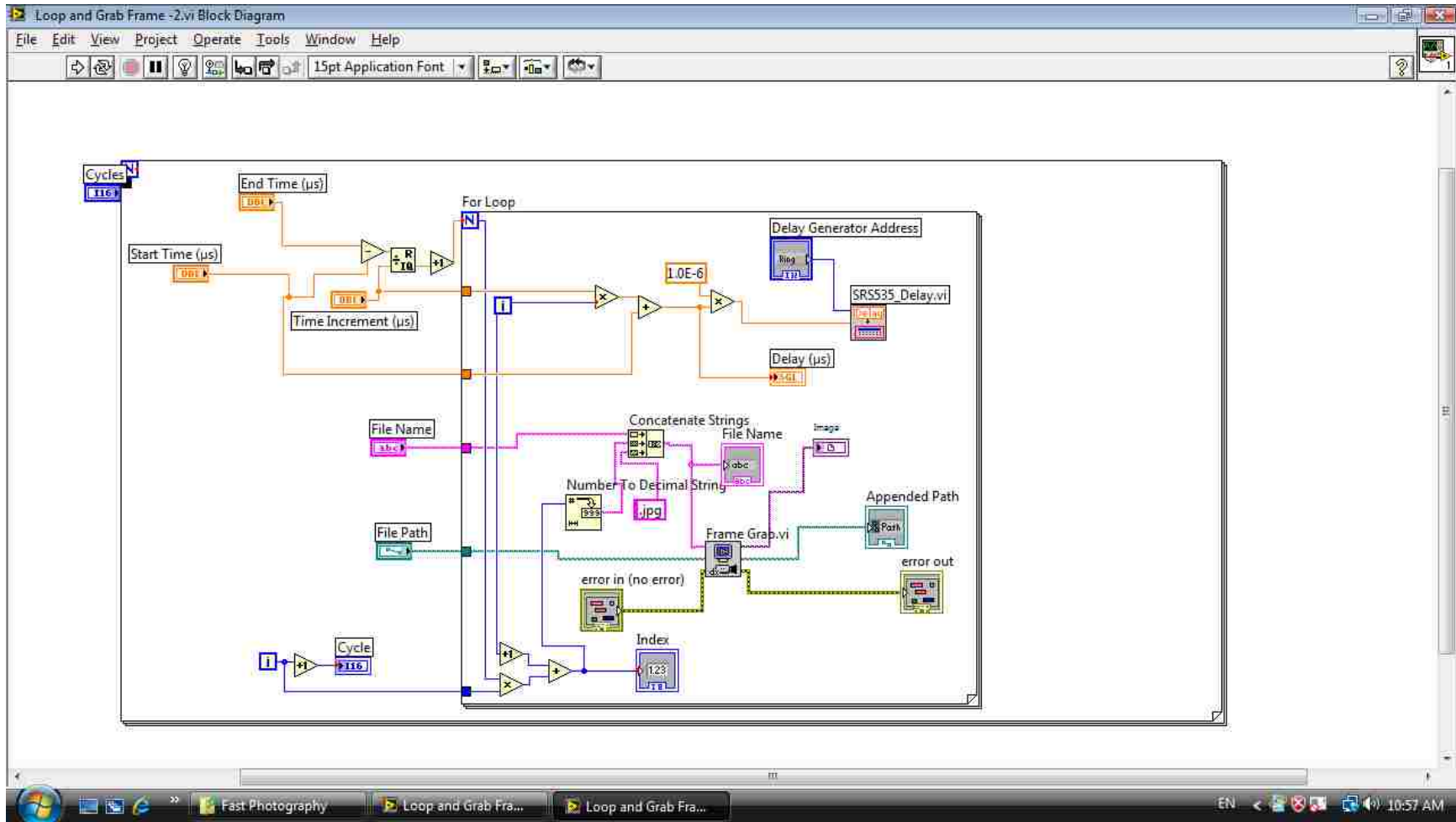
Figure B-2 The block diagram of "Loop and Grab Frame-2.vi".
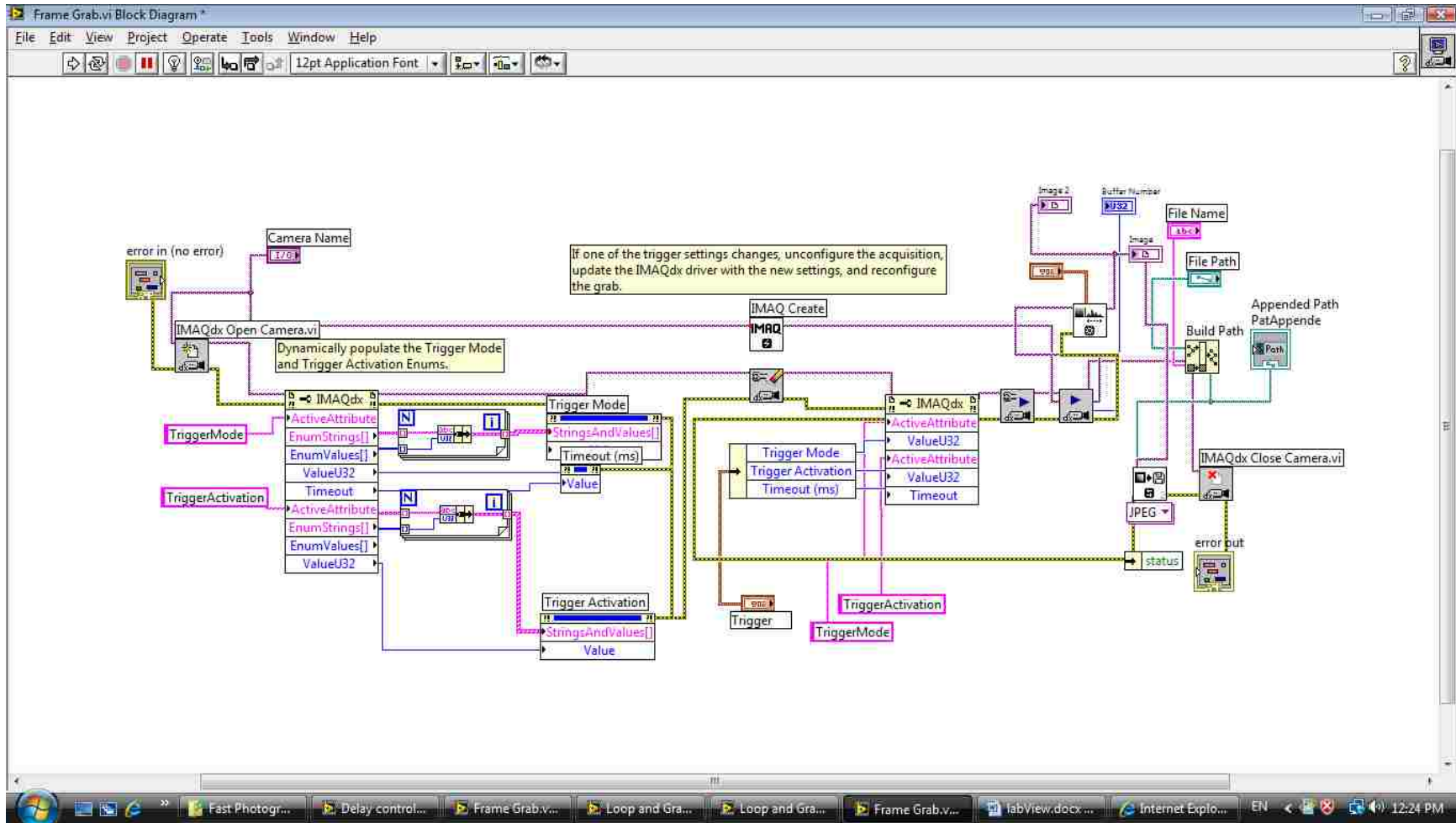
Figure B-3 The block diagram of sub-VI, "Frame Grab.vi".

APPENDIX C. PHOTOGRAPHS OF PLUME EVOLUTION

The plume evolution of glycerol ablation at different IR wavelengths, fluences and delay time are shown in Appendix C. A rapid plume expansion, followed by an extended emission of particles ablated from the target surface is observed.
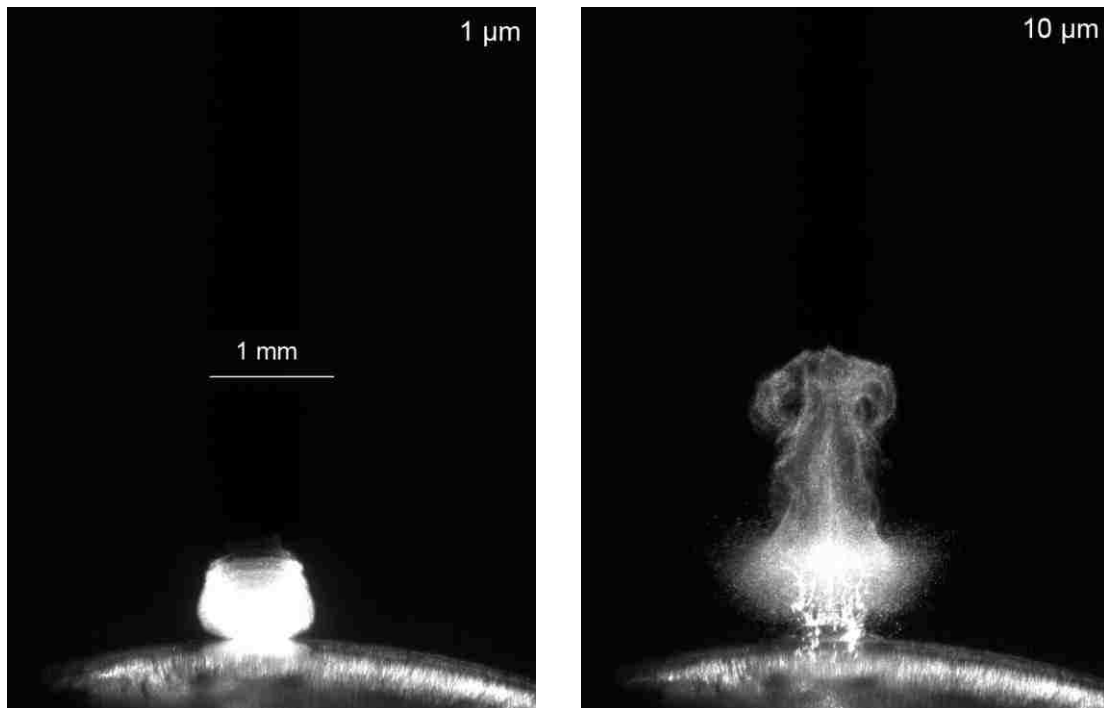
Figure C-1 2.94 µm wavelength IR laser-produced glycerol ablation at a fluence of 9000 J/m^2 at different delay time.
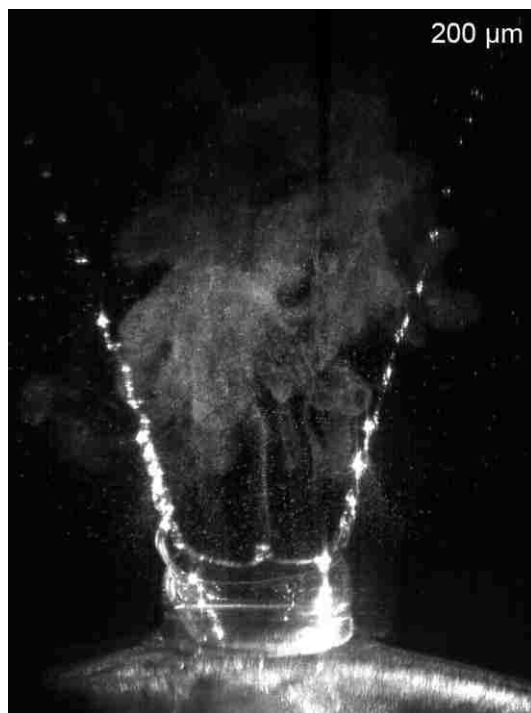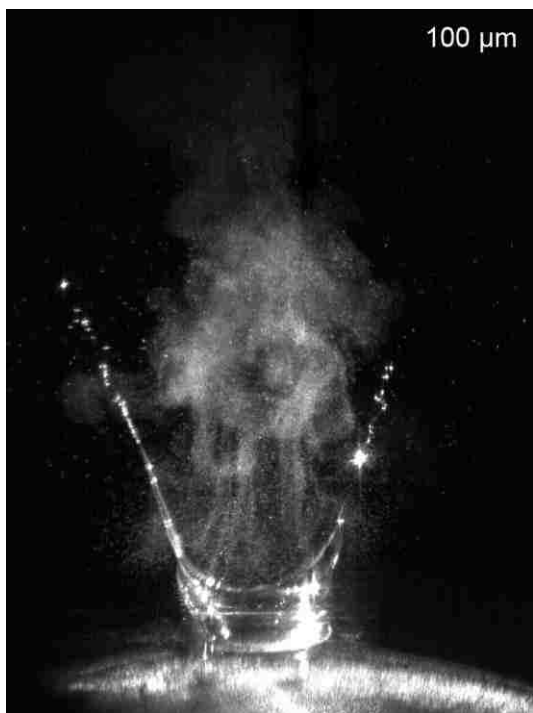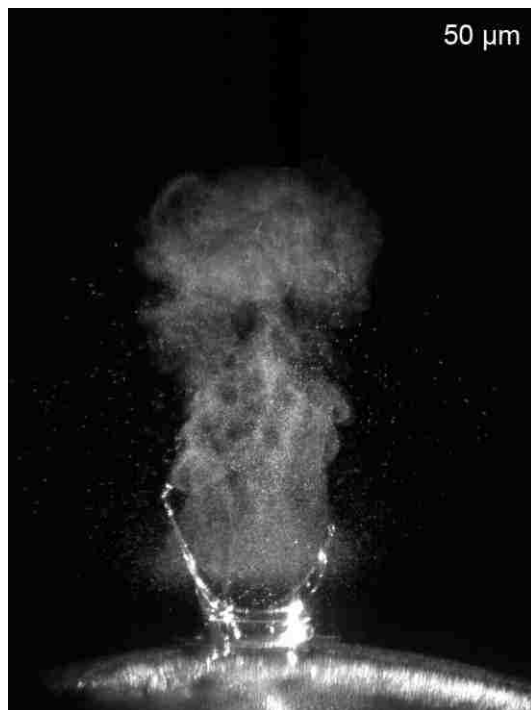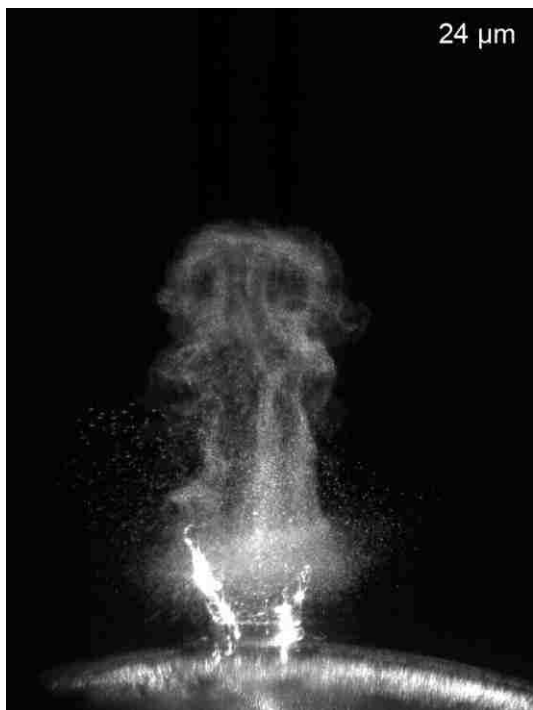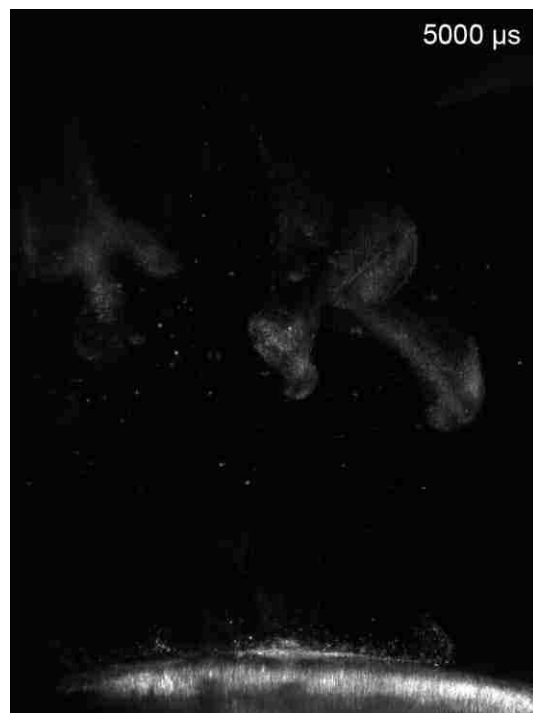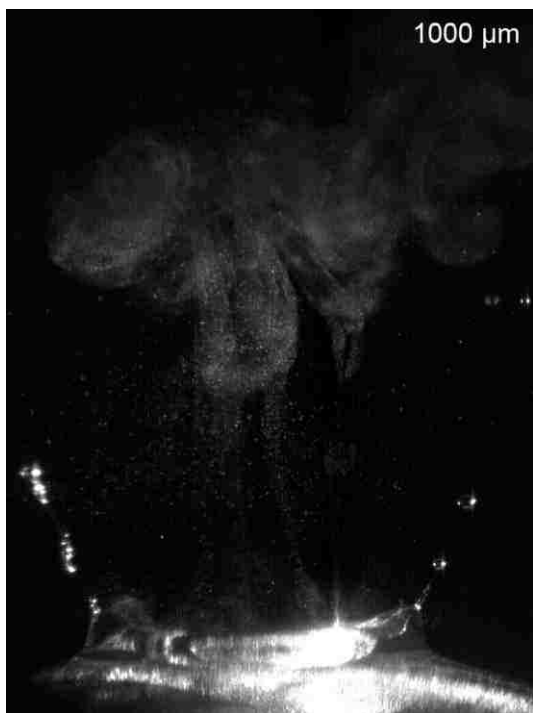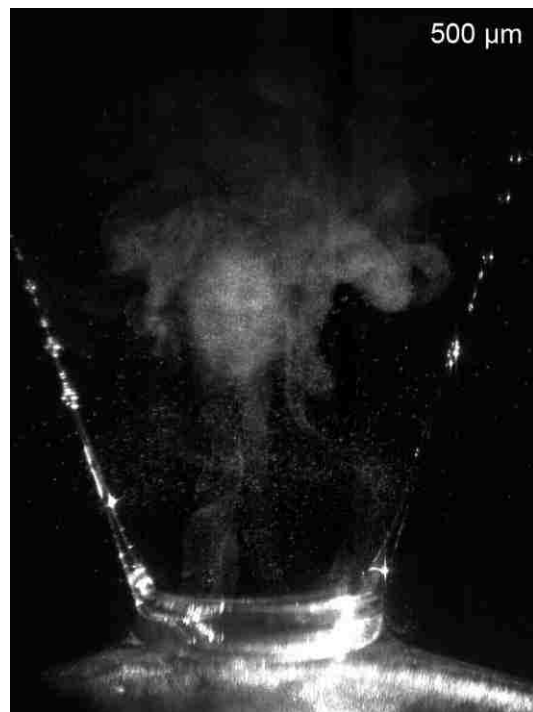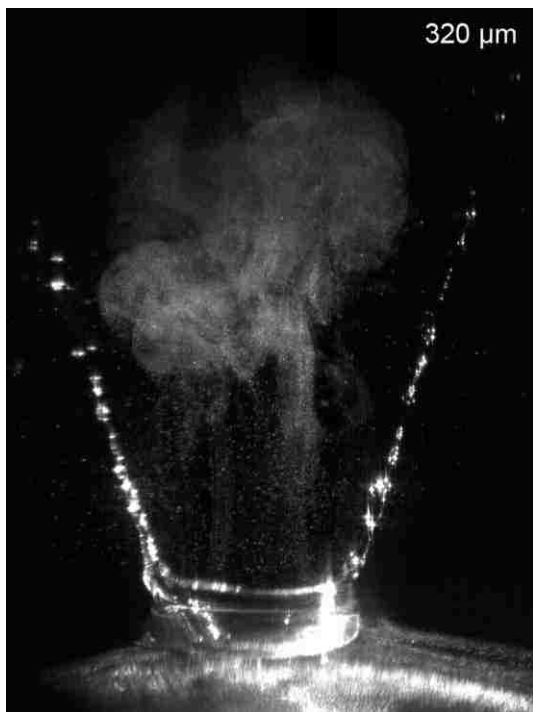
Figure C-2 3.5 μm wavelength IR laser-produced glycerol ablation at a fluence of 6000 J/m^2 at different delay time.

Figure C-3 3.5 µm wavelength IR laser-produced glycerol ablation at a fluence of 9000 J/m^2 at different delay time.
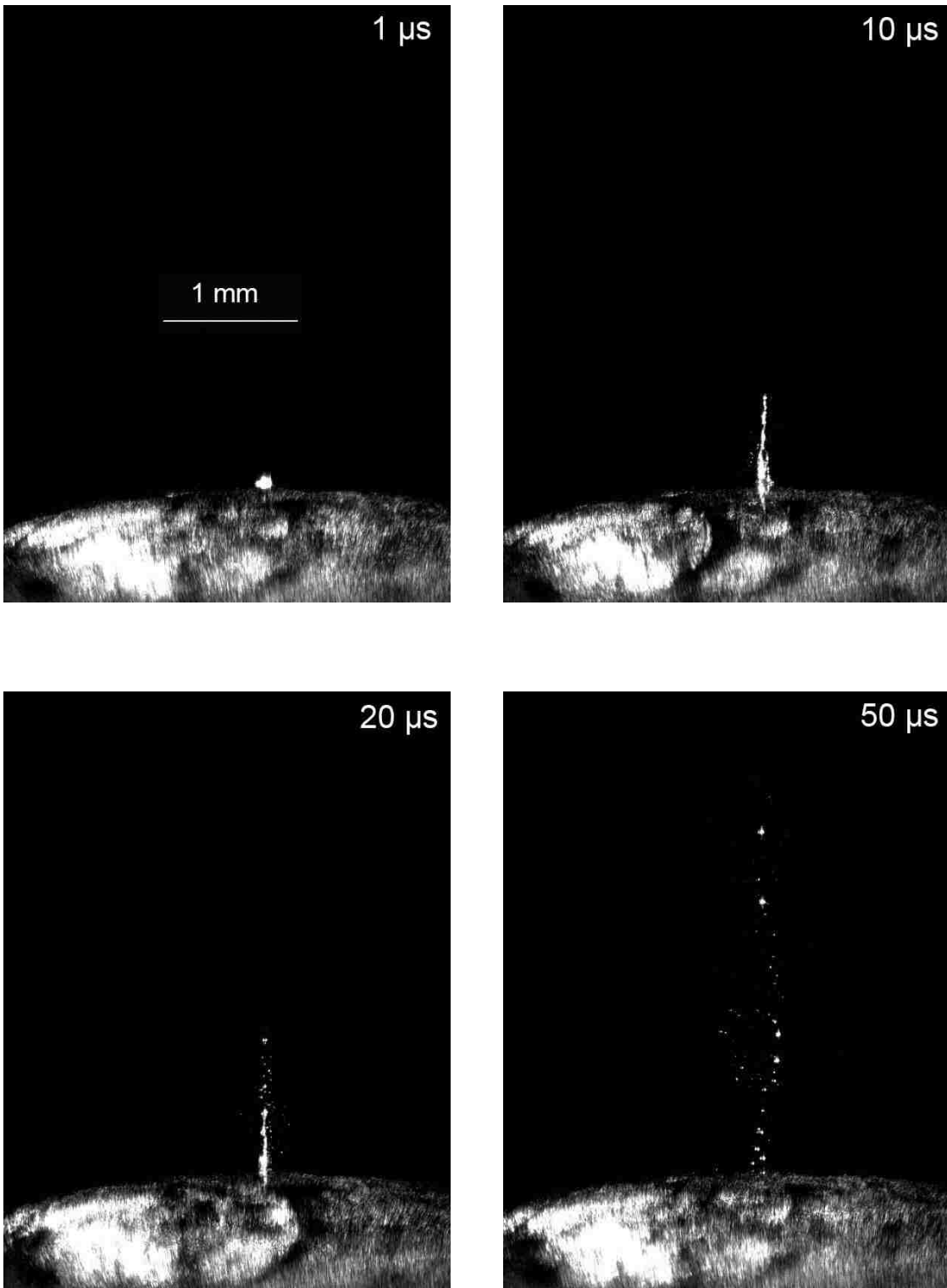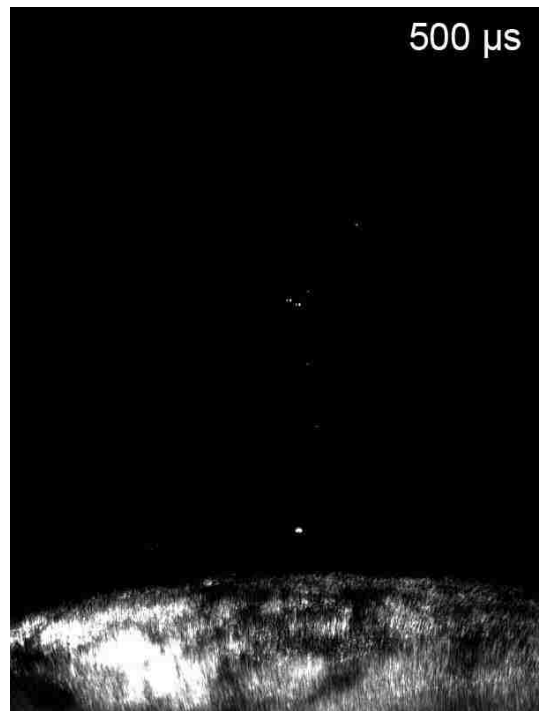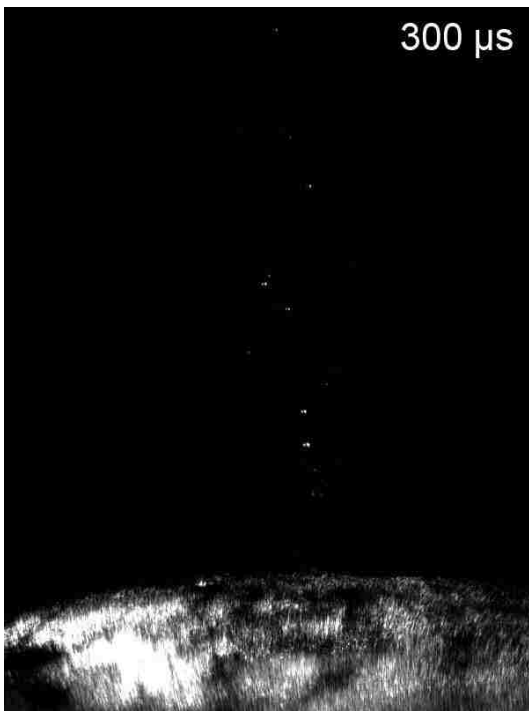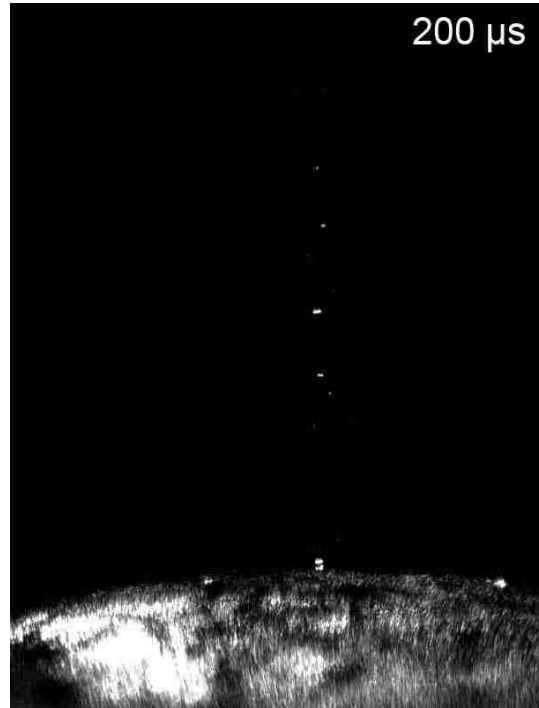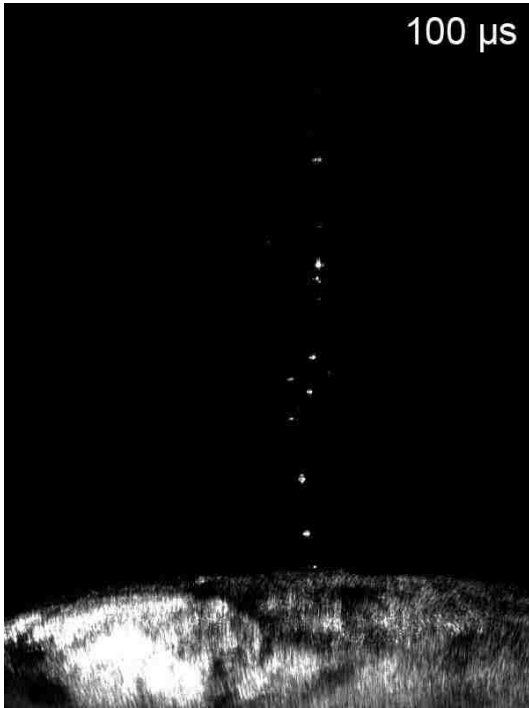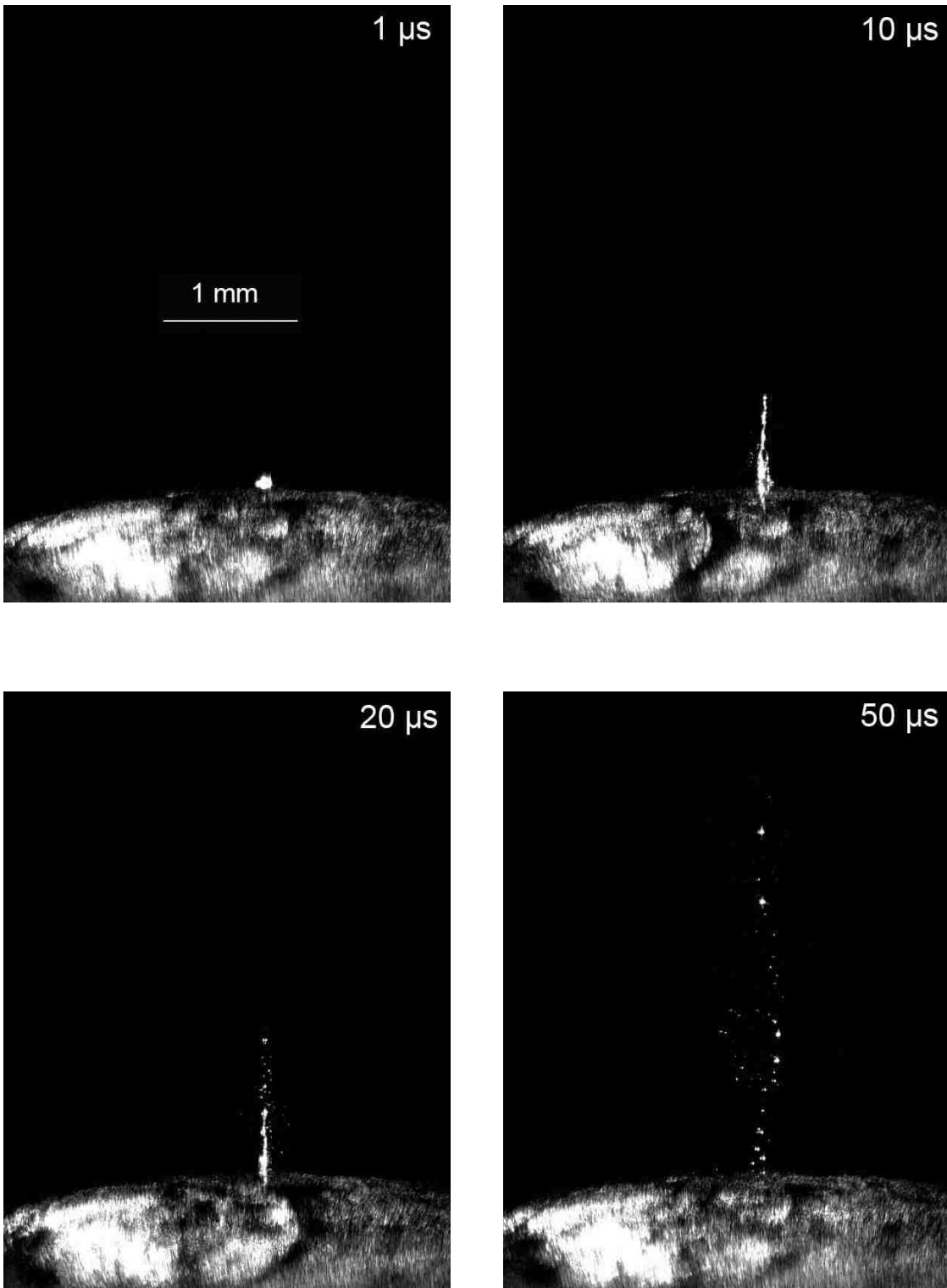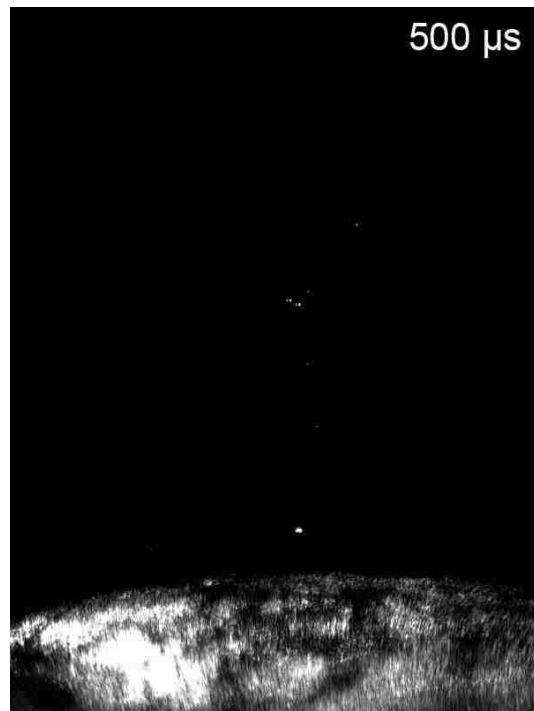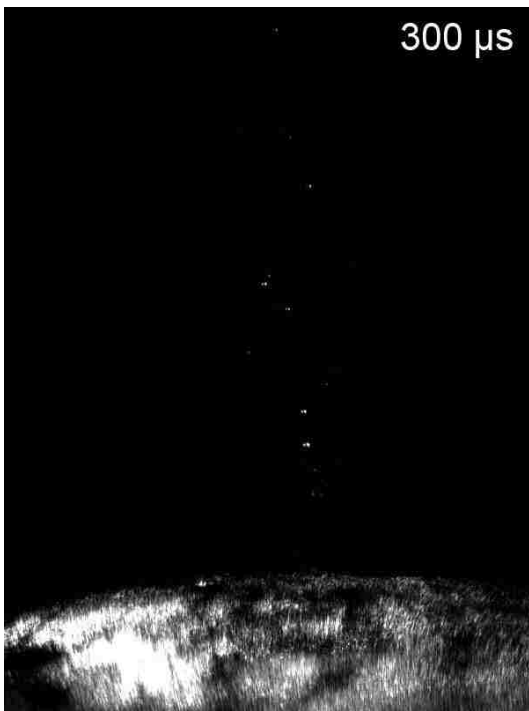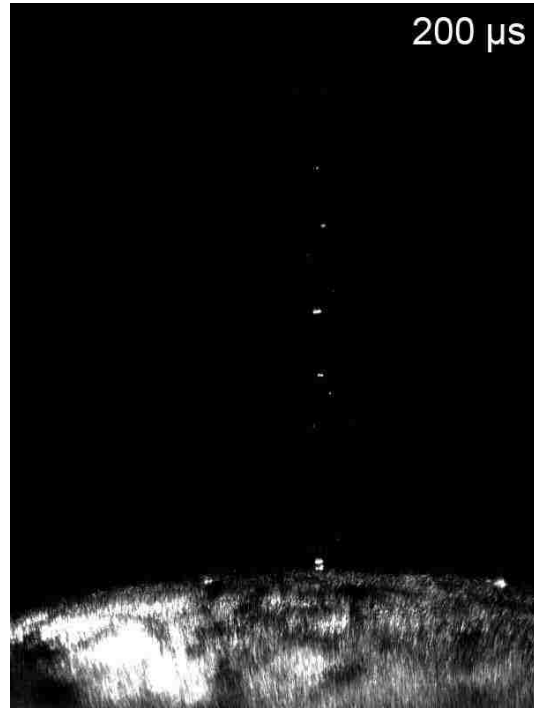
(**Figure C-3** continued)

APPENDIX D. COPYRIGHT

**AMERICAN CHEMICAL SOCIETY LICENSE
TERMS AND CONDITIONS**

Nov 14, 2010

This is a License Agreement between Xing Fan ("You") and American Chemical Society ("American Chemical Society") provided by Copyright Clearance Center ("CCC"). The license consists of your order details, the terms and conditions provided by American Chemical Society, and the payment terms and conditions.

All payments must be made in full to CCC. For payment instructions, please see information listed at the bottom of this form.

License Number	2546911028940
License Date	Nov 13, 2010
Licensed content publisher	American Chemical Society
Licensed content publication	The Journal of Physical Chemistry A
Licensed content title	Wavelength and Time-Resolved Imaging of Material Ejection in Infrared Matrix-Assisted Laser Desorption†
Licensed content author	Xing Fan et al.
Licensed content date	Jan 1, 2010
Volume number	114
Issue number	3
Type of Use	Thesis/Dissertation
Requestor type11	Not specified
Format	Print and Electronic
Portion	50% or more of original article
Author of this ACS article	Yes
Order reference number	
Title of the thesis / dissertation	Particle analysis in infrared laser desorption and ablation
Expected completion date	Nov 2010
Estimated size(pages)	140
Billing Type	Invoice
Billing Address	232 Choppin Hall
	Louisiana State University
	Baton Rouge, LA 70803
	United States
Customer reference info	
Total	0.00 USD
Terms and Conditions	

**ELSEVIER LICENSE
TERMS AND CONDITIONS**

Nov 14, 2010

This is a License Agreement between Xing Fan ("You") and Elsevier ("Elsevier") provided by Copyright Clearance Center ("CCC"). The license consists of your order details, the terms and conditions provided by Elsevier, and the payment terms and conditions.

All payments must be made in full to CCC. For payment instructions, please see information listed at the bottom of this form.

Supplier	Elsevier Limited The Boulevard,Langford Lane Kidlington,Oxford,OX5 1GB,UK
Registered Company Number	1982084
Customer name	Xing Fan
Customer address	232 Choppin Hall
	Baton Rouge, LA 70803
License number	2546920413007
License date	Nov 13, 2010
Licensed content publisher	Elsevier
Licensed content publication	Applied Surface Science
Licensed content title	UV laser irradiation of IR laser generated particles ablated from nitrobenzyl alcohol
Licensed content author	Xing Fan, Kermit K. Murray
Licensed content date	1 April 2009
Licensed content volume number	255
Licensed content issue number	12
Number of pages	6
Type of Use	reuse in a thesis/dissertation
Intended publisher of new work	other
Portion	full article
Format	both print and electronic
Are you the author of this Elsevier article?	Yes
Will you be translating?	No
Order reference number	
Title of your thesis/dissertation	Particle analysis in infrared laser desorption and ablation

https://s100.copyright.com//CustomerAdmin/PLF.jsp?lID=2010110_1289630717007   11/14/2010

Expected completion date	Nov 2010
Estimated size (number of pages)	140
Elsevier VAT number	GB 494 6272 12
Terms and Conditions	

ELSEVIER LICENSE
TERMS AND CONDITIONS

Nov 14, 2010

This is a License Agreement between Xing Fan ("You") and Elsevier ("Elsevier") provided by Copyright Clearance Center ("CCC"). The license consists of your order details, the terms and conditions provided by Elsevier, and the payment terms and conditions.

All payments must be made in full to CCC. For payment instructions, please see information listed at the bottom of this form.

Supplier	Elsevier Limited The Boulevard,Langford Lane Kidlington,Oxford,OX5 1GB,UK
Registered Company Number	1982084
Customer name	Xing Fan
Customer address	232 Choppin Hall
	Baton Rouge, LA 70803
License number	2546920688862
License date	Nov 13, 2010
Licensed content publisher	Elsevier
Licensed content publication	Applied Surface Science
Licensed content title	Infrared laser wavelength dependence of particles ablated from glycerol
Licensed content author	Xing Fan, Mark W. Little, Kermit K. Murray
Licensed content date	30 December 2008
Licensed content volume number	255
Licensed content issue number	5
Number of pages	6
Type of Use	reuse in a thesis/dissertation
Intended publisher of new work	other
Portion	full article
Format	both print and electronic
Are you the author of this Elsevier article?	Yes
Will you be translating?	No
Order reference number	
Title of your thesis/dissertation	Particle analysis in infrared laser desorption and ablation

https://s100.copyright.com//CustomerAdmin/PLF.jsp?lID=2010110_1289630992862   11/14/2010

Expected completion date	Nov 2010
Estimated size (number of pages)	140
Elsevier VAT number	GB 494 6272 12
Terms and Conditions	

VITA

Xing Fan, whose IQ is 126, was born in Huaibei, China, in 1978. He graduated from No. 1 High School of Huaibei City in 1995. During the high school, he won the championship in the high school soccer tournament of Huaibei City. He received a Bachelor of Science degree in material chemistry at University of Science and Technology of China (USTC) in 2000. As an undergraduate student, he won another championship in the soccer tournament of USTC. After one year of industry experiences, he decided to extend his study in material science with his advisor, Dr. Changrong Xia, at USTC in 2001. During the graduated study at USTC, he worked on interfacial polarization resistance between the cathode and electrolyte of solid oxide fuel cells. Two first-author papers, two co-author papers and five conference proceedings were completed by him at USTC. Three years later, he got a Master of Engineering degree from Department of Material Science and Engineering, USTC. He was named the outstanding graduate of USTC that only the top 5% of graduate students received this honor. In 2004, he joined Dr. Kermit K. Murray research group at Louisiana State University (LSU) for the doctoral program of analytical chemistry. He knew nothing about football before coming to US but later became a faithful fan of LSU tiger. During the doctoral program, he focused on the particle and plume analysis in infrared laser ablation. He is currently a member of the American Society of Mass Spectrometry (ASMS). He has presented his research at eight conferences and published three first-author papers and one co-author paper. He is currently a candidate for the degree of Doctor of Philosophy in chemistry, which will be awarded at the Fall 2010 Commencement.